The Origins of Nanoscale Oxide Inclusion and its Evolution in Additively Manufactured Austenitic Stainless Steel During Laser Powder Bed Fusion and Post Heat Treatment

by

Pu Deng

A dissertation submitted to the Graduate Faculty of
Auburn University
in partial fulfillment of the
requirements for the Degree of
Doctor of Philosophy

Auburn, Alabama
Aug 8, 2020

Keywords: Austenitic stainless steel, Additive manufacturing, Oxide inclusions,
Powder spattering, Post heat treatment

Approved by

Barton Prorok, Chair, Professor of Materials Engineering

Xiaoyuan Lou, Professor of Materials Engineering

Pengyu Chen, Professor of Materials Engineering

Jeff Suhling, Professor of Mechanical Engineering

Abstract

The origins of nanoscale oxide inclusions in 316L austenitic stainless steel (SS) manufactured by laser powder bed fusion (L-PBF) was investigated by quantifying the possible intrusion pathways of oxygen contained in the precursor powder, extraneous oxygen from the process environment during laser processing, and moisture contamination during powder handling and storage. When processing the fresh, as-received powder in a well-controlled environment, the oxide inclusions contained in the precursor powder were the primary contributors to the formation of nanoscale oxides in the final additive manufactured (AM) product. These oxide inclusions were found to be enriched with oxygen getter elements like Si and Mn. By controlling the extraneous oxygen level in the process environment, the oxygen level in AM produced parts was found to increase with the extraneous oxygen level. The intrusion pathway of this extra oxygen was found to be dominated by the incorporation of spatter particles into the build during processing. Moisture induced oxidation during powder storage was also found to result in a higher oxide density in the AM produced parts. SS 316L powder free of Si and Mn oxygen getters was processed in a well-controlled environment and resulted in a similar level of oxygen intrusion. Microhardness testing and tensile testing indicated that the oxide volume fraction increase from extraneous oxygen did not influence mechanical properties. However, a marked decrease in hardness was found for the humidified and Si-Mn free AM processed parts.

Spatter particle re-incorporation was found to be significantly affected by the laser scanning direction with respect to inert gas flow in the L-PBF process chamber. Laser scans parallel to the gas flow of the L-PBF process, more specifically, against the gas flow reduce the risk of spatter particle re-incorporation in as-printing parts. Laser scans perpendicular to the gas flow leads to more partially sintered spatter particles on the as-built sample surface. Except for the role of oxygen getters, spatter particles also result in higher surface roughness for as-built AM 316L SS owing to its larger average size than fresh powder. Other than spatter particles generated from the melt pool, spatter particles from adjacent parts on the build plate could also

incorporate into the as-printing parts. Although spatter particles have been shown to introduce defects in AM parts, a decrease in tensile properties was not observed for as-built parts contain a higher amount of spatter particles, possibly due to the small build volume.

The evolution of nanoscale oxide inclusions presented in 316L SS manufactured by L-PBF was explored from three aspects, size, chemistry and morphology, and distribution. The average size of oxide inclusion increased from 50 nm in as-built 316L SS to 392 nm in fully recrystallized 316L SS. The coarsening of oxides was found to be controlled by Ostwald ripening, and the recrystallization process considerably facilitated the coarsening. A fraction of $MnSiO_3$ oxides converted to core-shell structure with Mn enriches at the shell and Si-rich core in the recrystallized grain, and some converted to $CrMn_2O_4$ in the unrecrystallized grain. The grain boundary migration has shown to capable of dragging oxides and move jointly. This led to a significant amount of oxides accumulated at the grain boundary. The fraction of grain boundary oxides decreases with increasing grain size.

Acknowledgement

Firstly, I would like to express my gratitude to my advisor Prof. Barton Prorok, for guiding me, supporting me, and inspiring me all the time through this journey. His guidance enabled me to think critically and creatively in conducting my research program. His patience and continuous encouragement greatly strengthened my confidence. I could not have hoped for a better advisor.

I would like to extend my thankfulness to Prof. Xiaoyuan Lou, who also supervise my research work, for his guidance and constant help. I benefited greatly from his extensive knowledge and long experience with metallurgy and metal additive manufacturing. His constructive criticism kept me motivated to improve my work.

I would like to thank for the time and effort from committee members, Pro. Xiaoyuan Lou, Prof. Pengyu Chen, Prof. Jeff Suhling, and university reader Prof. Robert Jackson. I appreciate for their valuable suggestions and advice.

I would like to express my appreciation to department technician Mr. Steven Moore for equipment training, Mr. Mike Crumple for fixing equipment, and department secretary Ms. Cheryl Rhodes for organizing fantastic activities. I am also appreciative to my seniors, Dr. Anqi Zhang, Yan Chen, Liangxi Li, for offering me great help when I came to Auburn. I would like to thank a large number of colleagues that have helped me during the journey, Ralf Fisher, Hayden Price, Dr. Jiahui Xu, Jiawei Zheng, Dr. Songtao Du, Dr. Yuzhe Liu, Dr. Lang Zhou, Yuzhe Sun, Jingfan Yang, Houshang Yin, Dr. Hossein Talebinezhad, Dr. Yang Tong, Dr. Rong Zhao, etc. More importantly, I sincerely appreciate my parents, Xiaohui Deng and Sailan Wang, for their unconditional love and support.

Lastly, I would like to express my gratefulness to my dear wife, Xue Li. Her love, support, and understanding made me get rid of worries and overcome difficulties through this journey. I am truly grateful to have her by my side.

Table of Contents

Lists of Figures

Lists of Tables

Lists of Abbreviations

AM	Additive Manufacturing
CAD	Computer-aided Design
DED	Direct Energy Deposition
SLM	Selective Laser Melting
L-PBF	Laser Powder Bed Fusion
SS	Stainless Steel
BSE	Backscattered Electron
SE	Secondary Electron
EDX	Energy Dispersive X-ray Spectrometry
SEM	Scanning Electron Microscopy
TEM	Transmission Electron Microscopy

Chapter 1

Introduction

1.1 Additive manufacturing

Additive Manufacturing (AM), also called Rapid Prototyping, enables the production of parts directly from computer-aided design (CAD) models, and is a well-known technology nowadays. AM processes build three-dimensional parts by successively melting or sintering thin layers of materials in the shape of powders, wires or sheets. This unique feature enables manufacturing of customized parts with exceptionally high design freedom in a single step, in contrast to traditional subtractive manufacturing methods such as milling and drilling. Moreover, it saves a substantial amount of raw materials as compared to traditional methods. The creative design freedom of AM realizes considerably lessening of part number of a conventional assembly and it also significantly shortens the cost and time for developing components with complex geometries. All these advantages of AM bring a broad range of applications to transportation, aerospace, medical, energy and consumer products industries.

Metal additive manufacturing processes can be classified into seven categories according to ASTM F42 Committee on Additive Manufacturing: VAT Polymerization, Material Jetting, Binder Jetting, Materials Extrusion, Power Bed Fusion (PBF), Sheet Lamination, Direct Energy Deposition (DED). Among all additive manufacturing techniques, selective laser melting (SLM), also known as laser powder bed fusion (L-PBF) is the optimum choice to offer high manufacturing resolution and excellent part quality.

1.2 Overview of work presented herein

There are three main projects presenting in this work, and they are introduced in Chapter 2-4.

In Chapter 2, we examined all three possible origins of oxygen in 316L stainless steel (SS) manufactured by L-PBF. Three sources of oxygen contamination have been studied: precursor powder, process chamber atmosphere, and powder long-term storage. A special 316L SS powder was made by removing its regular oxygen getters, the inclusion in the corresponding AM parts and its mechanical properties were investigated. The mechanism of oxygen transfer to additive parts was illustrated, and the effects of oxygen on mechanical properties and the melt pool of austenitic stainless steel (SS) manufactured by laser powder bed fusion were characterized.

In Chapter 3, the transportation of spatter particles that ejected from the melt pool to the as-printing sample surface during the L-PBF process was found to be significantly affected by the scanning direction of the laser beam relative to the gas flow. The effects of spatter particles on AM 316L SS were characterized by surface roughness, oxygen intrusion, and mechanical properties.

In Chapter 4, we studied the evolution of nano-oxides in 316L SS during heat treatment. The evolution of nano scale oxide inclusions presented in 316L SS manufactured by L-PBF was explored from three aspects, size, chemistry and morphology, and distribution. Grain boundary migration initiated by recrystallization after heat treatment was found to considerably facilitate the coarsening of oxide inclusions, and the migrating grain boundaries were found to be capable of altering the distribution of oxide inclusions.

Chapter 2

Origins of Nano-Oxides and Oxygen Intrusion in 316L Stainless Steel Manufactured by Laser Powder Bed Fusion

2.1 Introduction

Metal-based additive manufacturing (AM) has made appreciable impacts in the metal fabrication industry due to the ability to fabricate complex geometry parts that cannot be easily achieved by conventional methods [1]. Selective laser melting (SLM), also known as laser powder bed fusion (L-PBF), has emerged as the optimum choice to offer high manufacturing resolution and excellent part quality among many metal AM technologies. With the assistance of computer-aided design (CAD), L-PBF creates complex structures in a layer-by-layer fashion through selective laser melting according to a sliced and pixelated, 3D computer model. The feedstock powder for L-PBF is generally manufactured by the inert gas atomization process [1], which usually results in the powder containing hundreds of ppm of oxygen [2]. Owing to its large anion radius, oxygen cannot be easily accommodated interstitially in austenitic stainless steels [3, 4]. Thus, excess oxygen typically remains in the matrix where it can react with high oxygen affinity elements in steel to form oxide inclusions [5]. In the L-PBF process, there is greater opportunity for oxygen to form inclusions. As such, uniformly distributed nano-scale oxides rich in Si and Mn have been reported in 316L SS built by L-PBF [6, 7]. Some studies show that nano-scale oxide inclusions can improve the mechanical properties of AM 316L SS compared to those devoid of them [8-11], while others note that the strengthening effect of oxides is negligible at best [12]. Recent work has also suggested oxide inclusions in AM 316L SS suppresses MnS formation, which leads to superior pitting corrosion resistance [13]. However, when compared to their wrought counterparts, these inclusions were also shown to have detrimental effects on cracking behavior, resulting in lower toughness and higher stress corrosion cracking (SCC) susceptibility [14].

Inclusions in alloys are usually considered microstructural defects that typically deteriorate mechanical properties and/or corrosion resistance [15]. In metal casting, inclusions commonly consist of nitrides, carbides, sulfides and a mixture of compounds that can nucleate voids and microcracks that lead to premature failure under impact or fatigue loading [15]. Due to the thermal and elastic properties differences between matrix and inclusion, voids may form around inclusions under deformation [15]. With further loading, stress becoming concentrated at matrix and inclusion interface where voids grow by coalescence and lead to numbers of microcracks. Eventually, propagation of microcracks around inclusion results in failure of materials. Hence, early initiation of microcracks around inclusions are important origin of reduction of materials impact toughness and fatigue performances. Moreover, it has been demonstrated that inclusion-based defects can entrap hydrogen and increase the material's susceptibility to hydrogen embrittlement [16]. Finally, although stainless steel is well known for its superior corrosion resistance, the existence of inclusions can compromise the protective chromium oxide layer to cause pitting corrosion [15]. Pit corrosion refers to the dissolution of inclusions and leaves small holes in the metal matrix and it was suggested that most of pits tend to initiate around inclusions. Despite this significant list of detrimental effects, oxide inclusions have great potential to improve alloy strength by introducing uniformly dispersed, ultrafine particles into the metal matrix that impede dislocations during plastic deformation. A significant benefit of this oxide dispersion strengthening (ODS) is superior creep resistance at elevated temperatures [17-21]. Additionally, high-density nano-oxide particles can act as sinks to radiation-induced vacancies and interstitials towards significantly reducing radiation damage in nuclear reactor environments [18, 22, 23]. Recent efforts have also been made to produce effective nano-scale oxide dispersions in metals fabricated by AM [24-27].

In L-PBF fabrication of SS, oxide formation can significantly impact the build quality and reproducibility, especially when printing materials with higher oxygen reactivity, such as aluminum and titanium. On the other hand, finding an effective way to control and optimize oxide dispersions in L-PBF fabrication can lead to the development of advanced ODS alloys with superior performance. Compared to the significant interests on the characteristics and properties that oxide inclusions can impart to AM parts, a fundamental understanding of where these oxides originated has not been well established.

Considering the entire AM processing chain, from powder fabrication to the end-use part, there are three possible oxygen sources/pathways of incorporation into the alloy. The first and most obvious is oxygen incorporation during the gas atomization fabrication of the powder. Another source would be in-situ oxidation during L-PBF from extraneous oxygen in the process environment. Another pathway involves moisture-induced oxidation from powder transportation and storage conditions. Studies have shown that oxygen contamination in precursor powders has a linear relationship with the density of oxide inclusions in parts produced by powder metallurgy with hot isostatic pressing (PM-HIP) [28, 29]. Similar studies have also evaluated gas atomized 316L SS powder for AM applications [30-32]. However, the surface and interior oxidation of the powders during gas atomization and its impacts on the part quality has not been systematically evaluated.

It has also been a long-time interest of the AM community to understand the effects of moisture on the quality of AM parts, especially related to oxidation. Some studies have suggested that liquid bridging between particles and surface oxides caused by moisture contamination can retard the flowability of AM powders [33, 34]. To our best knowledge, the effects of moisture exposure to oxide inclusion formation, including their effect on mechanical properties, have not been evaluated.

Compared to the potential oxygen contamination on the precursor powders, there are fewer concerns of oxygen intrusion during the L-PBF process, primarily due to the protective, closed-loop argon environment. However, a residual oxygen level in the process chamber is unavoidable and can fluctuate with build time and gas supply. Some efforts have been made to evaluate the effects of environmental oxygen in the process chamber on oxide inclusions in austenitic stainless steel. Eo et al. studied the effects of the laser metal deposition (LMD) process parameters on melt pool oxidation for 316L SS and suggested that yield stress was proportional to inclusion number density [35]. Song et al. examined the effects of environmental oxygen partial pressure on the morphology, composition, size and number density of oxide inclusions [36]. Metals printed by L-PBF generally experience much faster cooling rates as compared to those by LMD. Thus, different oxidation reaction dynamics are expected. The dominant path of oxygen transfer during L-PBF and its impacts on microstructure and mechanical properties is critical to understanding their effects and controlling their formation and evolution to improve mechanical performance. This work is aimed at providing a systematic understanding of the origin and formation of oxygen inclusions in austenitic stainless steels manufactured by L-PBF.

2.2 Experimental instruments and procedures

The images of all instruments located at Auburn University, Materials Engineering department used in this work are given in the Appendix.

2.2.1 Powder materials and L-PBF system

316L SS precursor powder manufactured by nitrogen-gas atomization purchased from Carpenter Powder Products and General Electric Company (GE) were used in this study. Table 1 shows the initial composition of the as-received fresh powder. The powders were sieved to -325 mesh/+15 μm (15-44 μm) for good flowability and AM parts were printed with an EOSINT M270 system (at Quad City Manufacturing Laboratory, Rock Island, IL, USA) and a Concept Laser Mlab LaserCusing® system (at Auburn University, Auburn, AL, USA) to evaluate the process-to-process and machine-to-machine variability. The EOS system used 195 W of laser power, 1.2 m/s scan speed and 20 μm layer thickness, while the Concept Laser System used 90 W laser power, 0.6 m/s scan speed and 25 μm layer thickness.

2.2.2 Section and polishing of AM part

All AM parts were sectioned parallel to the build-up direction. Surfaces were prepared by mechanically grinding to a 220 grit using SiC grinding papers and then followed by polishing with 9um, 3um diamond suspension using Struers TegraPol-15 Auto-polisher with Tegraforce-1. Surfaces were finalized with vibratory polishing using colloidal silica using Buehler Vibromet 2 vibratory polisher. After vibratory polishing, the surface of specimens was first cleaned with Alconox solution by wiping using microfiber cleaning cloth to remove remaining suspension particles. Then the specimens were further cleaned with ultrasonic cleaner for 30 minutes. This preparation method produced a clean, strain-free and scratch-free surface on the relatively soft austenitic stainless steel samples.

2.2.3 Density measurements of AM part

Printing parameters on both systems were determined for optimum density. The density measurements were performed by using an Olympus BX51 microscope and ImageJ software. The optical images of the surface of polished specimens were taken by optical microscope with 5X or 10X magnification depending on specimen size. The images were then analyzed by ImageJ software. The density analysis of both systems is shown in Table 2.

2.2.4 Scanning electron microscope (SEM) and transmission electron microscope (TEM)

Backscattered electron (BSE) imaging and energy dispersive X-ray spectroscopy (EDS) was conducted with a Hitachi SU70 (at Quad City Manufacturing Laboratory, Rock Island, IL, USA) or a JEOL 7200F field emission scanning electron microscope (FE-SEM)(at Tuskegee University, Tuskegee, AL, USA). BSE images were obtained with an yttrium-aluminum-garnet (YAG) scintillator detector, which offered high sensitivity and high resolution with a low beam current. Low accelerating voltages, ranged from 7 to 10 kV, were also applied in BSE imaging to reduce the beam-sample interaction volume and increase spatial resolution. Specimens for cross-sectional TEM were prepared by focused ion beam (FIB) milling. A FEI NOVA FIB was used to extract the specimens (lamellae) from regions of interest and mounted on to copper grids for further examination. A platinum overlay was used to protect the oxide layers in the milled lamellae. These lamellae were further thinned in an argon ion mill operating at a low voltage and then plasma cleaned prior to observation. TEM analysis was conducted in a FEI Osiris FEG-TEM/STEM operating at 200 kV. Bright field / dark field imaging and elemental mapping were carried out in the scanning-TEM (STEM) mode. HRTEM imaging and FFT (Fast Fourier Transform) analysis was conducted for phase identification. FFTs were analyzed using GATAN Digital Micrograph and CrystalMaker software.

2.2.5 Statistical analysis of oxide inclusion

Volume fraction and size of oxide inclusions were acquired by using ImageJ software. Fifteen BSE images from the precursor powder or AM build samples were averaged following ASTM E1245 [37].

2.2.6 Experimental procedure for studying oxygen from precursor powder

In order to examine the oxide inclusions inside the 316L SS powder, small amount of powder was cold mounted by epoxy resin in a small mold with a hole. Then the mold was connected to a vacuum pump to simulate a vacuum infiltration system, so the powders could submerge and agglomerate at the bottom of resin. After one-night for solidification, the mounted powder agglomeration was then secondly mounted into a regular mold, 32 mm in diameter in this case, using epoxy resin. This method enables powder to maintain in the mount instead of poping off during mechanical polishing. After mounting, the powder specimens were polished using the same polishing procedure as introduced in section 2.2.2.

The chemistry of surface oxides on precursor powder was assessed by PHI 680 Auger Nanoprobe auger electron spectroscopy (AES) (at EAG laboratories, East Windsor, NJ, USA) and the oxide layer thickness was determined from depth profiles after Ar ion sputtering. The electron beam conditions were 5 kV and 15 nA. The ion beam conditions were 3 keV, 2 mm × 2 mm raster. The sputter rate was 238 Å/min. The sputter rate of depth profile was calibrated for Fe_2O_3.

2.2.7 Experimental procedure for studying the effect of environmental oxygen

To study the effect of extraneous/residual oxygen in the process environment, GE powder was printed in the Concept Laser unit with a process of oxygen content ranging from 0.0% to 1.0% with interval of 0.2%. This was accomplished by varying the threshold oxygen content to begin processing, monitored by Metrotec A19-S oxygen measurements sensor. The process began by purging the chamber atmosphere with argon gas until the oxygen content reaches 1.0 %. The argon purging was then halted, and the atmosphere was then recirculated internally. Printing was then initiated for a prescribed amount of time. When finished, the argon purging continues until the next oxygen threshold was reached, and until printing at 0.0% of oxygen was completed.

2.2.8 Experimental procedure for studying the oxygen contamination during storage

The GE powder was also stored in an environmental chamber (100-200 CFM Textile Conditioning Unit) for a period of month with the temperature and relative humidity set at 28 ℃ and 80%, respectively. The effect of moisture on the powder flowability and the oxidation in the AM part were evaluated using Freeman Technology FT4 powder rheometer®, BSE imaging by

SEM, and instrumental gas analysis (IGA). IGA tests were carried out by EAG laboratories at NY, USA. Humidified 316L SS powder was printed by Concept laser system using the same process parameter as the part printed by fresh powder, and under 0% oxygen content environment.

2.2.9 Special 316L SS powder for studying the effect of oxygen getters

A Si/Mn free 316L SS alloy was prepared by Carpenter with ultra-pure feedstock materials and inert gas atomization facility. This aimed at investigating the effect of regular oxygen getters, Si and Mn, in 316L SS. AM parts were then fabricated in the Concept Laser system using the same parameters for the 316L SS given in Table 2. The chemical composition is shown in Table 1, in comparison to regular 316L SS powder from Carpenter.

2.2.10 Mechanical properties

Vickers hardness was tested using a DM-400 FT Microhardness tester (LECO Corporation) with applied force 1 kg and duration time 30 s. Five indentations were tested on each sample and the average hardness was reported. Two sets of vertical flat bars (6 mm × 2 mm × 68 mm) were printed at 0% and 1% oxygen content environment by Concept laser system for tensile test. 1% oxygen content environment was conducted by using 1% oxygen blended argon gas cylinder prepared by Airgas to maintain the oxygen level during the printing. Tensile tests were performed at room temperature on an MTS Q-test 100 Elite Testing system with the nominal strain rate of $2 \times 10^{-3}\ s^{-1}$. Yield strength was determined by 0.2% offset. The average value of three tensile test results were reported for each specimen. The tensile properties of as-built and annealed AM 316L SS (1150 ℃ for 2hr) were compared. Charpy specimens (10 mm × 10 mm × 55 mm) were also printed at two oxygen conditions, v-notch on specimens were machined by electric discharge machining (EDM) according to ASTM A370. Charpy impact tests at room temperature were conducted using Tinius Olsen impact testing machine.

		Alloy Composition (wt%)							**Impurities (ppm)**			
#	**Element**	**Fe**	**Cr**	**Mn**	**Si**	**Ni**	**Cu**	**Mo**	**C**	**O**	**N**	**S**
1	316L Powder (Carpenter)	Bal	16.7	1.02	0.74	10.7	0.19	2.29	266	384	935	61
	AM Part (EOS)	Bal	16.9	1.13	0.71	10.7	0.20	2.24	221	326	1163	62
2	316L Powder (GE)	Bal	17.7	0.92	0.73	12.8	0.02	2.33	252	239	660	32
	AM Part (Concept Laser)	Bal	17.7	0.88	0.66	12.9	0.01	2.28	219	212	800	40
3	316L Powder (Si/Mn Free)	Bal	17.7	0.02	0.01	13.9	0.00	2.84	40	440	810	40

Table 1: Chemical compositions of 316L powder purchased from Carpenter Powder Products and AM parts printed with EOS 270 SLM system, 316L SS powder purchased from General Electric were printed by Concept Laser Mlab Cusing SLM system. Alloy composition measured by inductively coupled plasma optical emission spectrometry (ICP-OES), carbon and oxygen concentrations were measured by instrumental gas analysis (IGA) according to ASTM E1019 [38].

L-PBF System	**Powder Source**	**Laser Power**	**Scan Speed**	**Layer Thickness**	**Part Density**	**Density Std. Dev.**
		(w)	**(m/s)**	**(um)**	**(%)**	**(%)**
EOS 270	Carpenter	195	1.2	20	99.81	0.08
Concept Laser	GE	90	0.6	25	99.79	0.11

Table 2: Processing parameters used on two L-PBF system, and corresponding fabricated 316L SS part density (measured using ASTM E2109 [39]).

2.3 Results and Discussion

2..3.1 The presence of oxides inside AM stainless steel parts

The oxygen concentration found in 300 series stainless steel is generally governed by the chosen fabrication method. Fig. 1 summarizes the typical oxygen concentration obtained in SS for various methods, including wrought [28, 29, 40, 41], powder metallurgy (PM) [28], casting [42-44], welding [40, 45] and L-PBF from this work. The L-PBF processing resulted in the oxygen levels that were 4-6 times higher than cast, wrought, and welded SS. Interestingly, it also was approximately 2 times greater than powder metallurgy even though both use powder fabricated by inert gas atomization. The scientific literature has reported that the higher oxygen levels found in AM and PM parts can significantly degrade the impact toughness through void formation around embedded oxide particles [14, 28, 29, 46]. It has also been demonstrated that oxygen contamination can lead to higher defect density in AM parts [47]. Therefore, a comprehensive understanding of the origin of oxygen intrusion can play a critical role in reducing part-to-part variation as well as support standards development and quality control.

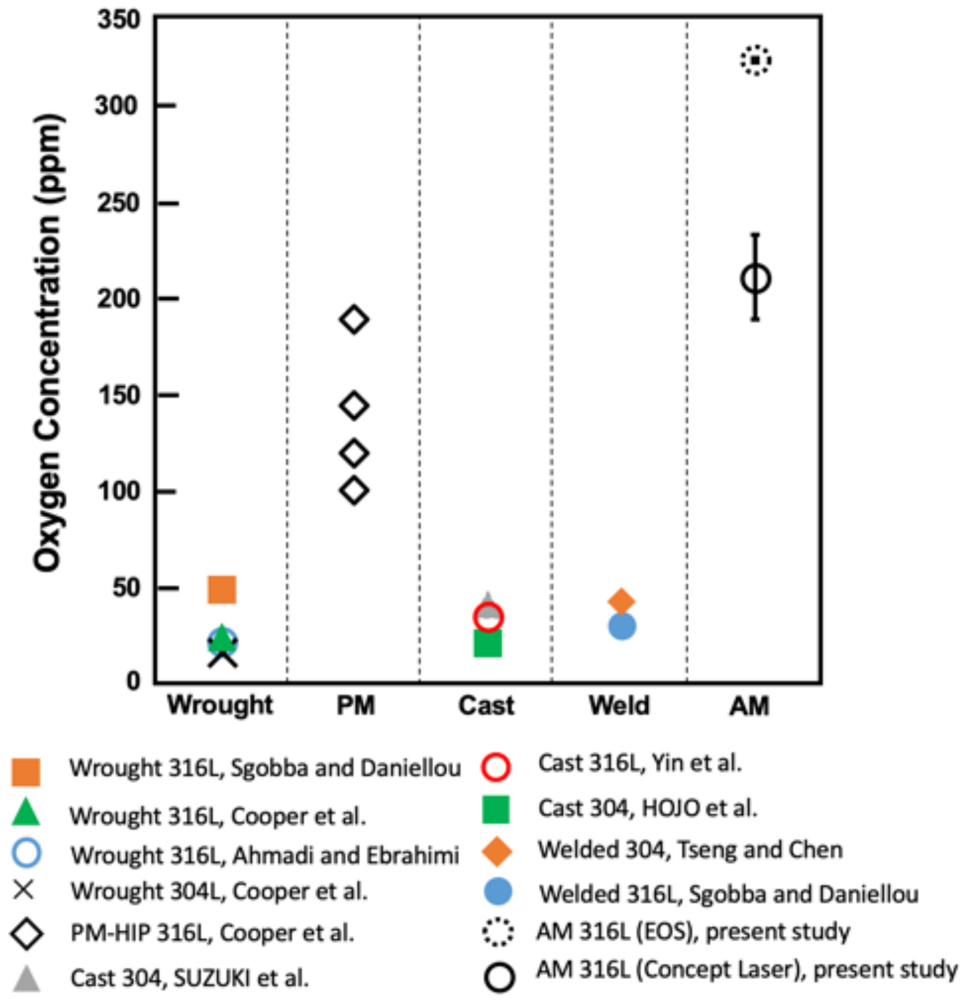

Fig 1 A comparison of oxygen concentration between wrought SS, PH-HIP SS, cast SS, welded SS and AM SS. Data obtained from literature including wrought SS, PH-HIP SS, cast SS and welded SS [28, 29, 40-45].

The typical microstructure and behavior obtained with AM 316L SS, including the directional columnar structure and cellular dislocation network, has been widely reported [12, 48, 49]. This work is aimed to build upon the knowledge of AM 316L SS by focusing mainly on the characteristics of oxide inclusions within the microstructures of these AM parts. Given the typical oxide inclusion size, their presence and distribution are best observed by TEM elemental mapping. Fig. 2 is a TEM image illustrating the size and distribution of oxide inclusions (gray dots) within a typical AM 316L SS sample. The image shows a high angle grain boundary (HAGB) and the associated sub-grain cellular structure that is commonly observed in AM 316L SS [5, 12, 14, 46]. Strong segregation of Cr, Mo, and Mn was found along the cellular walls and at the HAGB in the as-built AM 316L SS part. Nano-scale oxide inclusions, mostly Si and Mn-rich oxides ($MnSiO_3$), were found to be distributed along the grain and cellular boundaries. Fig. 3 shows a high resolution TEM image of an oxide inclusion located at a cellular boundary within the FCC SS matrix. The Cr and Mo segregation appeared to create a darker contrast around the particle. Selected area diffraction showed these nano-scale oxides are amorphous in nature. Although the particle was highly incoherent with respect to the matrix, no structural defect or void was visible along the particle/matrix interface.

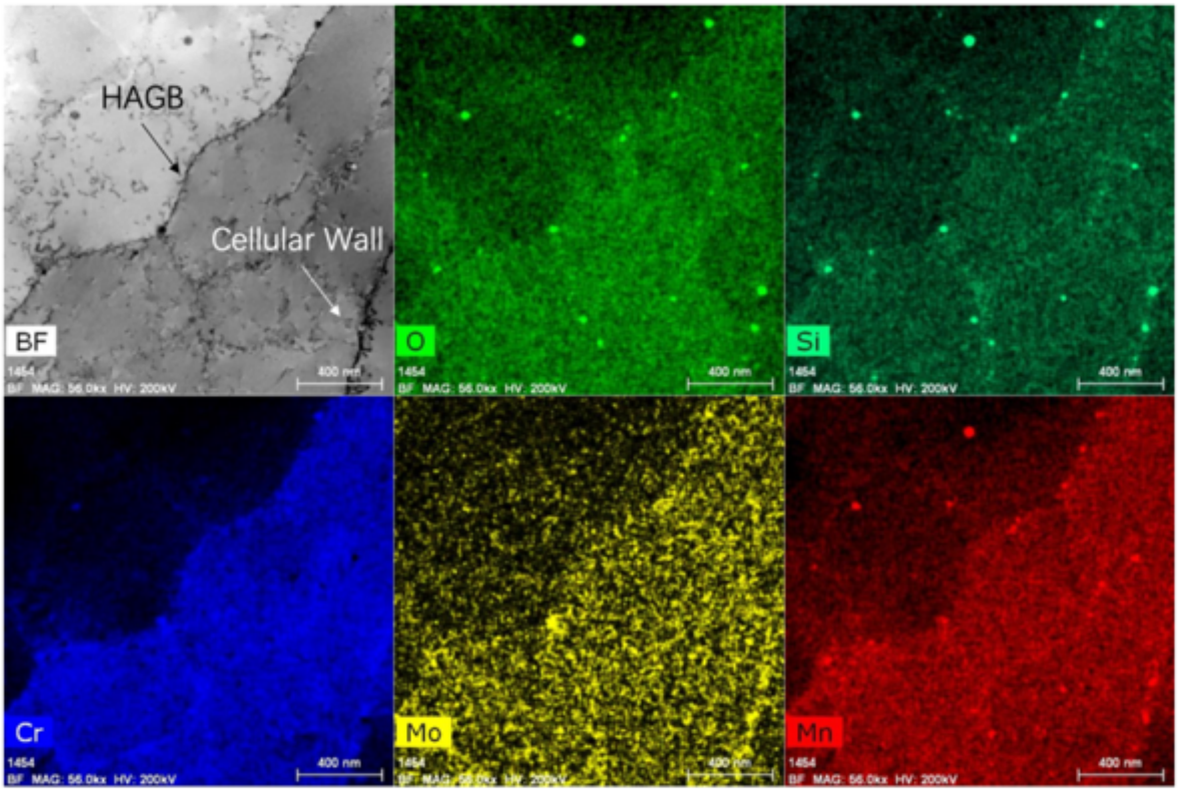

Fig 2 Electron micrograph of the cellular microstructure of AM 316L SS illustrating the location and distribution of nanoscale oxide inclusions in STEM-EDS elemental maps.

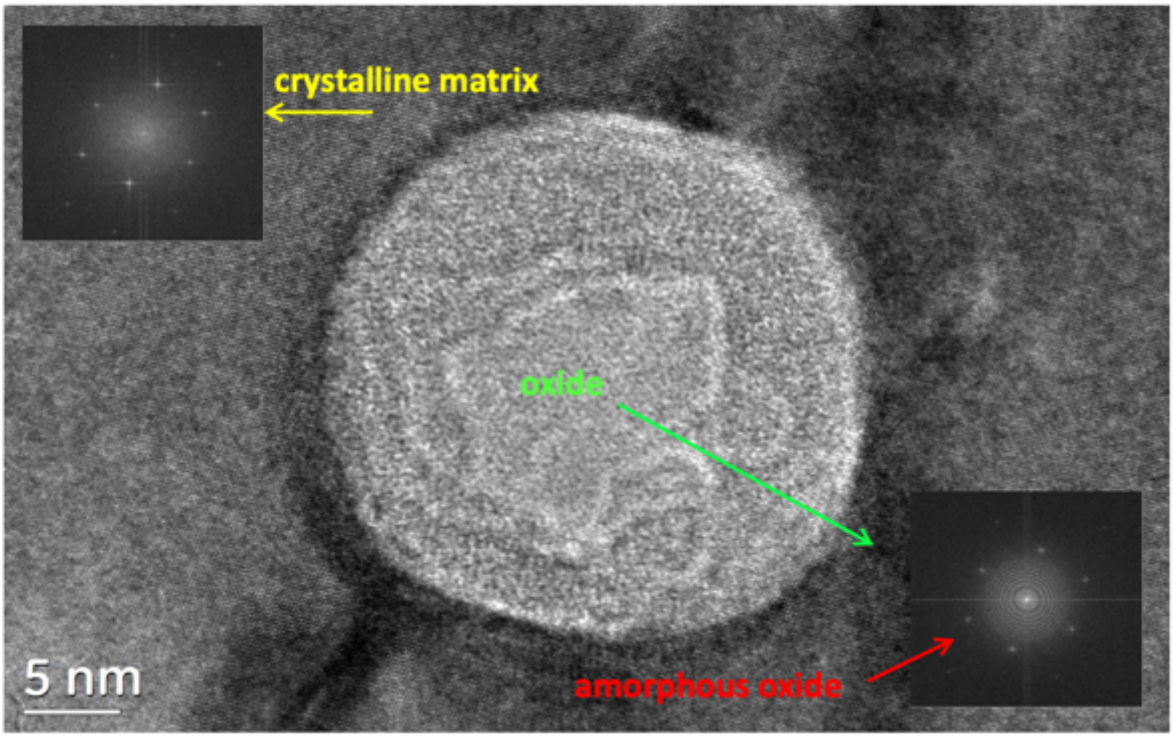

Fig 3 High resolution TEM image of a nanoscale oxide inclusion in the matrix of AM 316L SS. Included are the FFTs (Fast Fourier Transforms) for both the oxide and the matrix locations.

2.3.2 Oxygen transfer from precursor powder

As shown in Fig. 1, powder-based fabrication processes are prone to higher oxygen contamination. Fresh feedstock powders were obtained from two different manufacturers, Carpenter and GE, and characterized for oxygen content. The typical oxygen level in these powders ranged from 212 to 440 ppm, see Table 1. Figs. 4 (a) and (b) show TEM images with elemental maps for cross-sections of the as-received Carpenter powder. Both powder samples were very similar and possessed non-equilibrium microstructural components such as oxygen inclusions and elemental segregation. Both are likely a result of the extremely rapid cooling that occurred during solidification. The oxide inclusions appear to be composed of Si, Mn, P, Mo, and S. A high magnification zoom of the large inclusion of the left side is shown in Fig. 4 (b). The inclusion appears to be primarily composed of Si and Mn rich oxides that are enveloped by MnS. Oxide-sulfide complex inclusions are commonly observed in cast steels [50-52]. Wakoh et al. investigated MnS precipitation behavior and noted that MnS prefers to nucleate on $MnSiO_3$ oxide surfaces during solidification due to its lower melting temperature and higher sulfur capacity [50]. Shin et al. hypothesized that the formation mechanism of the oxide-sulfide complex could attribute to their low lattice disregistry [51]. Molybdenum phosphide and molybdenum sulfide also precipitated out adjacent to the Si-Mn-O-S oxide-sulfide complex. Kim et al. studied the effect of cooling rate on the morphology of oxide-sulfide complex inclusions in Si/Mn deoxidized steels [52]. Their work noted that both the size and precipitation ratio of the MnS phase in the oxides decreased with the increasing cooling rate. The cooling rate of gas atomized droplets and liquid melt pool for L-PBF process are 10^5 to 10^6 K/s [53] and 10^6 to 10^7, respectively [54]. The L-PBF process induces massive heat into precursor powder and creates rather small melt pools (*ca.* 100 μm in width and 80 μm in depth) with a peak temperature well above melting points of all components. Thus, oxides and sulfides may dissociate and re-nucleate during rapid solidification. Furthermore, the oxides observed in AM 316L SS parts were likely due to (1) the much lower Gibbs free energy of Si and Mn oxide formation over other inclusions, and (2) the high oxygen concentration present in the AM material. The redistribution/introduction of oxygen during ultrafast laser melting significantly reduced the chance of MnS formation. This happenstance can actually improve pitting corrosion resistance of SS, as reported elsewhere [55, 56].

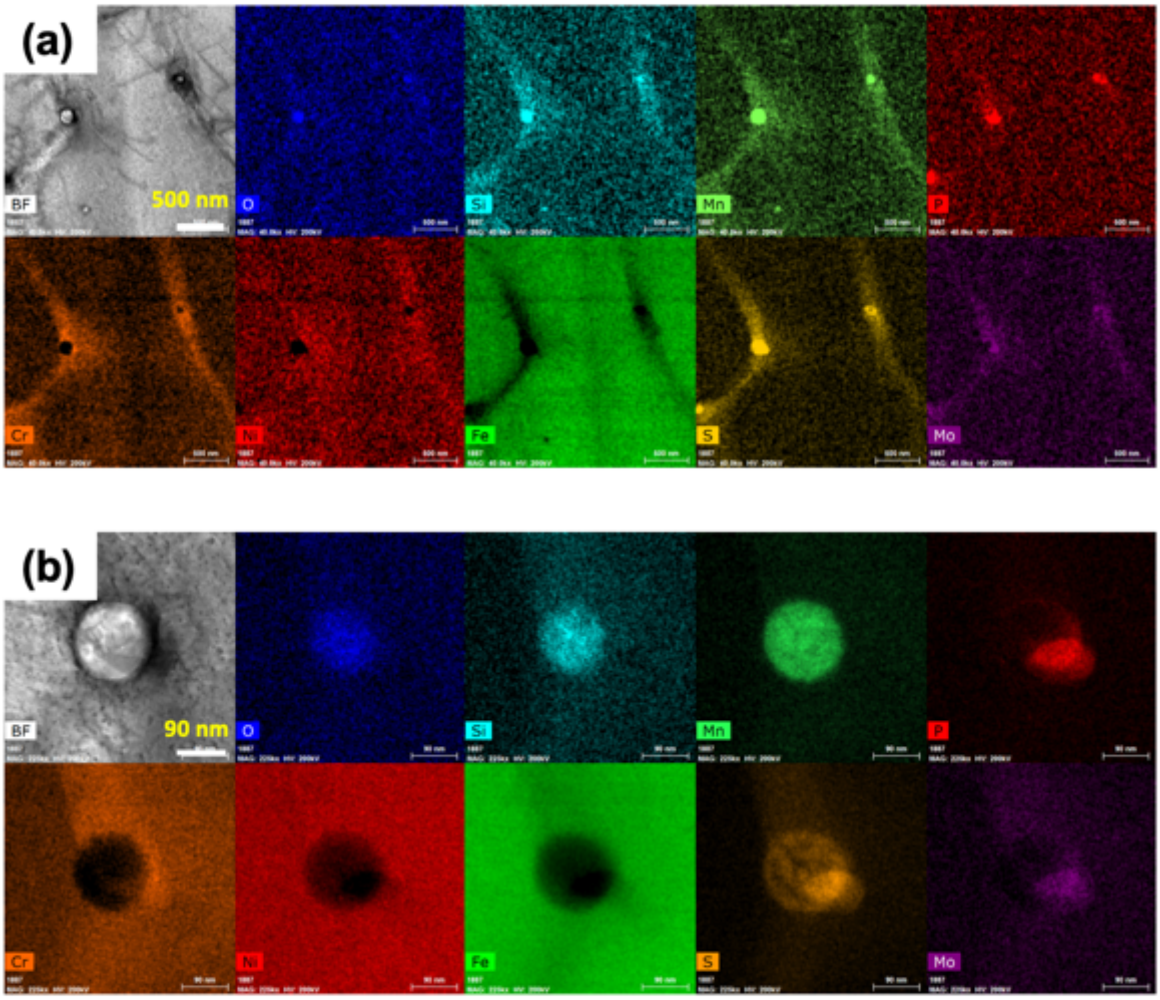

Fig 4 STEM-EDS elemental mapping displays composition and morphology of inclusions in precursor 316L Stainless Steel powder, (a) is low magnification (40000x) and (b) is high magnification (225000x).

In this study, two different precursor powders and two different AM systems were employed to assess the process-to-process and machine-to-machine variability of oxide inclusion formation. The Carpenter powder was processed in an EOSINT M270 unit and the GE powder processed in a Concept Laser Mlab LaserCusing® unit. Back-scattered electron (BSE) imaging was utilized for analysis here due to its desirable contrast difference between the oxide inclusions and metal matrix. BSE images of cross-sections of the precursor powder from Carpenter and a part printed from it in the EOS M270 SLM system are shown in Fig. 5. In both, the Carpenter/EOS and GE/Concept

Laser cases, the powder contained larger, but fewer oxide inclusions than in the AM part.

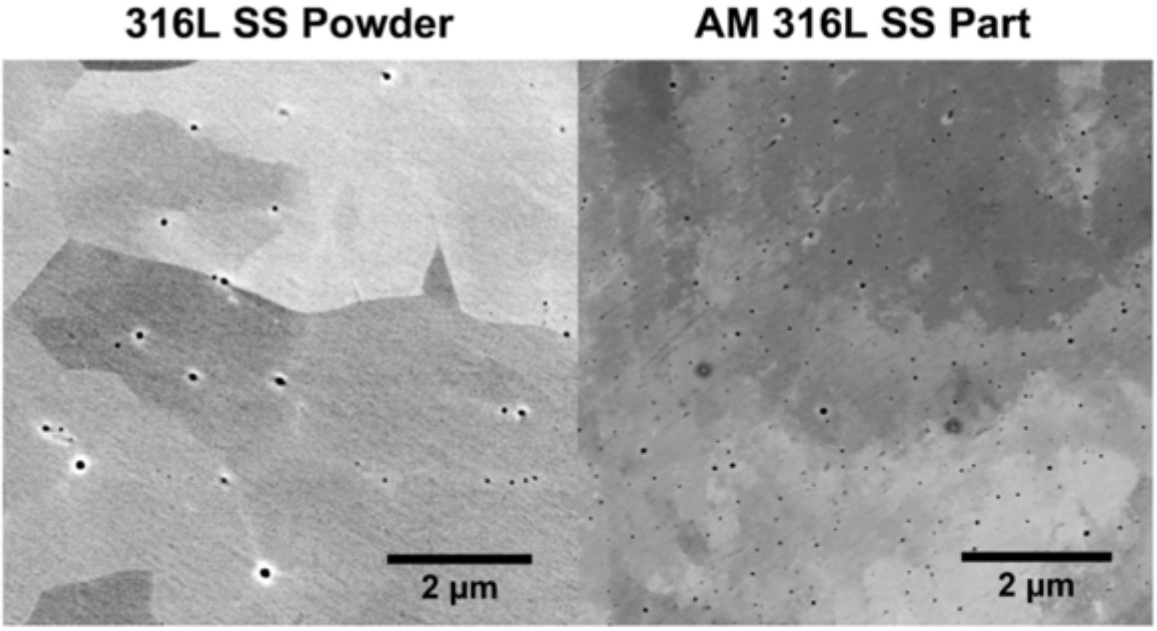

Fig 5 Back-scattered electron image comparison between 316L SS precursor powder and AM 316L SS Part.

The volume fraction and average inclusion size were determined from fifteen measurements on each sample and are shown in Fig. 6. Here, the error bars represent the standard deviation. Both powder/machine combinations produced very similar results. The AM processed parts exhibited somewhat lower oxide volume fractions as compared to the precursor powders. The AM parts also contained significantly smaller inclusion sizes with a distinct Gaussian distribution; whereas, the powder distributions were rather scattered, see Fig. 7.

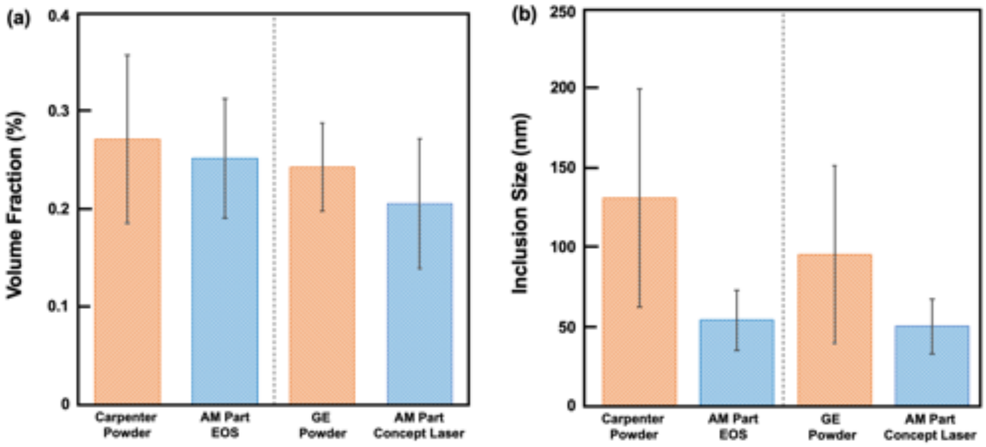

Fig 6 Comparison of (a) oxide inclusion volume fraction, and (b) average oxide inclusion size of 316L SS produced by the Carpenter/EOS and GE/Concept Laser combinations. Measurements were obtained from BSE (backscattered electron) images by using ImageJ software.

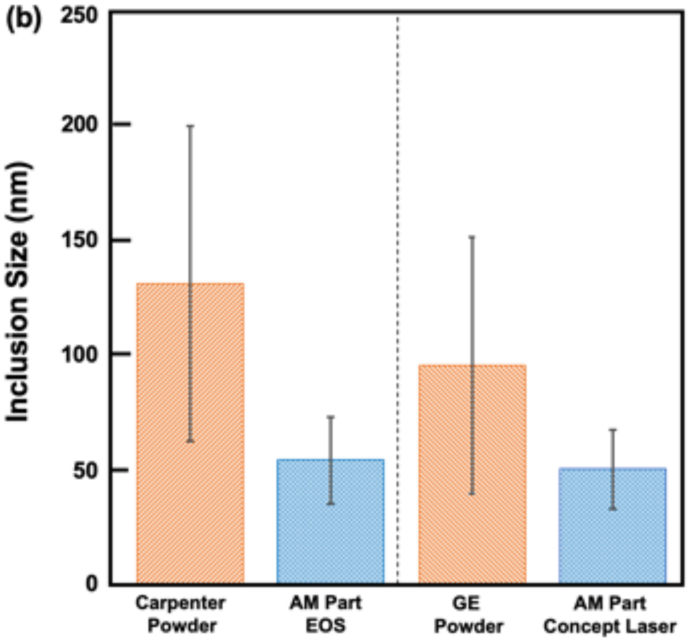

Fig 7 Histogram comparing the inclusion size distribution between precursor powder and AM part for the GE/Concept Laser combination.

The ultrafine oxygen inclusion formation exhibited by the AM processed parts was likely due to the rapid cooling rate of the L-PBF process, which was higher than that of the inert gas atomization process used to produce the powders. Furthermore, $MnSiO_3$ (Rhodonite) has a melting point of approximately 1596 K [57], which is well below the peak temperature developed inside the melt pool. The appreciably smaller inclusion size indicated that the majority of nano-scale oxide inclusions in the AM part were formed by the dissolution and re-precipitation of oxides in the precursor powder. The relative differences in oxygen and carbon content between the two (Table 1) suggest some oxygen was released during the laser process along with carbon, possibly in the form of carbon oxides (CO/CO_2). Table 1 also indicated the nitrogen pick-up in two AM parts came from the remaining nitrogen gas in the atmosphere [58].

An additional consideration of oxygen contribution from the precursor powder is the oxide layer existing on the powder surface. TEM/EDS characterization indicated this layer was approximately 3 nm thick, see Fig. 8 (a). This thickness was consistent with an auger electron spectroscopy (AES) depth profile shown in Fig. 8 (b), determined based upon an oxygen concentration drop-off of 60% of the initial value. It can be noticed that the surface oxides were composed of iron oxide at the outmost surface, as indicated by Fe profile in Fig. 8(b), and chromium and nickel oxides were underneath. The composition of oxides was also manifested by TEM elemental mapping in Fig. 8(a). Since the analysis was performed on the fresh powder received from powder vendor, it is reasonable to conclude this thin layer of oxide was mainly formed during inert gas atomization. A theoretical calculation based upon this oxide layer thickness suggested that the surface oxygen would only contribute approximately 10 ppm to the overall oxygen content in the final AM part. Thus, surface oxides in the fresh 316L SS powder made only a negligible contribution to the formation of nano-scale inclusions in the AM parts.

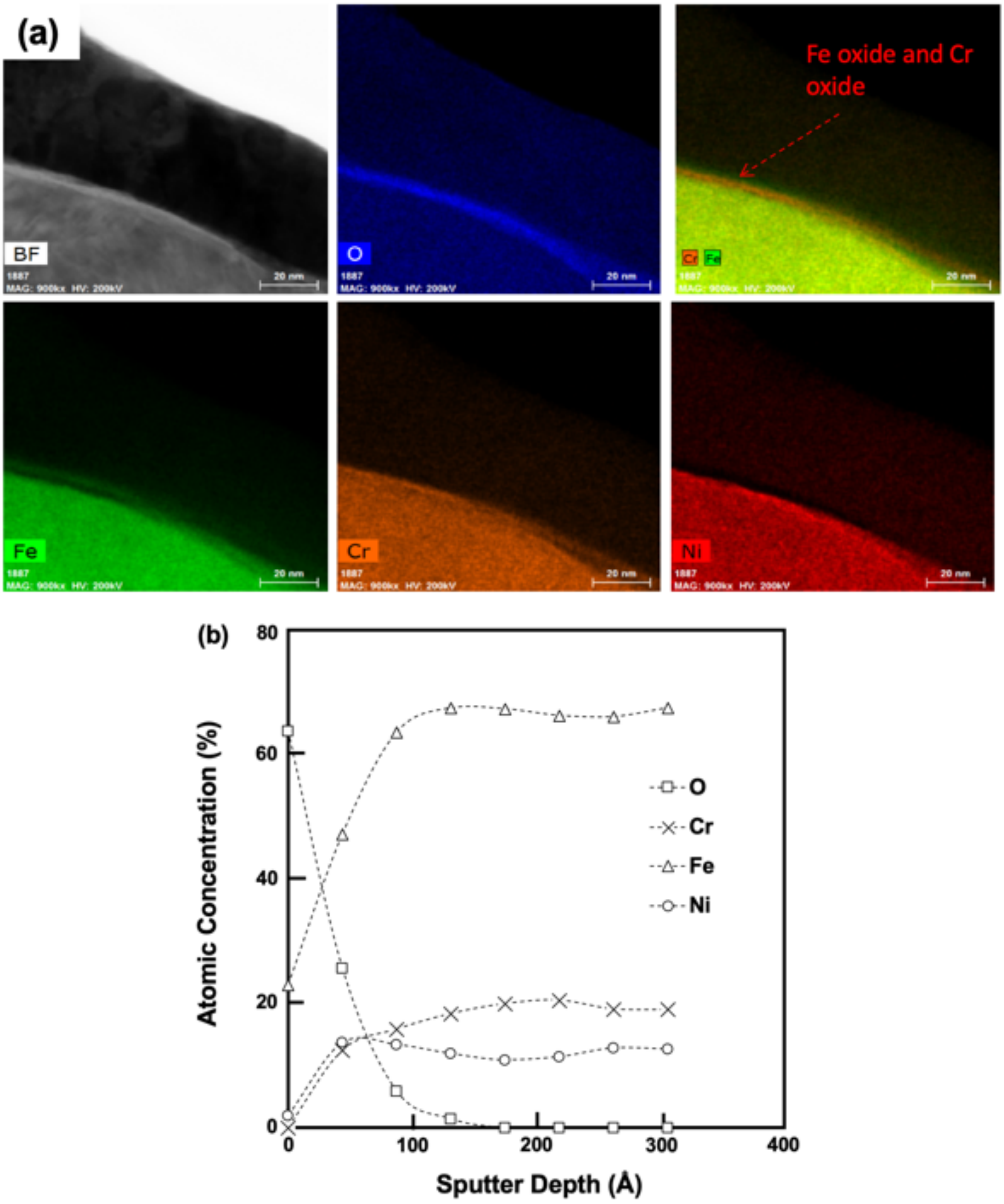

Fig 8 Measurement of 316L SS powder surface oxide layer thickness: (a) STEM image and STEM-EDS mapping of the surface of the precursor powder, and (b) Auger electron spectroscopy (AES) depth profile.

2.3.3 In-situ oxygen gettering and oxidation during L-PBF process

Although most commercial L-PBF AM systems are equipped with an inert gas purging system, it can take a significantly long time to achieve a suitable low oxygen partial pressure environment. The potential of oxygen gettering during L-PBF has been addressed to a degree in the literature [59, 60]. However, there have been no systematic studies that quantify this effect. For reactive metals, like Al and Ti, the effects of oxygen contamination during the laser process can significantly impact the part quality. Where and how oxygen from process environment transfers into AM parts has not been resolved. To this end, six 316L SS samples were processed by L-PBF at different controlled oxygen levels between 0.0 % and 1.0 % oxygen. The density of these AM parts was measured following ASTM E2109 [39] and did not appear to be influenced by the chamber oxygen level, Fig. 9 (a). However, the volume fraction of oxide inclusions did appreciably increase with the chamber oxygen level, Fig. 9 (b). While the average inclusion size only negligibly increased with oxygen level, the oxygen concentration increased significantly, Fig. 9 (c) and (d) respectively. This is a clear indication that extraneous oxygen in the chamber can be incorporated into solidified parts during L-PBF. Furthermore, the increased oxygen content in the AM parts manifests as a higher number/density of oxide inclusions.

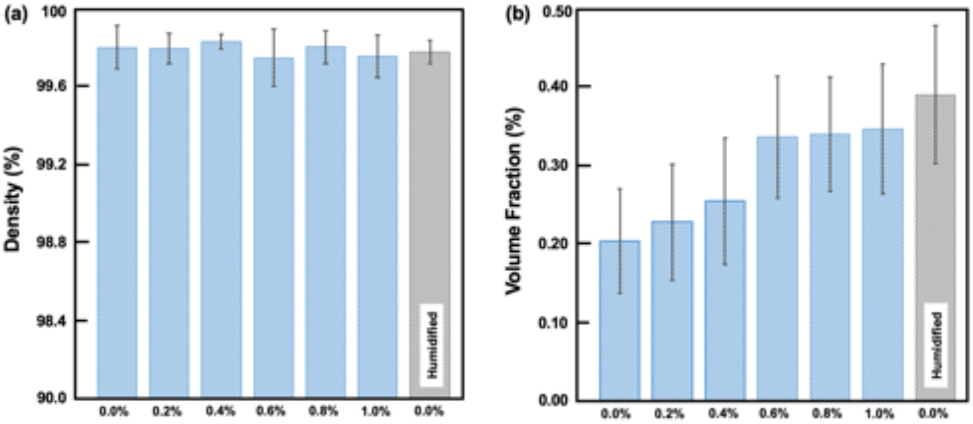

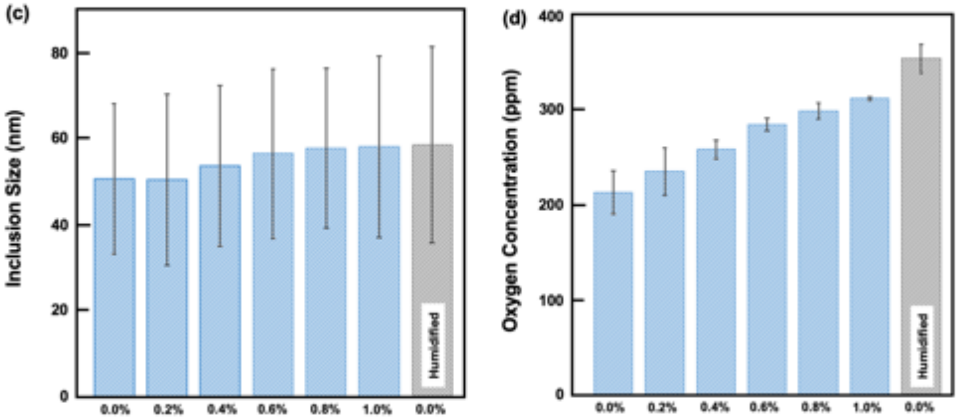

Fig 9 Comparison among 316L SS AM Parts fabricated under different chamber oxygen levels and with humidified powder: (a) density of AM parts; (b) volume fraction of oxide inclusions in AM parts; (c) average inclusion size in AM parts and (d) oxygen concentration in AM parts.

The incorporation of extraneous oxygen in the environment into the melt pool of the L-PBF process can occur by two basic mechanisms, oxygen uptake at the melt pool surface and amalgamation of oxygen-containing spatter particles depositing onto the part. The high-energy interaction of the laser with the powder bed generated molten droplets or spatter particles that were ejected from the melt pool in a direction opposite to the laser movement [61-63]. Some of these droplets fell back onto the printing surface after traversing through the chamber atmosphere. During this time, they could absorb oxygen from the atmosphere, which then was incorporated into the build with subsequent laser melting. Figs. 10 (a) and (b) are electron micrographs illustrating oxide formation on the melt pool surface and on the spatter particles respectively. High oxygen affinity elements, such as silicon and manganese, will likely exist at or near the melt pool surface. The elemental mapping shown in Fig. 10 (a) confirms that they indeed reacted with environmental oxygen to form inclusions on the surface. In turn, the highlighted spatter particle in Fig.10 (b), approximately 120 µm in diameter, provides the evidence that these particles indeed fell back and become partially sintered on the as-built surface. The oxide spots on the surface of the spatter particles were not observed from the fresh powder. The elemental mapping here indicates the oxides are composed of silicon and oxygen, which is consistent with the literature

[61, 64-68]. Gasper et al. investigated the spattering and oxide formation in Inconel 718 manufactured by L-PBF and concluded that oxides on the spatters' surface originated from the melt pool surface oxidization before the ejection of spatters [60], which is likely the case here.

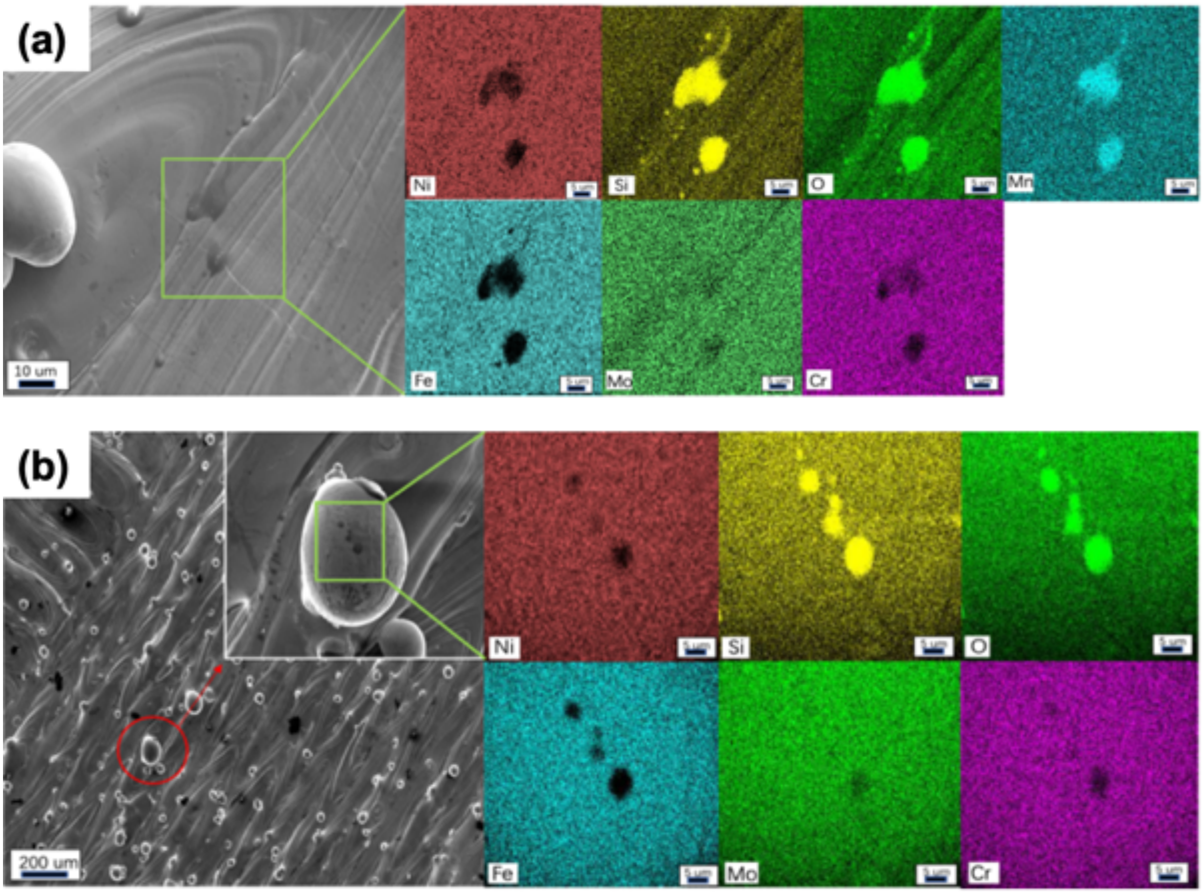

Fig 10 Electron micrographs and elemental mapping of oxide inclusions (a) on the surface of the melt-pool; and (b) on a spatter particle.

To further investigate whether the spatter particles can absorb additional oxygen from the processing environment, AES characterization was carried out to obtain the depth profiles of oxygen content, see Fig. 11 for the particles produced in 0% (a) and 1% (b) oxygen environments. Here, several particles of each oxygen level were characterized, showing identical profiles. The results indicate that significant surface oxidation took place on the spatter particles in the high oxygen environments. In fact, spatters exposed to the 1% oxygen environment had an oxide layer thickness of 297.5 ± 75 nm, which was 10 times that of the 0% environment (27.2 ± 1.1 nm) and 1000 times that of the fresh precursor powder (3 nm) shown in Fig. 8. Furthermore, this oxide appears to be composed of iron, nickel and chromium , different from the surface oxides seen on the spatters in Fig. 10 (b). Given the consistent values on multiple samples, this oxide layer appears to cover the entire spatter surface. It likely represents the molten droplets absorbed the oxygen and formed Fe/Ni/Cr oxides while traversing through the process environment. This extra oxygen is also reflected in the oxygen concentration measurements on the spatter particles, shown in Fig. 12. The oxygen content in the spatter rose sharply with oxygen content in the process environment, with the 1% spatter absorbing approximately 15 times more oxygen than the fresh precursor powder.

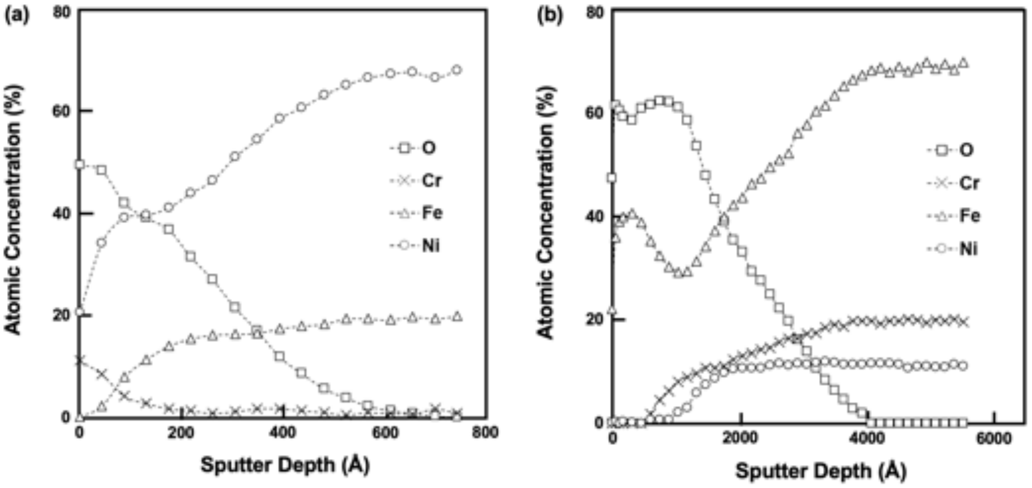

Fig 11 Auger electron depth profile of surface oxides on spatter particles for oxygen content environments of (a) 0.0% (b) 1.0%.

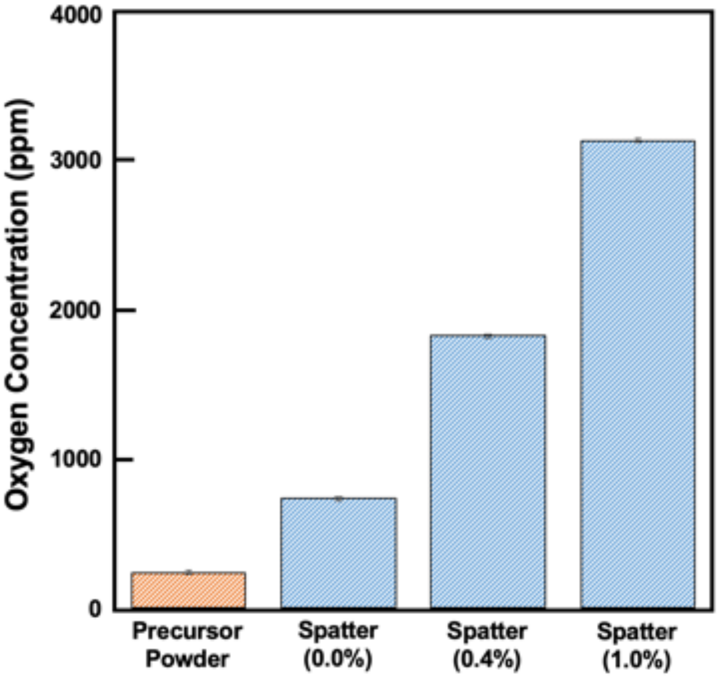

Fig 12 Comparison of the oxygen concentration between the precursor powder and spatter particles collected at different oxygen content environments.

It is also important to assess the oxide inclusions within the spatter particles produced at different oxygen level environments. The analysis of oxide inclusions in spatter particles showed they contained very similar interior inclusion sizes and volume fractions, as was observed in the AM parts. Overall, the volume fraction of interior oxide inclusions in the spatter particles was approximately 2 times higher than the fresh precursor powder. This indicates that the increase in AM part oxygen concentration with oxygen content in the process environment shown in Fig. 9 (d) resulted primarily from surface oxidation of spatter particles. Considering the extremely short melt pool residence time and limited contact between melt pool surface and atmosphere, we conclude that the oxygen intrusion during L-PBF is dominated mainly by the incorporation of the oxidized spattered powder back into the melt pool. In addition, the spattered powder remained in the feedstock powder can increase the oxygen content in the recycled powder [30].

2.3.4 Effects of moisture pickup and oxidation during long-term storage

Another mechanism that can introduce oxygen into an AM part is the potential of moisture contamination during powder transportation and storage. An accelerated study was carried out to evaluate the effects of moisture pickup on the quality of the printed AM parts. In this study, fresh powders were stored in an enclosed environmental chamber at a temperature of 28 ℃ with 80% relative humidity for a month before AM printing under the 0% oxygen environment. It should be noted that the humidity level is higher than normal storage conditions (generally 30%-60% in air). The flowability of the humidified powder was compared to the fresh powder in a rheometer. Figs. 13 (a) and (b) show the applied shear stress and basic flowability energy (BFE) for each. Shear properties showing in Fig. 13(a) indicates that how easily a consolidated and resting powder will begin to flow. The shear head applies normal stress on powder bed, and once the required stress established, shear head begins to rotate slowly until the powder bed shear, maximum shear stress are recorded. This situation is at some extent similar to powder spreading process in SLM applications, and therefore can be desired method for evaluating powder flowability. Stability results given in Fig. 13(b) represent the energy consumed for conditioning (stiring thoroughly to obtain an even distribution of powder) the powder with the same blade tip speed, higher energy consumption relates to lower flowability. The elevated shear stress and BFE suggest that the humidified 316L SS powder showed a slightly degraded flowability than fresh powder. This may not play a significant role here as the density of AM parts made from humidified powder showed very similar densities of 99.79% and 99.77%, respectively, see Fig. 9 (a). This could be attributed to a relatively large powder supply in this work. The oversupply of the feedstock powder during printing filled up the lack of fusion induced by the degraded flowability of humidified powder. Analysis of the oxide inclusions they contained, including volume fraction, inclusion size and oxygen concentration, were also shown in Fig. 9 and the gray colored column. The results confirmed that moisture contamination can introduce additional oxygen into AM parts and lead to more oxide inclusions. The sources of oxygen from humidified powder leading to the high volume fraction of oxides are: (1) surface oxidation during the exposure of powder at high humidity environment; (2) residual moisture remained in the humidified powder could be dissociated at extremely high peak temperature in the melt pool. The average inclusion size from the humidified powder was somewhat larger than that observed with the fresh powder, suggesting a possible coarsening mechanism of oxides due to the collision coalescence mechanism, which has been studied for the casting process [42].

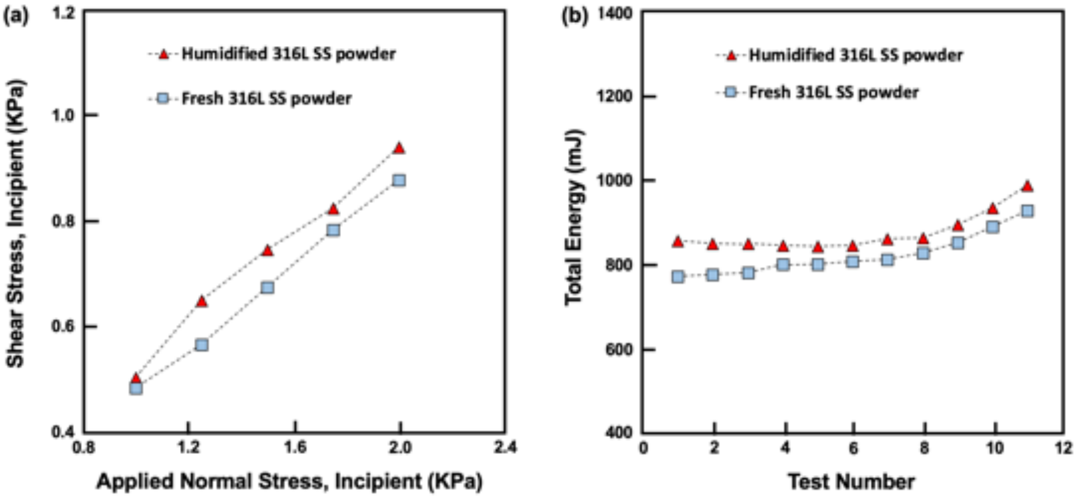

Fig 13 Comparison of fresh and humidified 316L SS powder: (a) Shear properties, and (b) Basic flowability energy. Measurements done by using Freeman Technology FT4 powder rheometer.

2.3.5 Si/Mn free AM 316L Stainless Steel

The presence of oxide inclusions in AM 316L SS has been linked to initiation sites for fracture failure [14, 29, 69]. In the fabrication of 316L SS, Si and Mn are normally added as deoxidizers to gather oxygen. The results of this work showed that these oxygen getters end up as components of the oxide inclusions in the final AM parts. By utilizing ultrapure feedstock materials and state-of-the-art inert gas atomization facilities, the oxygen level can be well controlled without adding deoxidizers. To investigate the possibility of producing AM parts with fewer oxide inclusions, Si/Mn free 316L SS powder was prepared by Carpenter under a low oxygen processing condition, and corresponding AM parts were fabricated by the Concept Laser system. The chemical composition of Si/Mn free powder was shown in Table 1, in comparison to regular 316L SS powder. A slightly elevated oxygen level was observed in the Si/Mn free powder. BSE images of Si/Mn free 316L SS cross-section from fresh powder and the fabricated AM part are shown in Fig. 14. Prismatic shape inclusions (not spherical shape) were found in both matrixes. An EDS analysis of inclusions in both are shown in Fig. 15 and confirmed that they were chromium-rich oxides. The inclusion type was in agreement with the Ellingham diagram where chromium has the highest oxygen reactivity in this material. Hence, even without oxygen getters like Si and Mn, oxide inclusions still formed in L-PBF manufactured 316L SS.

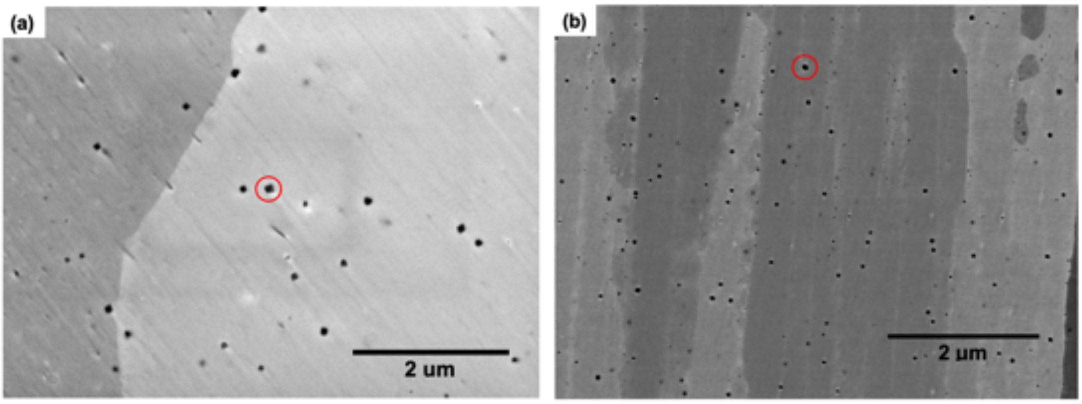

Fig 14 Back-scattered electron image comparison between (a) Si/Mn free 316L SS powder, and (b) AM part.

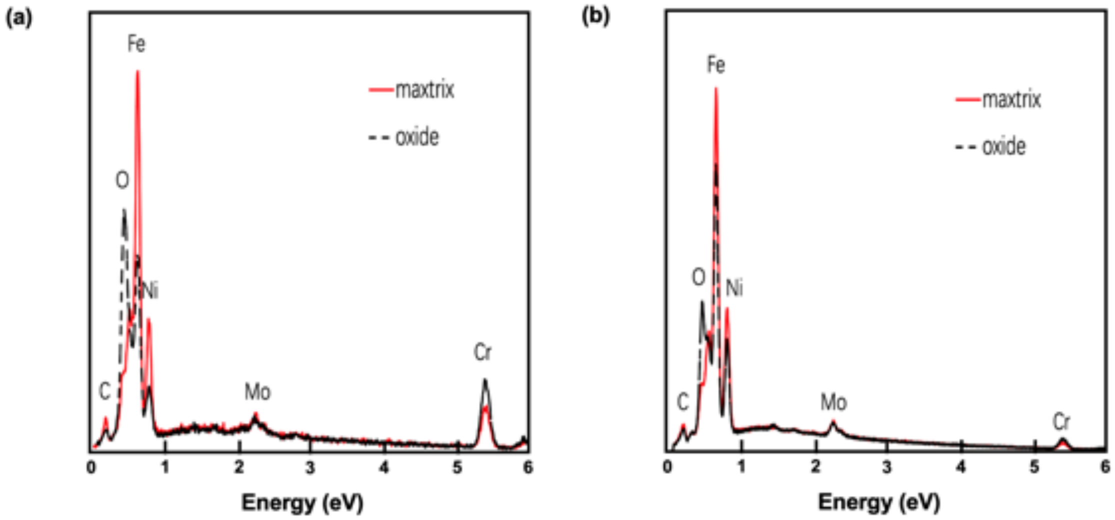

Fig 15 EDS spectrum comparison of oxide inclusions between (a) Si/Mn free 316L SS powder, and (b) AM part.

The volume fraction and average size of the inclusions in precursor powder and AM part are shown in Fig. 16. A slight drop of oxide volume fraction was observed in AM parts in comparison to its precursor powder. Although Cr rich oxides, in general, have a higher melting point than $MnSiO_3$, they experienced the same process of dissociation and re-precipitation during laser melting. The average size of the Cr rich oxides (80 nm) in Si/Mn free 316L SS powder was smaller than that of the Si/Mn rich oxides in regular 316L SS powder (131 nm and 96 nm in this work). It is worth noting that the final AM part made with Si/Mn free powder exhibited a slightly higher oxide volume fraction and larger inclusion size than the AM part made with regular powder. This suggests that collision coalescence coarsening during gas atomization was different than laser AM process. The Charpy impact toughness at room temperature of as-built AM 316L SS printed with regular powder and that of as-built AM 316L SS printed with Si/Mn free powder are 163± 12.78 J and 116 ± 12.73 J, respectively. Therefore, the switch to Si and Mn free chemistry will reduce the fracture resistance of the AM 316L SS.

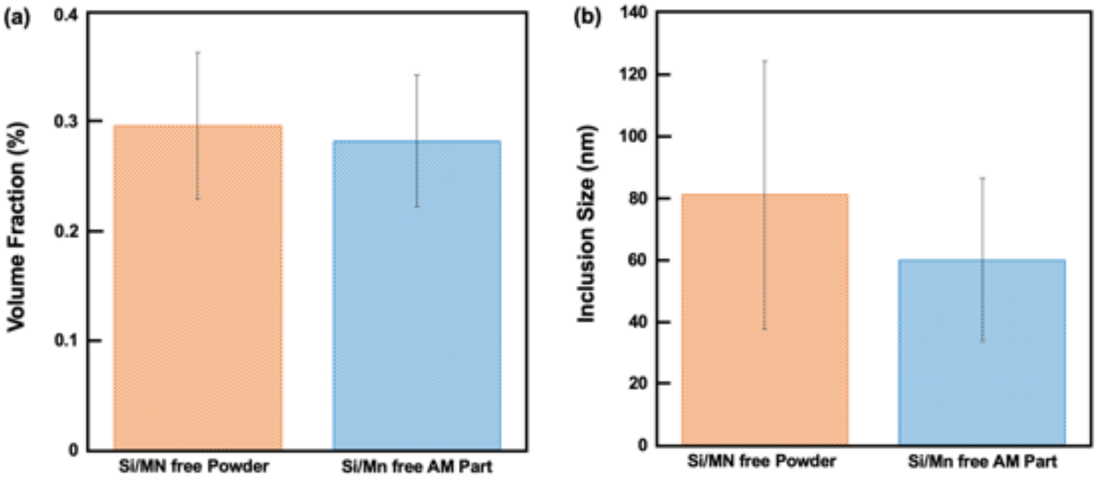

Fig 16 Comparisons of (a) oxide inclusion volume fraction, and (b) average oxide inclusion size, between Si/Mn free 316L SS powder and AM part.

2.3.6 Mechanical response and grain boundary pinning effect due to nano oxides

Vickers Hardness testing was performed on all AM 316L SS parts produced in this work, shown in Fig. 17. The orange and blue data represents the samples printed in different chamber oxygen levels, 0.0 to 1.0 %. Little to no difference in hardness was observed for these samples.

The Si/Mn free AM 316L exhibited lower hardness, which may be due to the lower amount of carbon and manganese as compared to regular powder [70]. It is worth noting that an interesting observation of the reduced hardness was captured in the AM part printed with humidified powder. The reason behind the reduction of hardness of AM part printed by humidified powder is still under investigation. Tensile properties of as-built and annealed AM 316L SS fabricated at 0% and 1.0% oxygen content environments were compared, as displayed in Fig. 18. Three specimens were tested for each condition. AM 316L SS printed 0% and 1.0% oxygen content environments exhibited consistent yield strength, ultimate tensile strength and percent elongation for both as-built and annealed circumstances. Fracture surface of tensile speciments were shown in Fig. 19, typical ductile fracture was observed for both as-built and annealed specimens. Inclusions were found in dimples of all fracture surfaces, as indicated by red arrows. The comparison of fracture topography of as-built and annealed specimens indicated that pores and defects are more prone to initiate cracks in as-built AM 316L SS than annealed AM 316L SS. The Orowan strengthening model, as listed below, was employed to estimate the contribution of oxide inclusions to the overall strength,

$$\tau = Gb/(L-d) \qquad (1)$$

Here G is shear modulus, b is Burgers vector, L is average inter-particle distance and d is the average diameter of particles. Under the assumption that oxides were uniformly distributed in the material, AM 316L SS printed in 1% oxygen contributed approximately 38 MPa of shear strength (using G = 78 GPa, b = 0.258 nm, L = 0.64 μm and d = 115 nm), which was negligible compared to its yield strength. Therefore, the environmental oxygen that was transferred into the AM parts is not likely to significantly strengthen AM 316L SS and also not to deteriorate the ductility. This conclusion is consistent with other reported work [12].

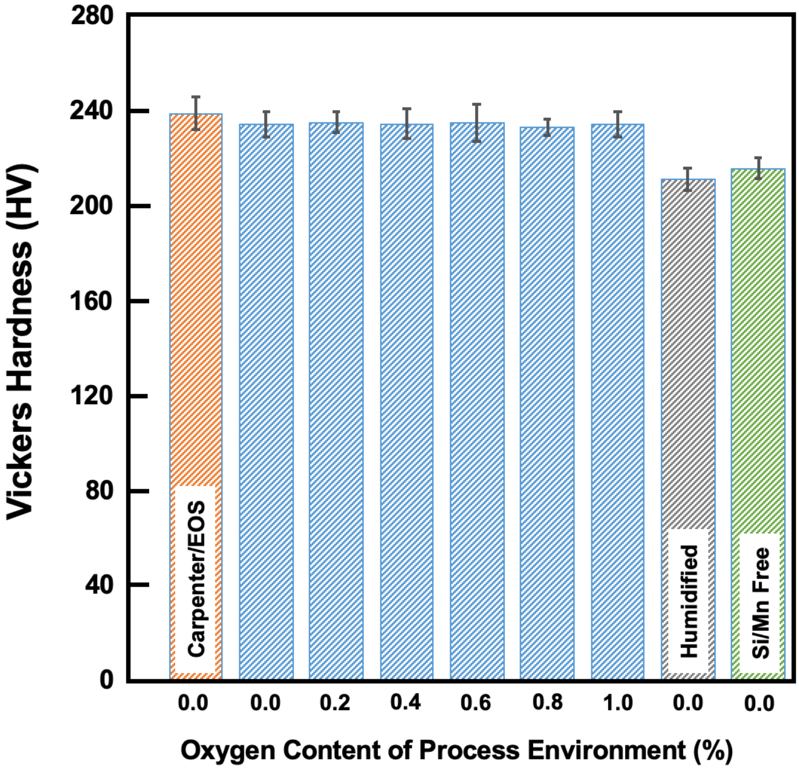

Fig 17 Vickers hardness results comparing all AM samples from 316L SS in this work.

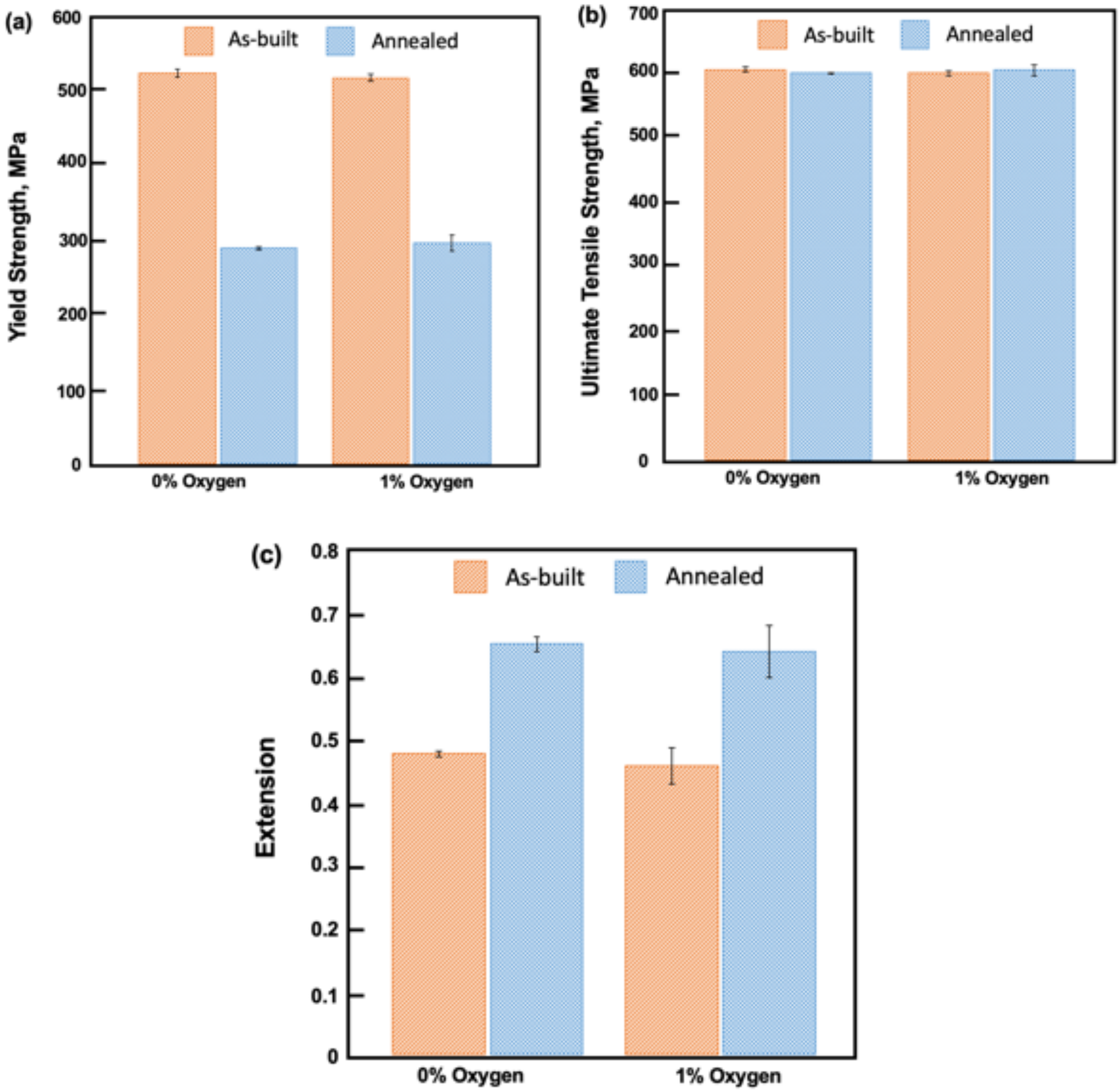

Fig 18 Comparisons of (a) yield strength, (b) ultimate tensile strength, and (c) extension, between as-built and annealed (1150 ℃ for 2hr) AM 316L SS produced at 0% and 1% oxygen content environment.

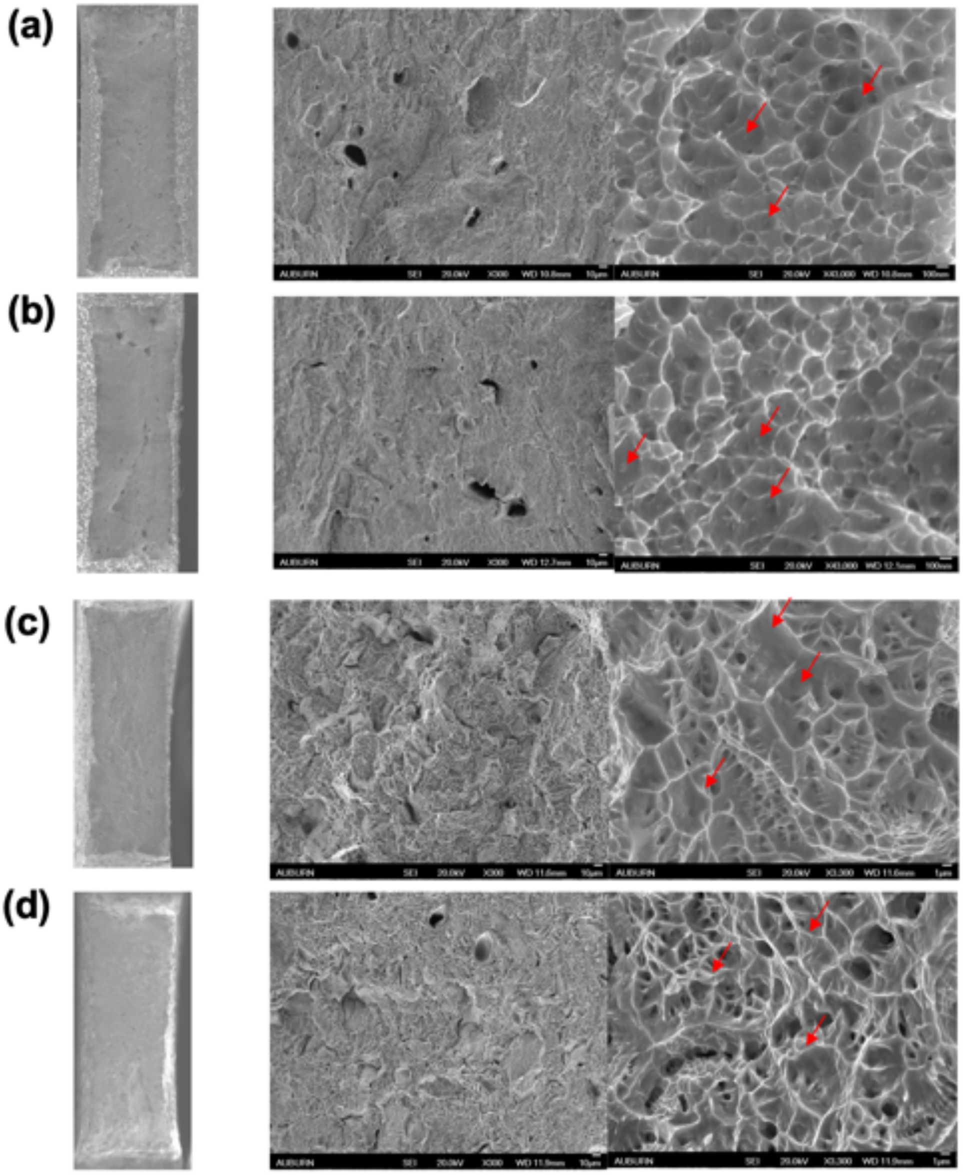

Fig 19 Fracture surface of as-built AM 316L SS produced at (a) 0% and (b) 1% oxygen content environment; annealed AM 316L SS produced at (c) 0% and (d) 1% oxygen content environment. Red arrows point the inclusion inside dimples.

The higher amount of oxide inclusions may affect the material's toughness has been widely reported [14, 28, 29, 46]. The Charpy impact toughness of as-built AM 316L SS specimens were presented in Fig. 20, as compared with wrought and PM-HIP counterparts. AM 316L SS printed with Si/Mn free powder revealed particularly lower toughness than all other part, which could be attributed to the weaker interface between prismatic shape chromium inclusion and matrix. The AM 316L SS printed at 0%, 1% oxygen content environment, and AM 316L SS printed with humidified powder, although they have the maximum of approximately 2 times difference in volume fraction of oxide inclusions, the toughness was not affected. This is consistent with the work done Cooper et al., they investigated the effect of oxygen content upon Charpy impact toughness of 316L SS manufactured by PM-HIP and observed that oxygen concentration in HIP'd steels has little effect on the fracture toughness when the concentration value exceeds 200 ppm [28].

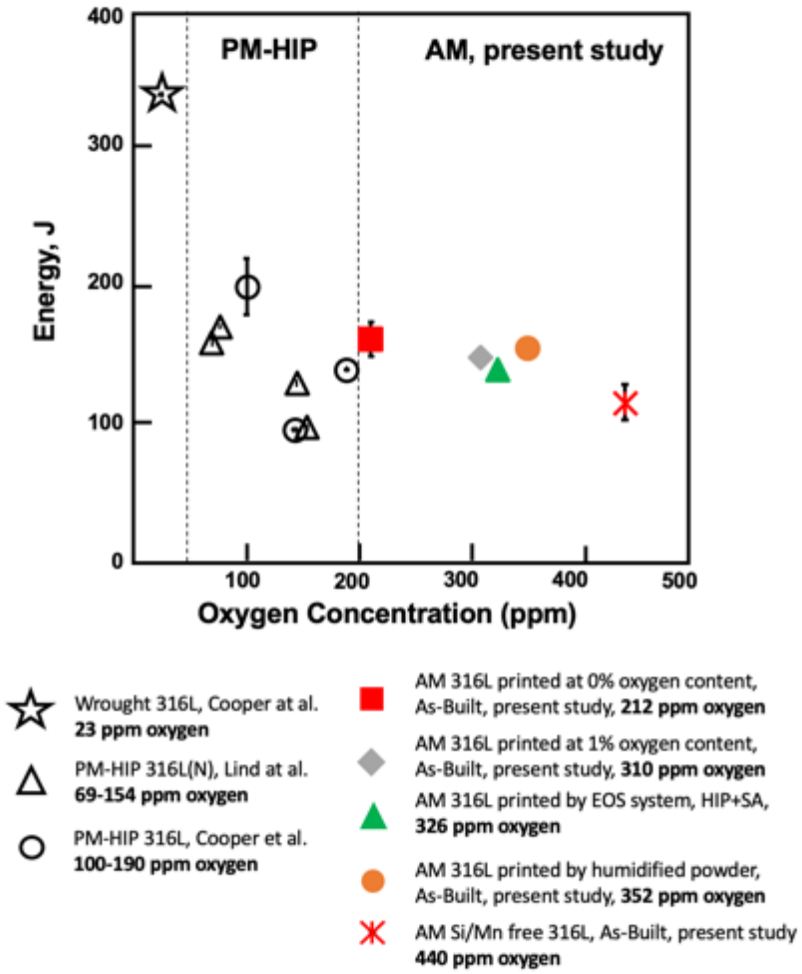

Fig 20 Comparisons of Charpy impact toughness of as-built AM 316L SS with wrought and PM-HIP counterparts.

2.3.7 Effects of oxygen content on melt pool

Surface active elements such as [O] and [S] have significant impacts on metals. In present work, the oxygen content in all 316L SS specimens is several times higher than sulfur content, as shown in Table.1 and thus [O] plays a dominant effect. Oxygen affects the surface tension σ and also the temperature dependency of surface tension $(\partial\sigma/\partial T)$, which determines the direction of Marangoni convection [71]. Changes in the direction of Marangoni convection lead to different shapes of the melt pool [72]. A positive temperature coefficient of surface tension $(\partial\sigma/\partial T)$ results in an inward flow of molten liquid and hence leading to a deep and narrow melt pool. On the contrary, a negative temperature coefficient of surface tension $(\partial\sigma/\partial T)$ leads to outward flow, and as a result, causing a shallow and wide melt pool. The laser beam usually melts several layers of powder materials for LPBF process to obtain highly dense parts. The variation of melt pool shape deviates from optimum density. Although the AM parts contain different oxygen contents ranging from 212 ppm to 352 ppm have shown not to affect its density, as displayed in Fig. 9(a), things can change when oxygen content exceeds a specific value. In order to investigate the effects of high oxygen content in 316L SS on LPBF melt pool and resulting part density, 316L SS powder was ball milled with 0.4 wt% and 1.0 wt% of nano -size molybdenum trioxide to introduce oxygen. The resulting AM parts contain approximately 1722 ppm and 3722 ppm oxygen, respectively. All parts were fabricated using the same process parameter. The AM parts were then cut parallel building direction and polished to measure the density using optical microscopy, as shown in Fig.21. Lower density and a higher number of pores and defects were observed on AM 316L SS with high oxygen content. The specimens were electro-etched by 10% oxalic acid at 10 V DC voltage to reveal melt pool geometry, optical micrographs of parts with minimum and maximum oxygen were presented in Fig. 22. Broader and shallower melt pool were revealed in high oxygen content AM 316L SS which results in incomplete overlapping between melts pools and leads to lack of fusion defects as indicated by red arrows in Fig. 22(b). It has been reported that the surface tension coefficient

($\partial\sigma/\partial T$) changes from negative to positive when the content of oxygen exceeds 50 ppm, and the direction of Marangoni flow changes from outward to inward [47, 71]. After reaching a maximum value (approximately 350 ppm), the surface tension coefficient ($\partial\sigma/\partial T$) reduces all the way to negative value [73]. The optical micrograph in Fig. 22 indicated that the change of the direction of Marangoni flow from inward (deeper and narrower melt pool) to outward (shallower and broader melt pool). Therefore, for normal 316L SS powder which contains hundreds ppm of oxygen, a positive surface tension coefficient and thus an inward Marangoni flow is anticipated.

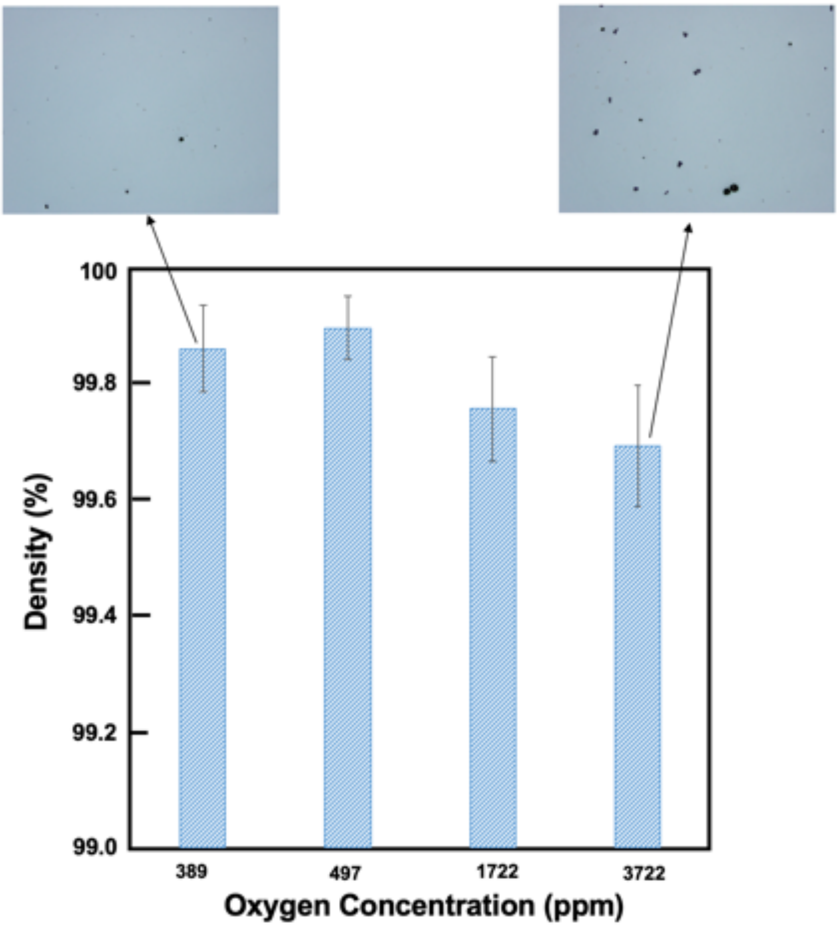

Fig 21 Densities of 316L SS AM Parts contains different amount of oxygen. The insets are optical micrograph.

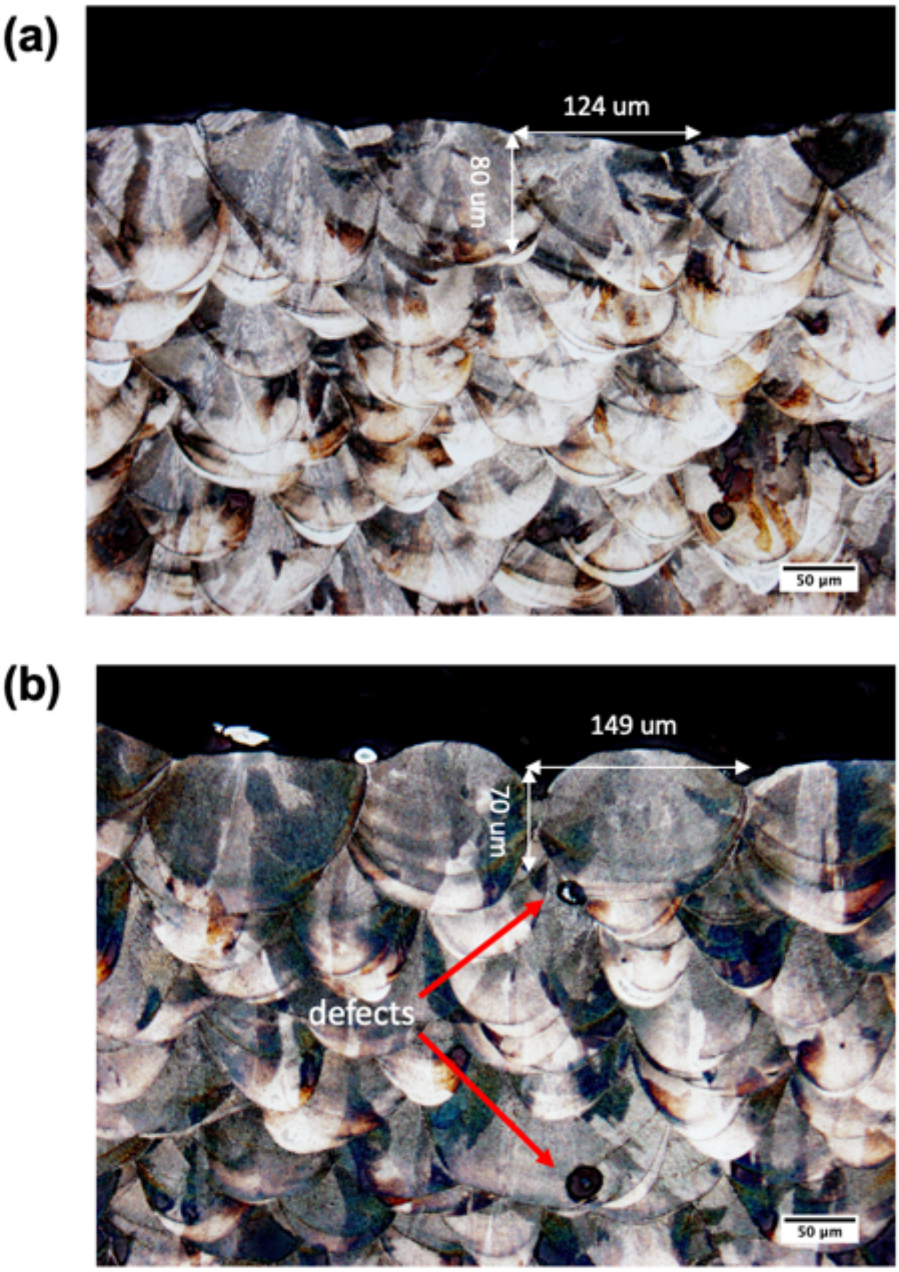

Fig 22 Optical micrograph of longitudinal cross section of etched AM 316L SS parts with different oxygen concentration: (a) 389 ppm; (b) 3722 ppm. Defects are indicated by red arrows in (b).

2.3.8 A physical picture of oxygen intrusion and its impact

Schematic shown in Fig. 23 illustrates the interactions between melt pool and oxygen intrusion from precursor powder and environmental oxygen. Under normal circumstances with fresh precursor powder and a well-purged L-PBF AM process chamber, the complex inclusions in the precursor powder completely dissolve and re-precipitate into smaller size oxide inclusions during L-PBF. The incorporation of heavily oxidized spatter particles and the oxidation of the melt pool surface were shown to be two possible mechanisms of oxygen intrusion from the L-PBF processing environment. Between them, the spattered particle incorporation was confirmed to be the dominant mechanism of environmental oxygen transfer into the AM parts. Spattered particles ejected from the melt pool were oxidized as they traversed through the chamber. Some particles deposited back on the solidified surface where they are incorporated into the part with successive laser processing. Partially sintered large particles could also introduce unmelt defects [61, 62, 67]. Furthermore, more defects and pores inside spatter particles as compared to fresh powder were found in this work, possibly due to coalescence of small ejecta during the mid-fly. High moisture contamination due to powder storage could also contribute to the formation of high-density oxide inclusions in AM parts. Nano-scale oxide inclusions in AM 316L SS parts reveal no additional strengthening effects but may affect stainless steel's toughness [14, 28, 29, 46]. However, it was observed in this study that moisture contamination caused notable hardness reduction. Therefore, preventing fresh powder from moisture contamination is vital for AM part quality. Elimination of oxygen getters such as Si and Mn in 316L SS has shown to be ineffective for reducing oxide inclusions in AM parts.

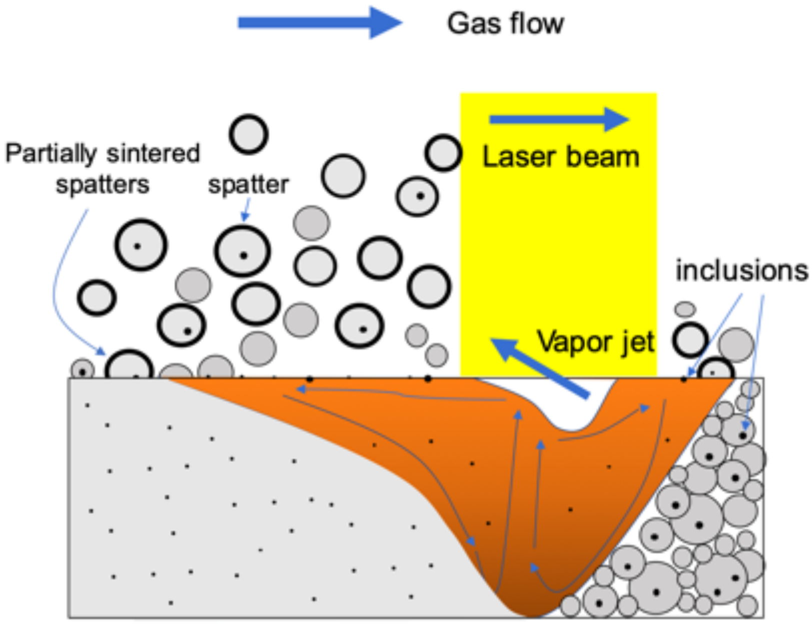

Fig 23 Schematic depicting interaction between environmental oxygen and melt pool.

2.4 Conclusion in this Chapter

In the present study, the formation mechanisms of nano oxides inclusions in L-PBF 316L SS was investigated by quantifying the contributions from the oxygen intrusion through precursor powder, in-situ oxidation during laser processing, and the moisture contamination during powder storage. The major findings are summarized as follows:

- Large oxide inclusions inside the fresh precursor powder, formed during inert gas atomization, was identified as the major source to the formation of nano-scale inclusions in AM 316L SS part through a dissolution/re-precipitation process. The contribution from the surface oxide on the fresh powder is negligible.
- A high oxygen level in the processing chamber of AM machine results in the elevated oxygen content in the final AM part. This process is dominated mainly by the incorporation of the oxidized spattered powder back into the melt pool.

- Exposing 316L SS powder to a high humidity environment is likely to degrade its flowability and increase the volume fraction of oxide inclusions. However, the humidity exposure within the range being tested in this study is not sufficient to affect the density and of the end parts. Only slight decrease of Charpy impact toughness was observed.
- Removing oxygen getters (Si and Mn) from 316L SS chemistry does not mitigate the oxygen contamination. Instead of Si/Mn rich oxides, Cr rich oxides can form which reduces the fracture resistance of 316L SS.
- The elevated oxygen level in the processing chamber (up to 1% oxygen), though increasing the oxygen content in the AM part, does not affect the hardness and tensile properties. AM part produced with the powder that is exposed to moisture can yield lower strength.
- High oxygen content (>1700 ppm) in AM 316L SS can alter the shape of melt pool and leads to lack of fusion defects.

Chapter 3

The Effect of Laser Scanning Direction on Spattering Behavior and its Impacts on 316L Stainless Steel Manufactured by Laser Powder Bed Fusion

3.1 Introduction

In the previous chapter, we have shown that spatter particles are the dominant contributor to oxygen intrusion from environmental oxygen. In this chapter, we expand on the studies of the effects of laser scanning direction on the spattering behavior. In the L-PBF process, the laser beam interacts with powder spread across the build plate. The heating of steel particles occurs in microseconds as the particles exposed to laser beams become liquid. The intensity of the laser beam follows Gaussian's profile, which means the maximum intensity decreases radially following Gaussian's distribution. Even with the energy loss due to reflection, the peak temperature of the melt pool can still exceed the boiling temperature of stainless steel. Nevertheless, only a portion of powders are in boiling state, since thermal conduction time through powders is much longer than heating time [74]. The proportion of particles in the boiling state will form a metallic vapor jet. High recoil pressure caused by evaporation exerts a downward force on the melt pool, resulting in liquid droplets ejection from melt pool. This ejected liquid droplet is known as spatter, which has also been widely known in welding and drilling applications. Recoil pressure, along with Marangoni convection was considered as the major contributor to the melt pool instability which leads to spattering, as reported by Qiu et al [75]. Khairllah et al. developed a three-dimensional high-fidelity powder-scale model. They successfully revealed melt pool behavior, including the formation of spattering induced by recoil pressure, defects and denudation zones [63]. Nevertheless, Ly et al. noted that the dominant mechanism leading to spatter formation is metal vapor-driven entrainment, instead of recoil pressure, as is widely understood [74]. By utilizing ultra-high-speed camera to monitor the melt pool dynamics, it was found that the velocity of vapor jet ejected from the evaporation zone of the melt pool can easily reach up to 700 m/s depending on the laser process parameter. The extremely high velocity vapor jet ejected vertically from the melt pool generates a low-pressure zone due to Bernoulli effect, which induces gas flow from surrounding gas to the laser beam. As a result, surrounding particles on the powder bed entrained by the gas flow towards the laser beam and a portion of them are heated, becoming hot spatter particles. Vapor jet entrainment spatter formation mechanism was later verified by Guo et al. using high resolution X-ray imaging technique [61]. Pore bursting in the melt pool may be another cause of droplet ejection [47].

Both high-speed photography [62, 66, 67, 74, 76, 77] and X-ray imaging [61, 78, 79] have been widely utilized for in-situ observation of spattering. We have noticed from the above-mentioned literatures and experiments that majority of spatter particles are ejected at the rear of melt pool, with the ejection direction opposites to the direction scanning laser beam. Although the dominant mechanism of spatter formation is under debate, both recoil pressure induced mechanism and vapor jet entrainment mechanism may explain that a majority of spatter particles are ejected behind the laser beam direction. The work done by Khairllah et al. has demonstrated how recoil pressure and Marangoni convection together shape the melt pool using high-fidelity model. Recoil pressure causes the build-up of liquid at the surface of melt pool, causing some molten liquid to elongate and separate into spherical droplets due to surface tension. The Marangoni convention induces turbulence into melt pool and thus causing instability which elevates the possibility of spatter ejection, as shown in Fig. 24(a). The distribution of the molten liquid in the melt pool is not equivalent relative to the laser beam position (depression zone), most at the rear of laser beam, due to the fact that conduction time through powders is much longer than heating time. In section 2.3.7, we demonstrated that AM 316L SS has a positive surface tension coefficient, which implies that the off-centered molten liquid moving away from the laser beam has a relatively low surface tension (lower temperature region). The lower surface tension reduces the energy required from recoil pressure for spatter ejection [80], and therefore, more spatter particles eject behind the laser beam. When the energy input from laser beam is in an appropriate range, the heating of powder follows a conduction mode which gives rise to a depression zone with an inclined front with respect to the laser beam, as illustrated in the Fig. 24(b). Conversely, a deep and narrow depression zone would form when the energy density exceeds the threshold value. The ejection direction of vapor jet is normal to the inclined front and thus the powder entrained by the vapor jet flies behind the moving laser beam. The scanning direction in Fig. 24(b) is from left to right, and it is clear that majority of flying particles were ejecting opposite to the laser beam in x-axis.

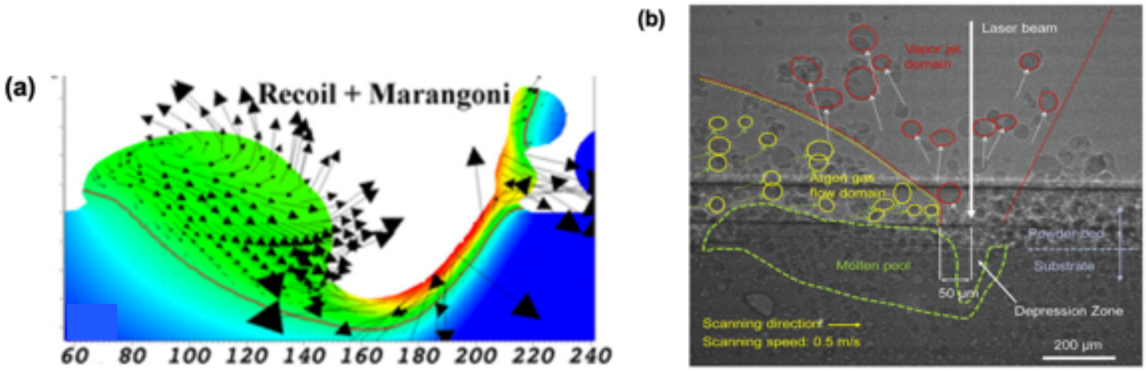

Fig 24 (a) 2D sliced melt track of 3D simulations demonstrating the effect of recoil pressure and Marangoni convection on shaping the melt pool [63]; (b) X-ray image of powder spattering [61].

Spatter particles are commonly considered as a by-product in the L-PBF process and L-PBF system are usually equipped with inert gas purging systems to carry away the spatter particles from powder bed into a filter. Extensive studies have been done to examine the detrimental effects of spatter particles on AM parts. (1) Large spatter particles generated during the L-PBF process that falls back on the printing part surface perturb the spreading and distribution of next layer powder [67]; (2) Large spatter particles that adhere to the printing part surface induce an incomplete melting region and leads to lack of fusion defects [61]; (3) Spatter particles were found to heavily oxidize compared to fresh powder and when they re-incorporate into the printing parts, oxygen was introduced into the parts [60, 81]; (4) Spatter particles could affect the surface roughness of

L-PBF parts [82]; (5) Flying spatter particles across the laser beam block the laser [83]. Due to the above effects, AM parts with more spatter particles generated during the fabrication process have shown degraded mechanical properties [82, 84]. Some efforts have been made to mitigate the formation of spatter particles, possible solutions include lower volumetric energy density and smaller layer thickness [61, 66, 76, 85]. Nevertheless, lower energy density could result in a lack of fusion defects in AM parts and smaller layer thickness increases material cost. According to the observation the majority of spatter particles were ejected opposite to the direction of scanning laser beam from the melt pool, it was inferred the gas flow in the L-PBF process chamber could play a significant role on the deposition of spatter particles on the surface of printed AM parts. In this work, since the gas flow direction in a L-PBF system was usually fixed, the effect of laser scanning direction with respect to gas flow was investigated for 316L SS.

3.2 Experiments and methods

316L SS precursor powder manufactured by nitrogen-gas atomization purchased from General Electric (GE) were used in this study. The AM parts were printed with Concept Laser Mlab Cusing SLM system. The printing parameter was set to 90 W laser powder, 0.6 m/s scan speed and 25 um layer thickness.

3.2.1 Instruments

Secondary electron (SE) imaging was conducted with a a JEOL 7000F field emission scanning electron microscope (SEM). The particles partially sintered on the surface of as-built AM parts were examined and analyzed by ImageJ.

Keyence VHX-6000 digital microscope was utilized to measure the area surface roughness of as-built AM 316L SS produced by different laser scan strategies. Keyence microscope equipped with high brightness LED light source has multi-lighting function and it can obtain lighting data from various angles. To measure the area surface roughness, the specimen surface with the size of 1 cm × 1 cm was imaged by stitching adjacent images in real-time. Images with high resolution (20000 × 20000 pixels) were acquired. Area roughness was obtained from roughness profile by calculating the arithmetical mean of the absolute values of height of peaks and valleys.

3.2.2 Experiment one

Two samples were printed separately at the same location on build plate, one was printed with laser scan in the direction of inert gas flow, another was printed with laser scan against inert gas flow. The AM parts situated in the powder bed after printing were photographed by camera and surface topography was measured by Keyence Microscope. This is aimed at investigating if laser scanning direction with respect to inert gas flow in the L-PBF process chamber could affect the amount of spatter particles deposit back on as-printed sample. The spatter particles have shown larger sizes compared to fresh powder and these particles stick on the sample surface and could increase the surface roughness, which can be characterized by Keyence Microscope.

3.2.3 Experiment two

The effects of spattering on adjacent as-printed parts at the same build plate were studied by design of experiments, as shown in Fig. 25. With gas flowing from left to right in the process chamber, spatter particles generated from the printing of sample 1 (S1) and 3 (S3) could incorporate into sample 2 (S1) and 4 (S4), and vis versa. Two printing orders were conducted: (1) 1234 (printed at 1% oxygen content environment); (2) 2431 (printed at 0% oxygen content environment). It was speculated that spatter particles fly against gas flow are easier to deposit back on as-printed surface. Since majority of spatter particles were shown to eject opposite to the laser scanning direction, S3 and S4 should have less spatter particles fall back on the on as-printed surface while S1 and S2 have more spatter particles on the surface. Moreover, for case (1), spatter particles generated from S1 and S3 that deposit on S2 and S2 would been directly re-melt by laser beam at the one-layer printing. However, since gas flow was from left to right, only a small quantity of particles from S2 and S4 was expected to incorporate into S1 and S3 for case (2). In Chapter 2, we demonstrated that spatter particles have a strong affinity with environmental oxygen, when they incorporate into as-printed part, oxygen transfer occurs from process chamber environment to AM parts and form oxide inclusions. Thus, the volume fraction of oxide inclusion in S1-4 measured was compared to analyze the effect of printing order on laser scanning direction on spatter particle incorporation. All samples were cut and polished parallel to building direction, using the same polishing steps as described in Section 2.2

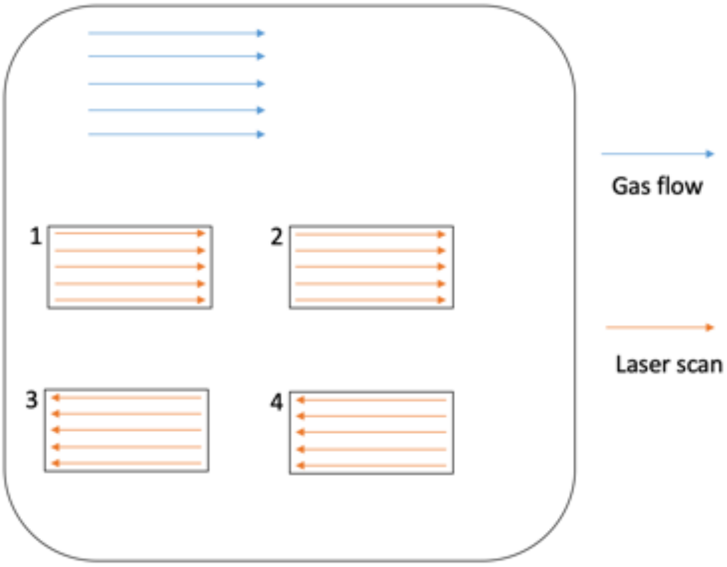

Fig 25 Experimental set up for investigating the effect of spattering on adjacent as-printing parts.

3.3.4 Experiment three

Flat tensile bar (6 mm × 2 mm × 68 mm) was used to compare the effect of laser scanning direction on mechanical properties of AM 316L SS. Experiment 1 and 2 compared AM parts printed by laser scans against the direction of gas flow and laser scans in the direction of gas flow, the results were characterized by surface roughness and oxygen incorporation. Due to the fact that our Concept Laser system does not enable the advanced parameter settings, we cannot print AM parts with single laser scanning direction, it will always rotate 180 degree at subsequent layer. The specimens at Experiment 1 and 2 were printed "manually" by repeating the same layer printing. Since only around 50 layers thick parts (1.25 mm) were sufficient for roughness and oxides volume fraction analysis, it is not feasible to print tensile bar this way which contains thousands of successive layers. Alternatively, two groups of thickened flat tensile bars (6 mm × 12 mm × 68 mm) were printed horizontally with laser scanning parallel and perpendicular to gas flow, and laser beam rotates 180 degree at subsequent layer. The thickened flat tensile bars were then sectioned to several piece of bars with desired thickness (6 mm × 2 mm × 68 mm) by electrical discharge machining (EDM). The laser track length was the same for two bars, as indicated in Fig. 25. Two cubes were printed with two different laser scanning directions and ultrasonic cleaned to remove loose powder/spatter particles, the surface was checked by SEM. The number and size of particles which partially sintered on the sample were analyzed by ImageJ software. The oxygen content of two samples were measured by ICP.

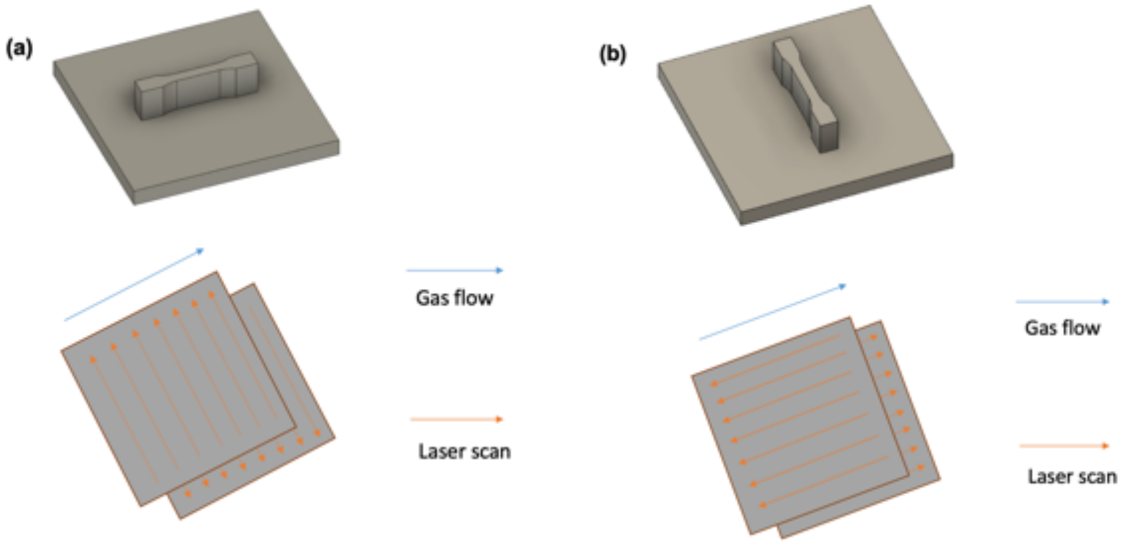

Fig 26 Schematic diagram of horizontally built tensile bars and corresponding laser scan strategy applied in the process. (a) laser scans perpendicular to gas flow; (b)laser scans parallel to gas flow.

3.3 Results and Discussion

3.3.1 The effects of laser scanning direction (same and opposite) relative to the direction of inert gas flow on surface roughness

Fig. 27 displays the topography of two AM 316L SS parts printed with laser scanning against gas flow and laser scanning in the direction of gas flow. When laser scans opposite to the direction of gas flow, majority of spatter particles ejected from the melt pool are flying in the direction of gas flow and thus they are easier to be accelerated and carried away by the gas flow from the powder bed, as shown in Fig. 27(a). The left half of the cube surface contains visibly less spatter particles (black spots) in comparison to the right half. This has been demonstrated by the Fig. 27(b) obtained by Keyence microscope, the areal surface roughness at the right half of the cube is higher than the left half with the overall areal surface roughness of 17.79 um. On the contrary, the cube printed with laser scanning in the direction of gas flow exhibited uniform high surface roughness from Fig. 27(d), its areal surface roughness is 18.97 um. Spatter particles ejected in the direction against the gas flow were deaccelerated and significant amount of them deposited back on the as-printed surface, which leads to higher surface rough ness due to its large average size.

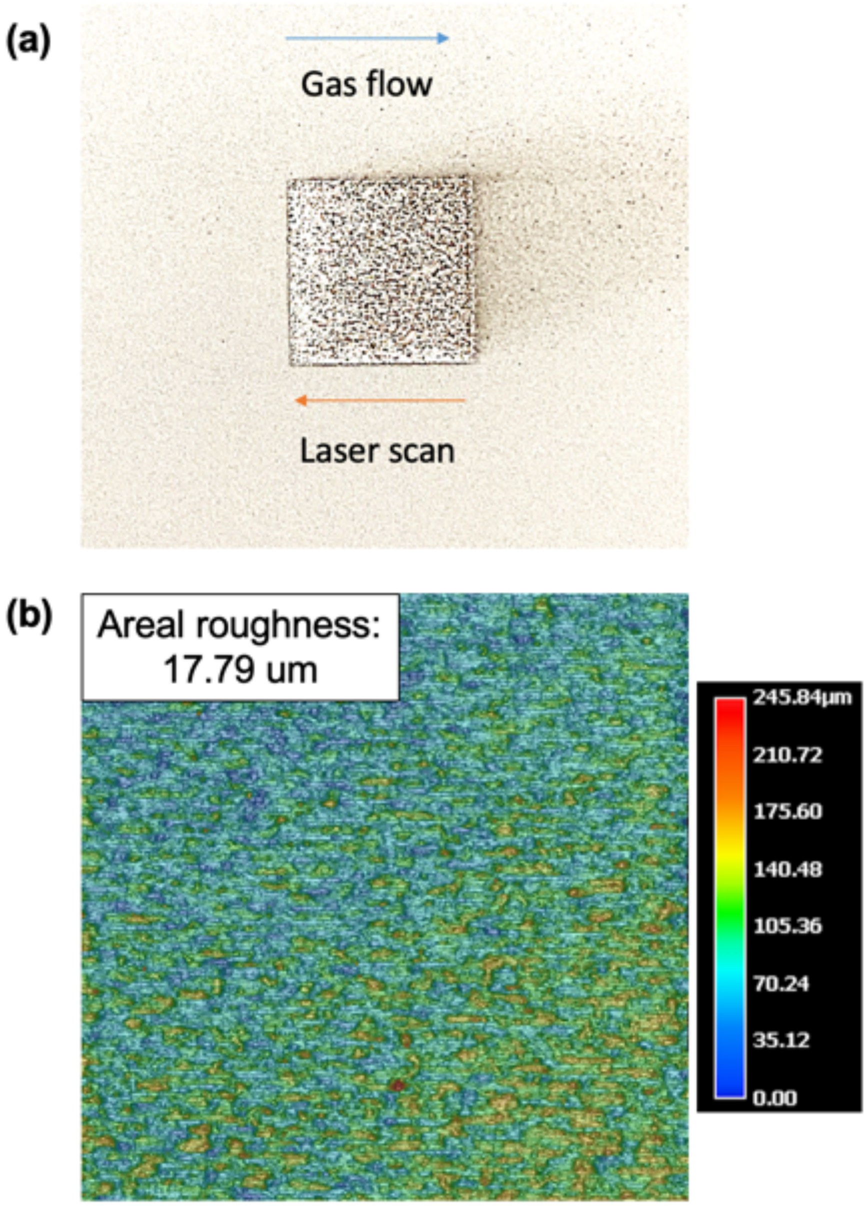
(a)
Gas flow
Laser scan
(b)
Areal roughness:
17.79 um
245.84µm
210.72
175.60
140.48
105.36
70.24
35.12
0.00

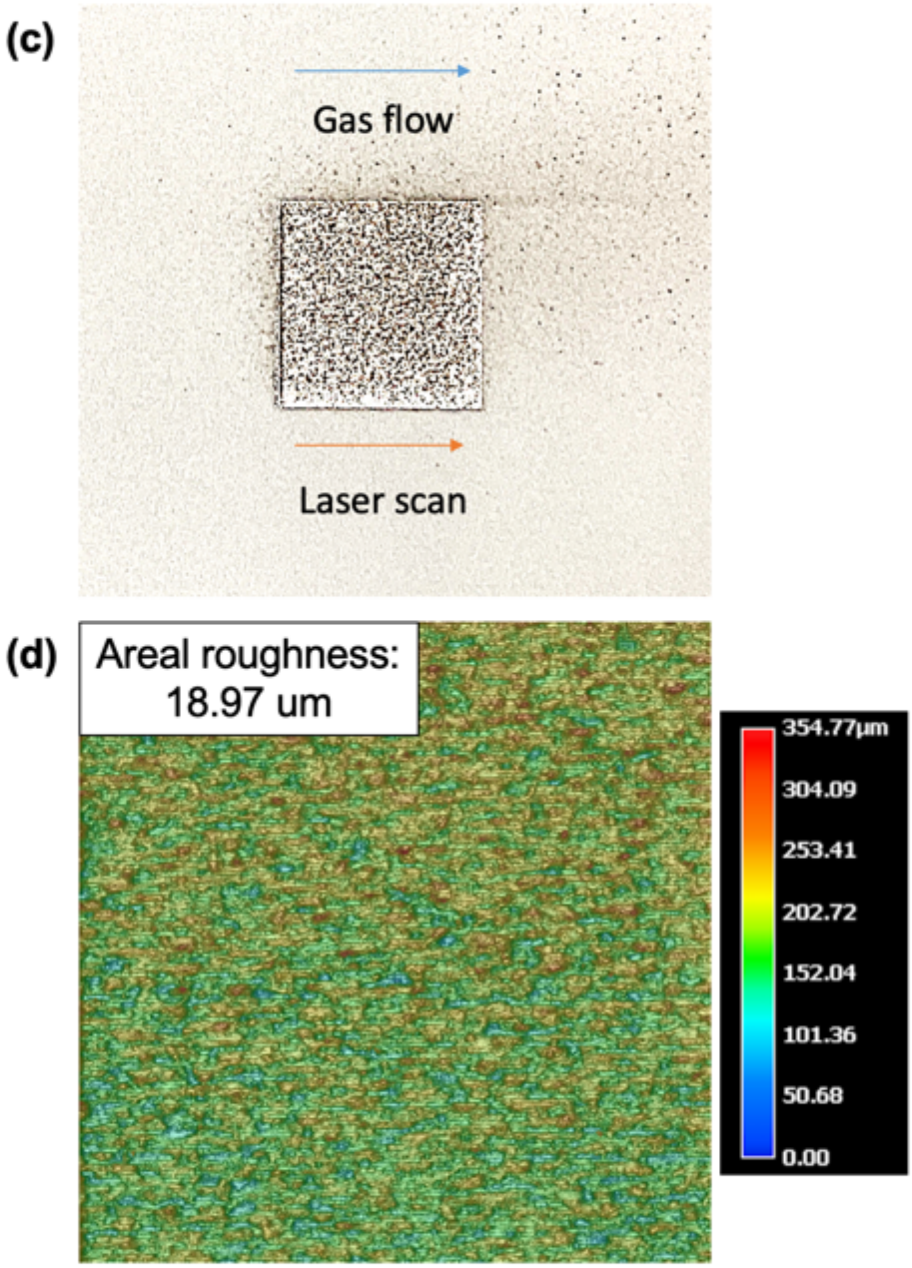

Fig 27 (a) Spatter particles distributed on the as-printing part surface with laser scanning against gas flow; (b) Topography of part in (a); (c) Re-deposit spatter distribution (dark spots) on the printing part surface with laser scanning in the direction of gas flow; (d) Topography of part in (c). Black spots in (a) and (c) are considered as spatter particles.

3.3.2 Spatter introduced oxygen contamination from adjacent as-printing part

The spatter particles generated from one as-printed AM part could be introduced into another adjacent as-printed AM part. The experimental design was shown in Fig. 25. S1-4 were printed with two different orders at 0% and 1% oxygen content environment, 1% oxygen content environment could exaggerate the oxygen contamination. Spatter particles have shown to be able to pick up large amount of environmental oxygen in the L-PBF processing chamber during mid-fly, they could be a source of oxygen contamination for adjacent as-printed part. The volume fraction of oxide inclusions is shown in Fig. 28(a) with printing order of 1234. Obviously, with inert gas flow from left to right, spatter particles generated on the left part of build plate could contaminate parts built on the right part of build plate. The same conclusion could be drawn from Fig. 28(b). Comparing volume fraction of oxide inclusion in AM 316L SS part printed with normal island scanning strategy (0% and 1%), laser scans in the direction of gas flow could pick up more environmental oxygen into AM parts. The dash line represents the volume fraction of oxide inclusion printed with normal island scanning strategy at 1% and 0% oxygen content environment.

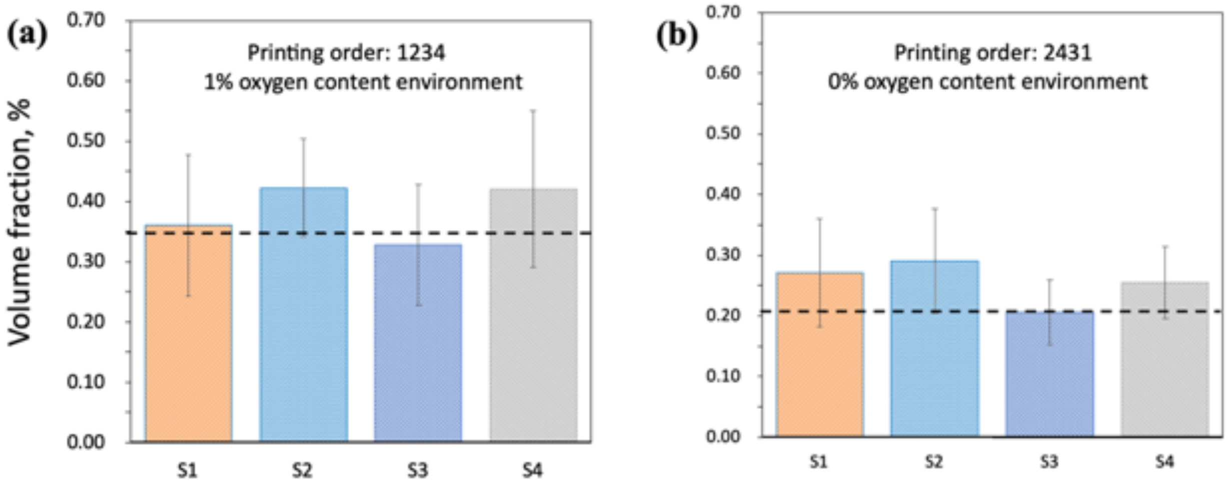

Fig 28 Volume fraction of oxide inclusions in AM 316L SS parts with printing order of 1234 at 1% oxygen content environment (a); and printing order of 2431 at 0% oxygen content environment (b). The dash line represents the volume fraction of oxide inclusion printed with normal island scanning strategy at 1% and 0% oxygen content environment.

3.3.3 The effects of laser scanning direction (parallel and perpendicular) relative to the direction of inert gas flow on tensile properties

Ultrasonic cleaning was applied to the as-printed AM 316L SS samples to remove loose powder/spatter particles on the surface, the sample surface was then examined by SEM under secondary electron (SE) mode. The SE images of two AM parts surface were given in Fig. 29, more and smaller partially sintered particles were observed on the part printed by laser scanning parallel to gas flow. Five SE images per sample were processed by ImageJ to analyze the size and number of particles on the sample, as displayed in Fig. 30. The particles on perpendicular to gas flow printed AM 316L SS has an average size and average number density of 33.6 um and 24/mm^2, respectively, in comparison to 27.4 um and 21/mm^2 for parallel to gas flow printed AM 316L SS. Size distribution histogram of surface particles in Fig. 30(b) indicated that particle with size between 20 um to 30 um deposit the most easily on the as-printed surface. As discussed in Chapter 2 and earlier in this chapter, spatter particles transfer environmental oxygen from L-PBF process chamber to as-printed AM part, and they also introduce defects into AM parts. The density and oxygen content were compared to evaluate the spatter introduced oxygen contamination and spatter introduced defects, as shown in Fig. 31. Both samples were printed under 0% oxygen content environment, it has shown in Fig. 12 that the spatter particles generated at 0% oxygen content environment have three times higher oxygen content than precursor powder. More and larger spatter particles re-incorporated into as-printed 316L SS undoubtedly leads to higher oxygen content, as shown in Fig. 31. Spatter particles could lead to defect generation by perturbing the spreading of powder layer and incomplete melting and fresh powder. Moreover, we also found that spatter particles itself contain large defects and could be transferred into as-printed parts, as shown in Fig. 32. Nevertheless, no obvious spatter introduced defects were observed in this work. The underlying reason could be the fewer considerable differences between the size and amount of spatter particles on the as-built part surface printed with laser scans perpendicular and parallel to the gas flow. In addition, the volumes are small in this work and thus there is less possibility of spatter to introduce defects was considered as another cause. Additionally, no obvious differences on tensile properties between as-built samples were observed, as shown in Fig. 33.

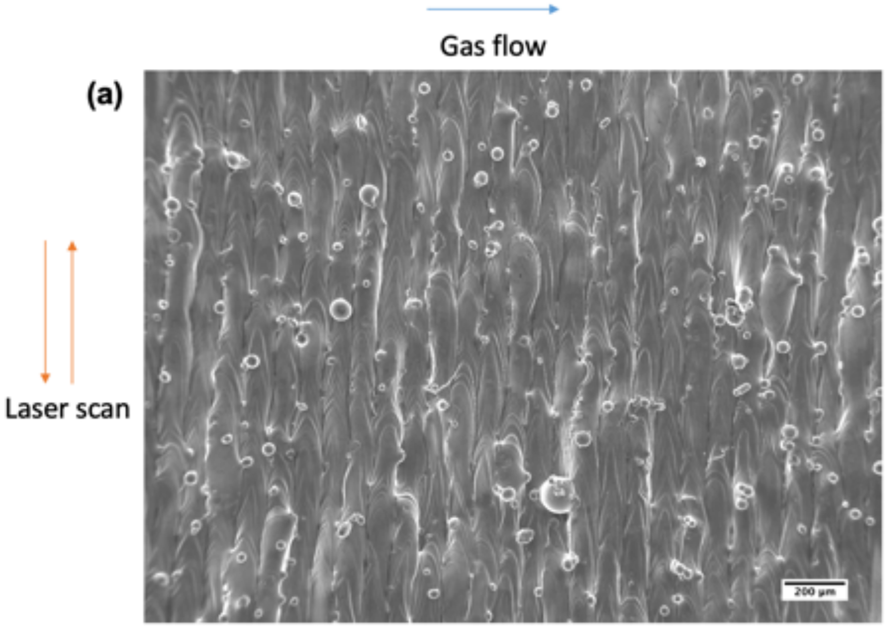

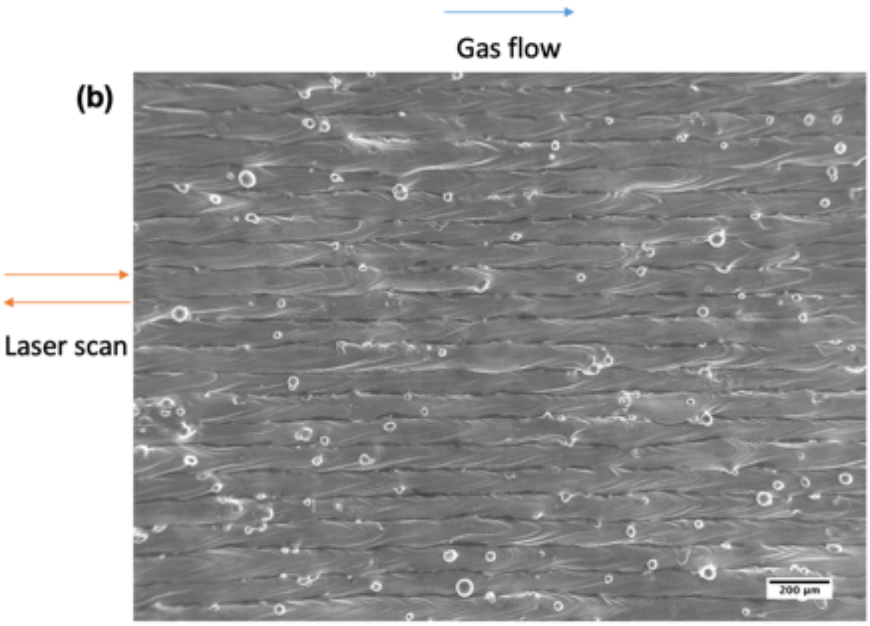

Fig 29 SEM Secondary electron (SE) image of AM 316L SS as-built surface showing partially sintered spatter particles: (a) laser scans perpendicular to gas flow; (b) laser scans parallel to gas flow.

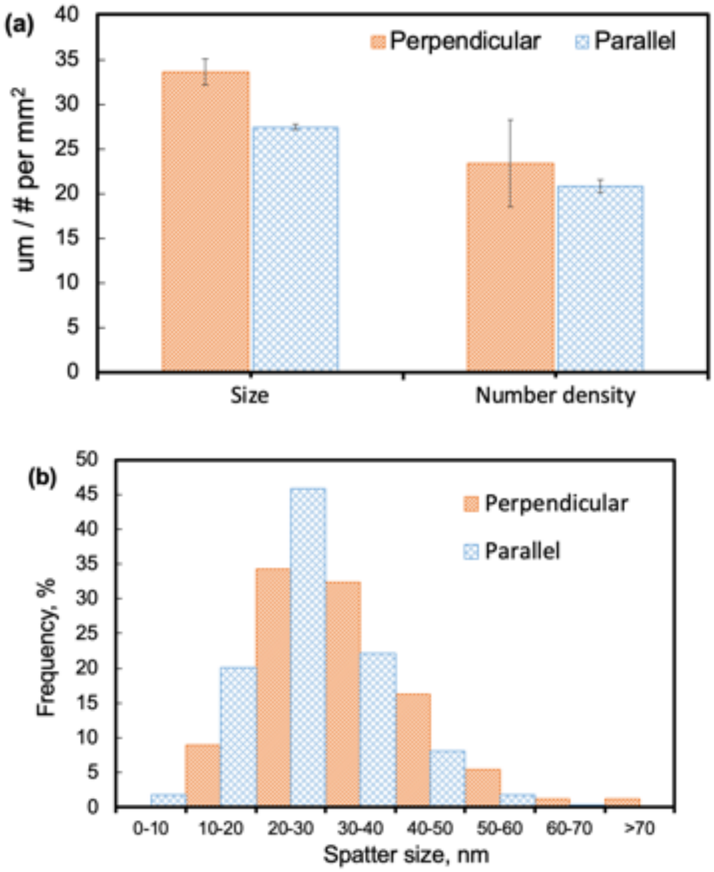

Fig 30 Comparison of (a) average size, number density, and (b) size distribution of partially sinter particles on AM 316L SS printed with laser scanning perpendicular and parallel to inert gas flow.

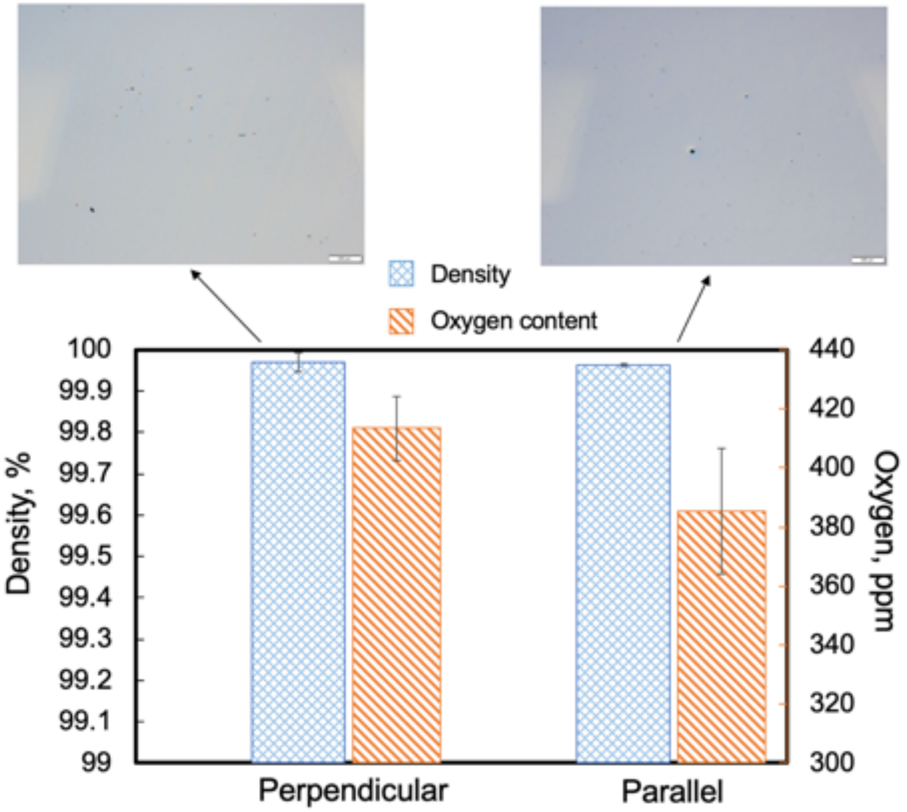

Fig 31 Comparison of density and oxygen content on AM 316L SS printed with laser scanning perpendicular and parallel to inert gas flow.

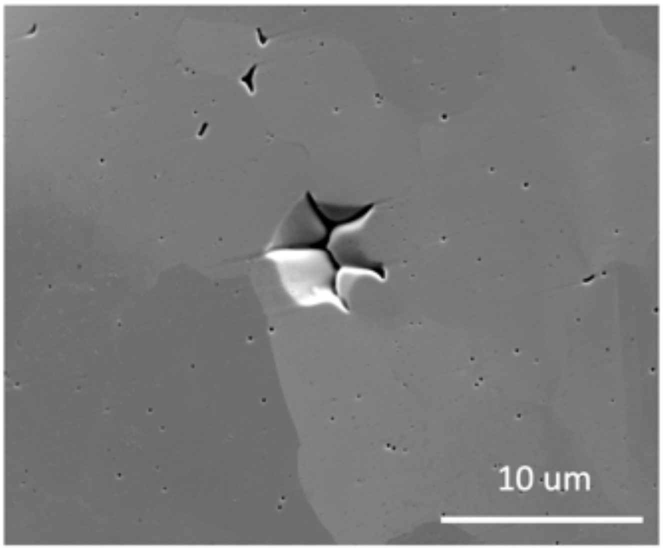

Fig 32 SEM image of the cross section of a spatter particle.

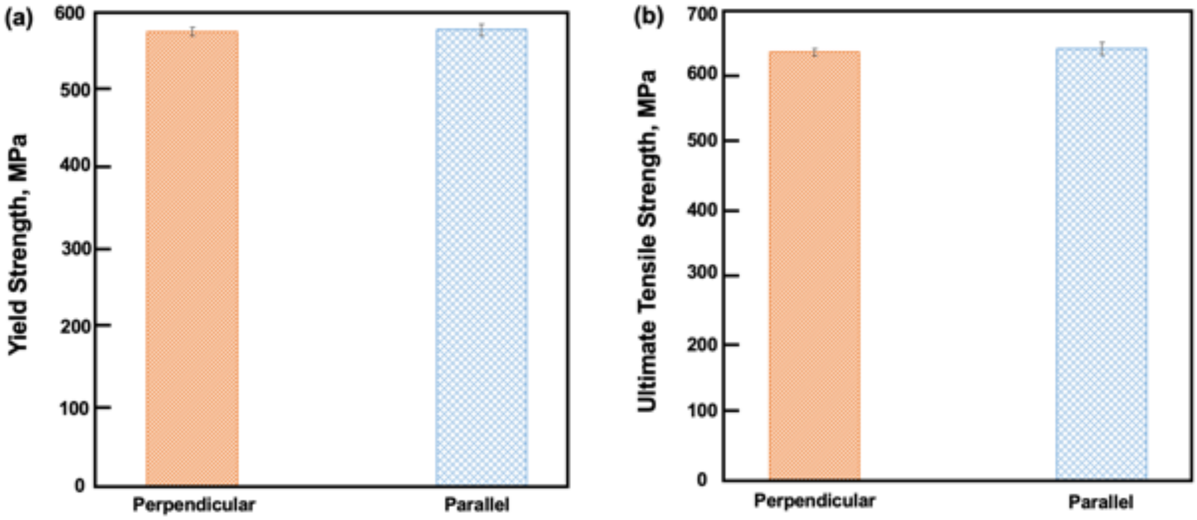

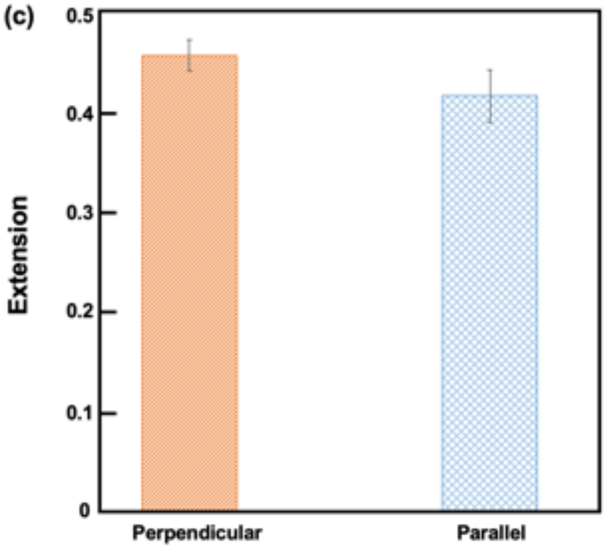

Fig 33 Comparisons of (a) yield strength, (b) ultimate tensile strength, and (c) extension, between as-built AM 316L SS printed with laser scanning perpendicular and parallel to inert gas flow.

3.4 Conclusion in this chapter

The transportation of spatter particles that ejected from melt pool to the as-printed sample surface during L-PBF process was found to be significantly affected by the scanning direction of laser beam relative to the gas flow. Laser scans against the direction of gas flow leads to less spatter particles deposit on as-printed sample than laser scans in the direction of gas flow. As a result, AM sample printed with laser scanning in the direction of gas flow has higher surface roughness due to the fact that spatter particles have larger average size than fresh powder. Adjacent printing parts on the build plate were also another source of spatter particle. Spatter particles can act as L-PBF process environmental oxygen getters which subsequently transfer environmental oxygen to final AM part and form oxide inclusion. The AM 316L SS fabricated with laser scanning perpendicular and parallel to the gas flow were compared. More and larger spatter particles were observed on as-built part surface which laser scans perpendicular to gas flow than that of laser scans parallel to gas flow. These spatter particles also introduce L-PBF process environmental oxygen into the AM part. However, although extensive studies have illustrated the spatter introduced defects, the density and tensile properties were not affected in this study and is likely due to small build volume. One of the goals of metal additive manufacturing industry is larger build volume, which potentially increases the possibility of spatter introduce defects from as-printed part itself and nearby parts. According to the present work, lase scans parallel to the gas flow of L-PBF process, more specifically, against the gas flow reduce the risk of spatter particle re-incorporation in as-printed parts. From the L-PBF system design aspect, a powder bed with rectangle shape and gas flow along the width (short side) axis could help to lessen the amount of spatter particle contamination from upwind as-printed parts to downwind as-printed parts.

Chapter 4

The Evolution of Nanoscale Oxides during Heat Treatment in 316L Stainless Steel Manufactured by Laser Powder Bed Fusion

4.1 Introduction

316L stainless steel (SS) is one of the most widely used and developed materials for metal additive manufacturing [1]. Additively manufactured 316L SS has shown both superior strength and ductility as compared to its wrought or cast counterparts [6, 7, 12]. The strength-ductility trade-off has been a longstanding challenge for metals, extensive efforts have been made to strengthen metals without sacrificing ductility. Many approaches have been reported, such as grain size gradient structure [86], introducing coherent twin boundaries [87, 88], and controlling size and distribution of secondary phases [89, 90]. Nevertheless, these methods require intensive mechanical processing and surface treatment and hence not feasible for producing components with complex geometry. LPBF provided an excellent solution for fabricating complex geometry components with a combination of high strength and ductility.

Cellular network structure and nanoscale oxide inclusions are the two most unique microstructure features for AM 316L SS comparing to those manufactured by conventional manufacturing methods [7, 12, 91]. Extensive studies have been made on their contributions to the advanced mechanical properties of AM parts. Both dislocation network and nanoscale oxide inclusions in 316L SS manufactured by LPBF has shown the ability to impede the dislocation movements, meanwhile, the impediment can be overcome at high applied stress to achieve a continuous flow, which enables the improvement of both strength and ductility [91]. After heat treatment above a particular temperature, however, the dislocation network would disappear due to the recovering process and lead to degraded strength [92]. On the other hand, nanoscale oxide inclusions conserve high interfacial energy between second phase particles and matrix, which results in particle coarsening by Ostwald ripening at elevated temperature driven by the reduction of the total surface free energy [93, 94]. In the meantime, during heat treatment, grain boundary migration initiated by the nucleation of new grain and recrystallization could complicate the coarsening of second phase particles and the distribution of particles after heat treatment [95-97].

Second phase coarsening, also known as Ostwald ripening, has been extensively studied. This phenomenon was first found in the water-oil emulsion system and nowadays it has been commonly observed in the metallic system and other non-metallic systems. Ostwald ripening refers to the process that large particles grow at the expense of small particles, and the driving force is the reduction of surface energy. Mathematical description of the ripening process was made by Lifshitz, Slyozov, and Wagner (LSW theory), it predicts the kinetic and the particle size distribution function under the assumption that no particle-particle interactions. Nevertheless, experimentally determined particle size distribution is inconsistent with that calculated by LSW theory. Many attempts have been made to modify LSW theory to accommodate its deficiencies, however, none is fully satisfied, and more experiments and theoretical calculations are required [94]. The present work is focusing on the characteristics of oxides evolution during heat treatment and its theoretical explanation with experimental evidence, the mathematical investigation is not addressed herein.

A dispersion of the second phase is formed by nucleation and growth in a supersaturated solution. Second phase particles present in matrix vary in size contain high surface energy. At elevated temperature, the system starts to evolve to obtain a lower energy state, and theoretically, the process ends until the second phase condenses to a single particle. The reduction of system total energy is achieved by particle coarsening which results in the decrease of interfacial energy. The coarsening of particles originates from the concentration gradient at the particle-matrix interface. The equilibrium concentration at larger particles surface is lower than that of the smaller ones, as described by Gibbs-Thomson relation:

$$C_r = C_e exp\left[\frac{2\gamma\Omega}{R_B T} \cdot \frac{1}{r}\right] \approx C_e\left[1 + \frac{2\gamma\Omega}{R_B T} \cdot \frac{1}{r}\right] \qquad (2)$$

Where C_e is the solute concentration at a planar interface of an infinite particle with matrix, C_r is the solute concentration at the surface of a particle with radius r, γ is the interfacial energy of particle-matrix interface, Ω is mean atomic volume of the particle, R_B is a constant, T is the absolute temperature. Small particles have higher solute concentration than the matrix, and this induces a net diffusion flux from small particles to the matrix, while atoms flow from the matrix to large particles. From the physical aspect, atoms at small spherical particle surfaces have fewer neighbors to bond than large particles, thus the atoms at small particles surface rip off easily. As a result, small particles shrink, and large ones grow. The average size of particle increases while the number of particles decreases along with the total surface free energy of the system.

In Chapter 2, it has been demonstrated that oxide inclusions in AM 316L SS in a well-controlled environment are mainly originated from inclusions in precursor powder. Complex inclusions in precursor powder completely dissolve and precipitate out into smaller sizes. The nanoscale oxides do not meet the requirement of minimum energy performance. Thus, smaller oxide inclusions will dissolve into the matrix while the larger one will grow at elevated temperatures. So far, to the best of our knowledge, there is only limited reported research about the evolution, including size, distribution, morphology, and chemistry, of nanoscale oxide inclusions present in AM 316L SS during heat treatment. Additionally, we presented our experimental observations along with discussions of nanoscale oxide inclusion in AM 316L SS coarsening before and during the recrystallization process and demonstrate that the migration of grain boundary facilitated the particle coarsening. The coarsening of particles during grain boundary migration has been experimentally observed previously [96, 98, 99]. Some studies proposed that the migrating grain boundaries dissolve second phase particles owing to higher solubility at grain boundary than the matrix, and subsequently re-precipitate out behind with larger size due to enhanced diffusivity at boundaries [100-103]. While other studies note that particles were dragged by the moving grain boundaries, particles undergo an improved coarsening at boundaries until the grain boundaries break away due to the decrease of Zenner pining effect [97, 98, 104-108]. Both theories were studied via experiments and numerical simulations. The movement of inclusions caused by grain boundary migration leads to the inhomogeneous distribution of inclusions. Considering the effective volume of grain boundaries as compared to grains, a significant volume fraction of inclusion and inclusions with higher average size presented at grain boundaries while smaller inclusions exist in the grain. This is usually undesirable, inclusions at grain boundaries may weaken the boundaries and embrittle the material, moreover, the loss of finely dispersed inclusions in the grain could also weaken the material. The aim of this work including (1) investigating the kinetic of oxide inclusion evolution in AM 316L SS during heat treatment; and (2) exploring the role of grain boundary migration on oxides evolution, including size and distribution in AM 316L SS.

4.2 Materials and Methods

4.2.1 Powder materials and L-PBF system

316L SS precursor powder manufactured by nitrogen-gas atomization purchased from Carpenter Powder Products was used in this study. The powders were sieved to -325 mesh/+15 μm (15-44 μm) for good flowability and AM parts were printed with an EOSINT M270 system (at Quad City Manufacturing Laboratory, Rock Island, IL, USA). The EOS system used 195 W of laser power, 1.2 m/s scan speed and 20 μm layer thickness. The chemistry of power and AM part was displayed in Table.1 at Chapter 2.

4.2.2 Sample preparation

Specimens cut from one AM 316L SS part were heat-treated at a serious of temperatures (650 ℃, 955 ℃, 1065 ℃ and 1150 ℃), followed by water quenching. AM parts for inclusion analysis including as-built and heat-treated specimens were sectioned parallel to the build-up direction. Surfaces were prepared by mechanically grinding to a 220 grit using SiC grinding papers and then followed by polishing with 9um, 3um diamond suspension using Struers TegraPol-15 Auto-polisher with Tegraforce-1. Surfaces were finalized with vibratory polishing using colloidal silica using Buehler Vibromet 2 vibratory polisher. After vibratory polishing, the surface of specimens was first cleaned with Alconox solution by wiping using microfiber cleaning cloth to remove remaining suspension particles. Then the specimens were further cleaned with ultrasonic cleaner for 30 minutes. This preparation method produced a clean, strain-free and scratch-free surface on the relatively soft austenitic stainless steel samples.

4.2.3 Scanning electron microscope (SEM) and transmission electron microscope (TEM)

Backscattered electron (BSE) imaging was conducted with a Hitachi SU70 (at Quad City Manufacturing Laboratory, Rock Island, IL, USA) or a JEOL 7000F field emission scanning electron microscope (FE-SEM). BSE images were obtained with an yttrium-aluminum-garnet (YAG) scintillator detector, which offered high sensitivity and high resolution with a low beam current. Low accelerating voltages, ranged from 7 to 10 kV, were also applied in BSE imaging to reduce the beam-sample interaction volume and increase spatial resolution. Specimens for transmission electron microscopy (TEM) or scanning TEM (STEM) were prepared using standard focus ion beam technique in an FEI Helios Nanolab in Michigan Center for Materials Characterization (MC2) at the University of Michigan. The FIB lift-outs were first thinned to around ~300nm by 30KeV beam energy and then to about ~100 nm by 5KeV to reduce the FIB damages. Energy-dispersive X-ray spectroscopy (EDS) mappings were performed on a Thermo Scientific Talos F200X microscope operating at 200kV. EDS-based hypermaps were taken with 512x512 pixels using a probe full-width half max of ~1.5 nm and a beam current around 3 nA. After collecting the hypermaps, line scanning data can be generated between any two points within the 2D map using Velox software.

4.2.4 Statistical analysis of oxide inclusion

Volume fraction and size of oxide inclusions were acquired by using ImageJ software. Fifteen BSE images from the precursor powder or AM build samples were averaged following ASTM E1245 [37]. Oxide inclusions situated at grain boundaries (intergranular oxides) and inside the grain (intragranular oxides) of recrystallized region were separately analyzed by ImageJ, as exampled by Fig. 34. BSE images contain a complete grain were used, oxides at grain boundary and inside the grain were separately measured.

Fig 34 Example of analyzing volume fraction percent and number percent of intergranular and intragranular oxides using ImageJ.

The volume fraction percent and number percent of intergranular oxides and intragranular oxides were determined by the following equations:

$$\mathit{volume\ fraction\ percent\ of\ intergranular\ or\ intragranular\ oxides} = \frac{\mathit{volume\ fraction\ of\ intergranular\ or\ intragranular\ oxides}}{\mathit{volume\ fraction\ of\ all\ oxides\ for\ a\ grain}}$$

(3)

$$number\ percent\ of\ intergranular\ or\ intragranular\ oxide = \frac{number\ of\ intergranular\ or\ intragranular\ oxides}{number\ of\ all\ oxides\ for\ a\ grain}$$

(4)

4.3 Results

4.3.1 Oxide inclusions in stress relieved (650 ℃) and fully recrystallized (1150 ℃) AM 316L stainless steel

The BSE images of stress relieved AM 316L SS in Fig. 35 (a) and (c) displayed the microstructure of the horizontal section and perpendicular section to the build-up direction. Fig. 35 (c) and (d) showed the corresponding magnified BSE images, the spherical particles in the material have been confirmed as oxide inclusions from the literature [5, 8, 14]. The elemental segregation can be observed under BSE mode, and the network was brighter than the interior, this is consistent with elemental segregation (Cr and Mo enrich at the cellular wall) of cellular structure in AM 316L SS parts as well as the size of the cellular structure (< 1 um), as displayed in Fig. 2 [12, 91]. All of the intragranular oxide inclusions were shown to distribute along the cellular wall. The size of oxide inclusion was analyzed by ImageJ using BSE images due to its optimum contrast between the matrix and particles. The histogram of the size distribution of oxide inclusions in stress relieved AM 316L SS is shown in Fig. 35(e), the average size of oxide inclusion is approximately 50 nm.

Fig. 36(a) displayed the backscattered electron (BSE) image of fully recrystallized AM 316L SS (HIP + SA), which exhibits coarse and equiaxed grains with an average size of 70 um. The high magnification secondary electron (SE) image in Fig. 36(b) revealed large oval-shaped inclusions with an average size of 392 nm along the grain boundary and inside the grain. Moreover, it indicated that relatively larger size inclusions at the boundary and a smaller one inside the grain. The histogram of the size distribution of oxide inclusions in fully recrystallized AM 316L SS is shown in Fig. 37, the similar Gaussian distribution was presented as the size distribution of oxide inclusions in stress relieved AM 316L SS.

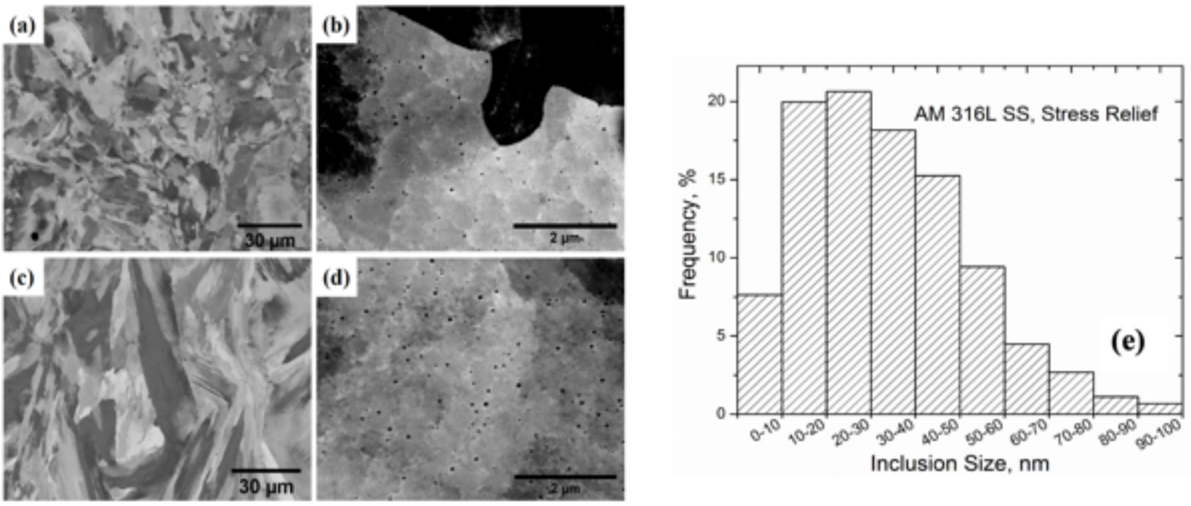

Fig 35 Back scattered electron images of AM 316L stainless steel after 650 ºC stress relief: (a) and (b) show the cross-section perpendicular to the build direction (low vs. high magnification); (c) and (d) show the cross-section parallel to the build direction (low vs. high magnification); (e) Nano oxide particle size distribution in stress relieved AM 316L stainless steel

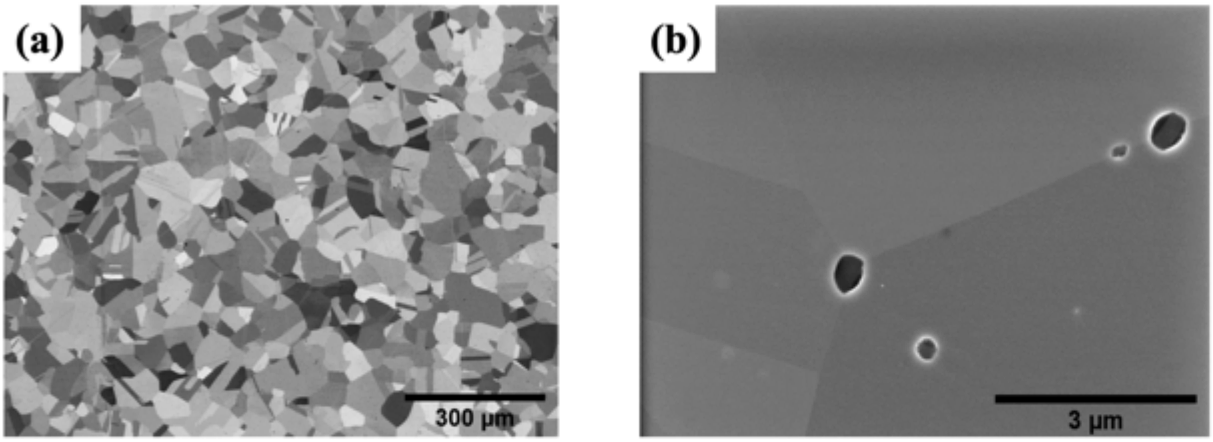

Fig 36 AM 316L stainless steel after hot isostatic pressing and solution annealing: (a) low magnification, backscattered electron image of fully recrystallized microstructure; (b) high magnification, secondary electron image revealing large inclusions inside the grains and along the grain boundaries

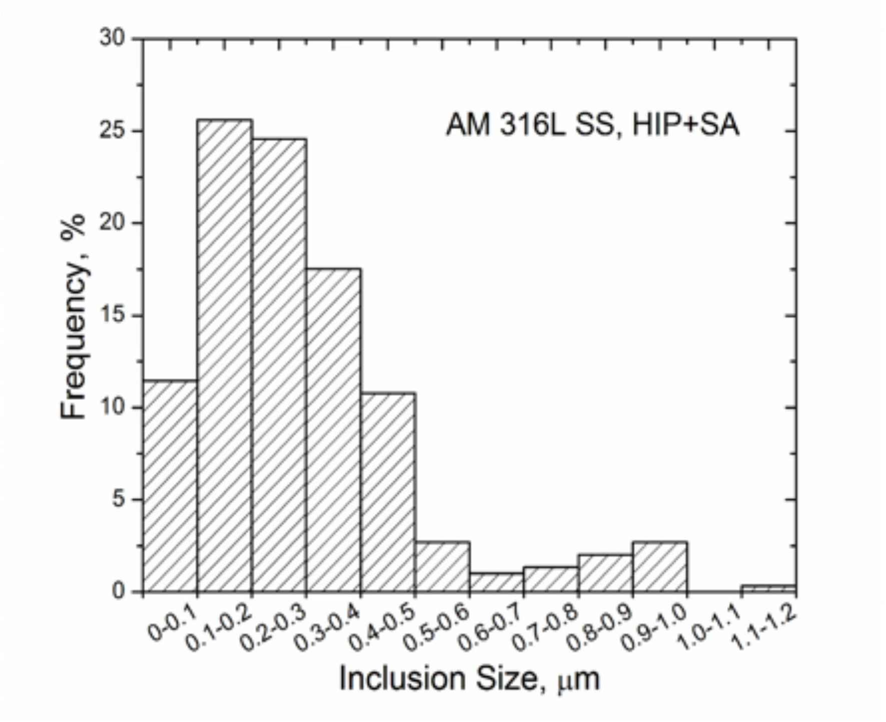

Fig 37 Inclusion size distribution in fully recrystallized AM 316L stainless steel

4.3.2 The size evolution of oxide inclusions in AM 316L stainless steel parts with temperature

The average size of oxides in AM 316L SS was compared among as-built parts and those heat-treated for 2 hours at a series of temperatures (650 ℃, 955 ℃, 1065 ℃ and 1150 ℃). The BSE images of AM parts after heat treatments were presented in Fig. 38, inclusions coarsened contiguously with increasing temperature. Fig. 39 displayed the average size, and volume fraction of inclusions in as-built (represented by 25 ℃ in the figure) and heat-treated AM parts, fifteen BSE images of each sample were utilized to accomplish the analysis. The magnification of BSE images was kept the same for low temperature annealed samples (3500 X). In contrast, for specimens treated at high temperature, lower magnification was chosen to process enough number of inclusions (15000 X and 13000 X).

The volume fraction of inclusion remained almost constant with heat treatment temperatures, indicates that there was no oxygen intrusion during heat treatment. The average size of inclusion raised significantly after 650 ℃ heat treatment, which has the same meaning as the falling number of inclusions. Therefore, the inclusions coarsened through Ostwald ripening, which occurs by the growth of large particles at the expense of small ones [109-111]. No obvious coarsening was observed after stress relieving (650 ℃) for 2 hours.

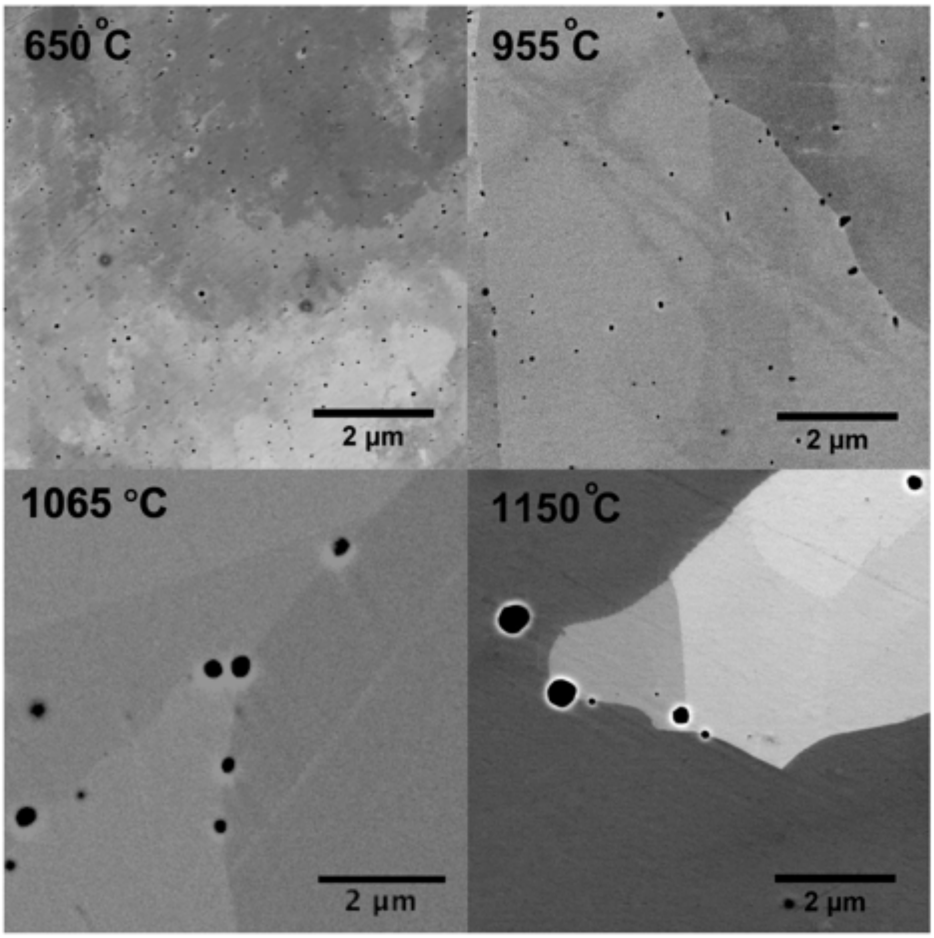

Fig 38 Effect of heat treatment temperature on oxide inclusion coarsening (2 hours' isothermal heat treatment)

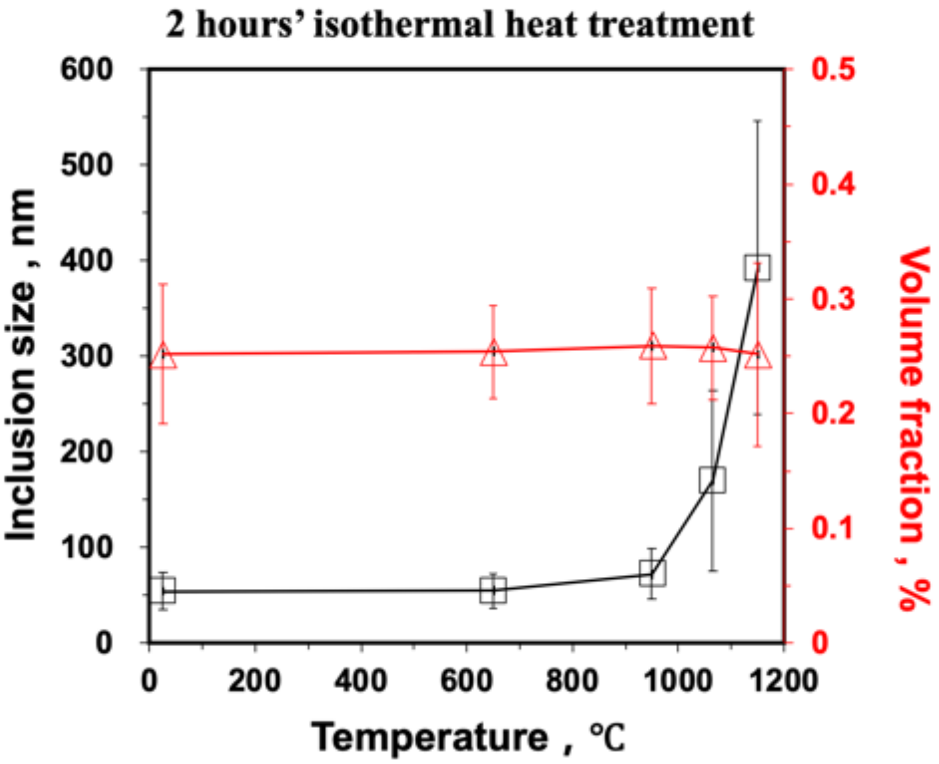

Fig 39 The average size and volume fraction of inclusion in as-built and heat-treated AM 316L SS, 25 ℃ represent as-built condition.

4.3.3 The role of grain boundary migration on oxide coarsening

After heat-treated at 1065 ℃, the AM 316L SS exhibited a distinct partially recrystallized microstructure feature (~ 50% recrystallization volume fraction). A difference in inclusion coarsening was observed between recrystallized and un-recrystallized grains, demonstrated by BSE image and TEM image, as shown in Fig. 40. The size of inclusions at the recrystallization front and inside the recrystallized grains was larger than those in the un-recrystallized grains. The data points at 1065 ℃ in Fig. 39 included both inclusions at recrystallized and un-recrystallized grains, each contains measurement results from fifteen BSE images. The analysis of inclusion in recrystallized and un-recrystallized grains was separated and displayed in Fig. 41. The volume fraction of inclusion kept the same, while the average inclusion size at recrystallized grains was 1.5 times larger than those at un-recrystallized grains.

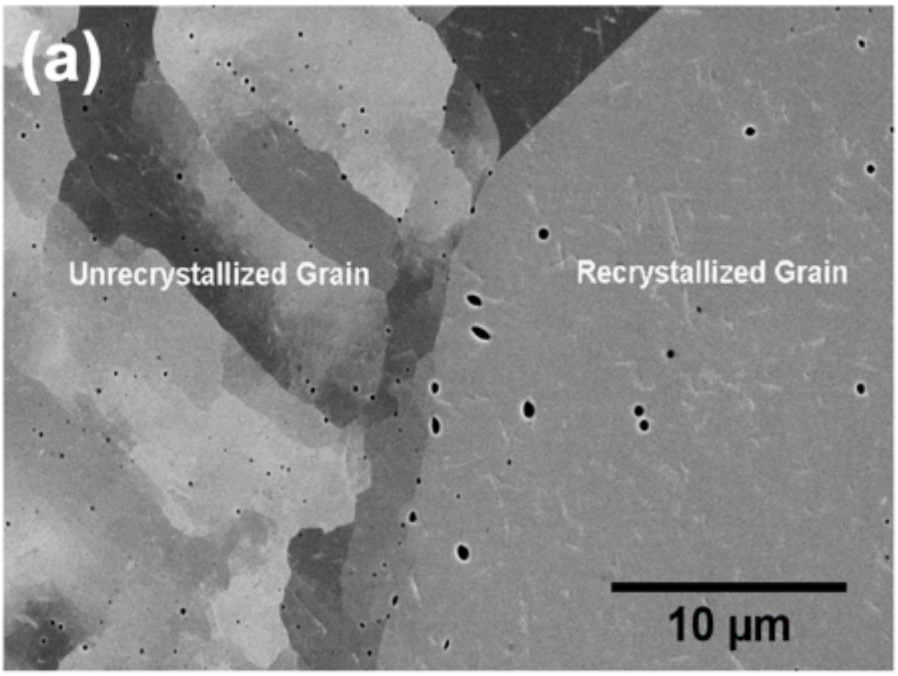

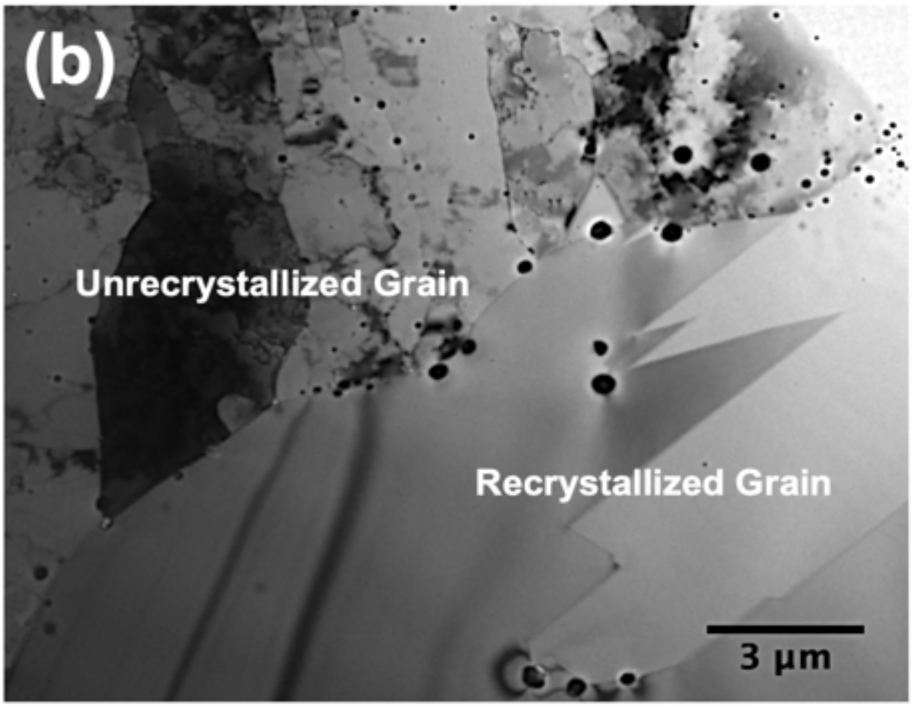

Fig 40 Difference in oxide coarsening between un-recrystallized and recrystallized grains (heat treatment condition: 1065 °C for 0.5 hours), demonstrated by BSE image (a), and TEM image (b).

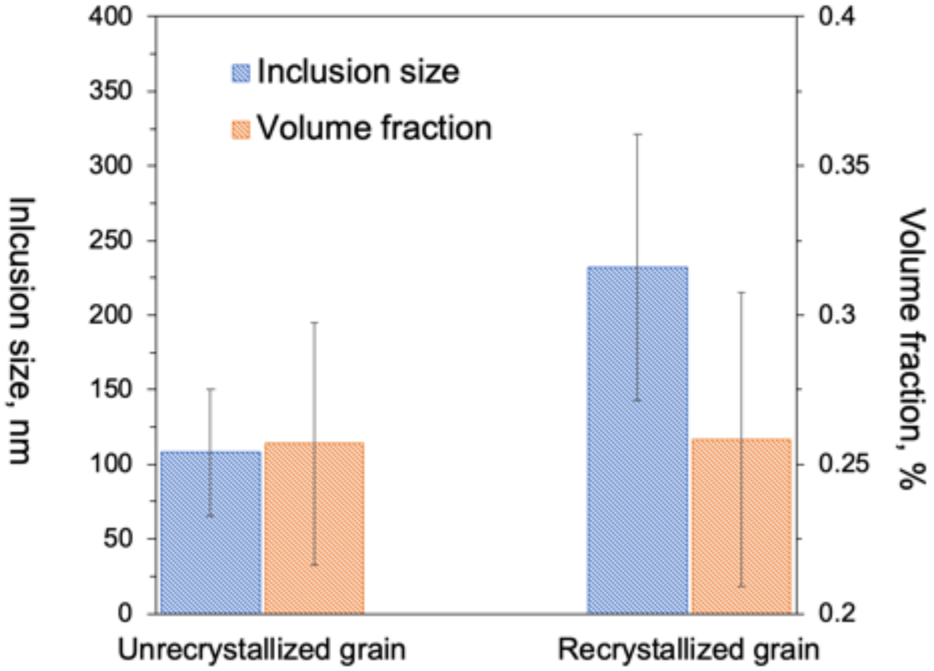

Fig 41 The average size and volume fraction of inclusion at recrystallized and un-recrystallized grains in AM 316L SS heat- treated at 1065 ℃ for 2 hours.

4.3.4 The coarsening of oxide inclusions with time

Owing to the partially recrystallized microstructure of AM 316L SS heat-treated at 1065 ℃, it became a desirable heat treatment temperature to compare the oxide inclusions in the recrystallized grain and the unrecrystallized grain. Moreover, the role of grain boundary migration on oxides could be investigated by increasing heat treatment time. BSE images showing the effect of heat treatment time of AM 316L SS heat-treated at 1065 ℃ were displayed in Fig. 42. After half hour heat treatment at 1065 ℃, most of the grains remained un-recrystallized, while all grains recrystallized to some extent after 50 hours of heat treatment. The size of inclusion increased continuously with time, while the inclusion size at recrystallized grain was always higher than that of at un-recrystallized grain, as shown in Fig. 43. Furthermore, the coarsening rate of oxides in recrystallized grain, represented by the green line in Fig. 43, is higher than that of in the unrecrystallized grain. The grains in AM 316L SS stayed un-recrystallized through 70 hours of heat treatment at 955 ℃, and the average inclusion size increased steadily from 50 nm to 117 nm after 20 hours annealing and further increased by only 20 nm after 70 hours annealing. The inclusions in un-recrystallized grains of 1065 ℃ heat-treated 316L SS grew initially with a similar rate as that of at 955 ℃ heat-treated 316L SS. In contrast, the inclusion size at recrystallized grains raised sharply at the early stage of heat treatment and also stabilized after a long time annealing.

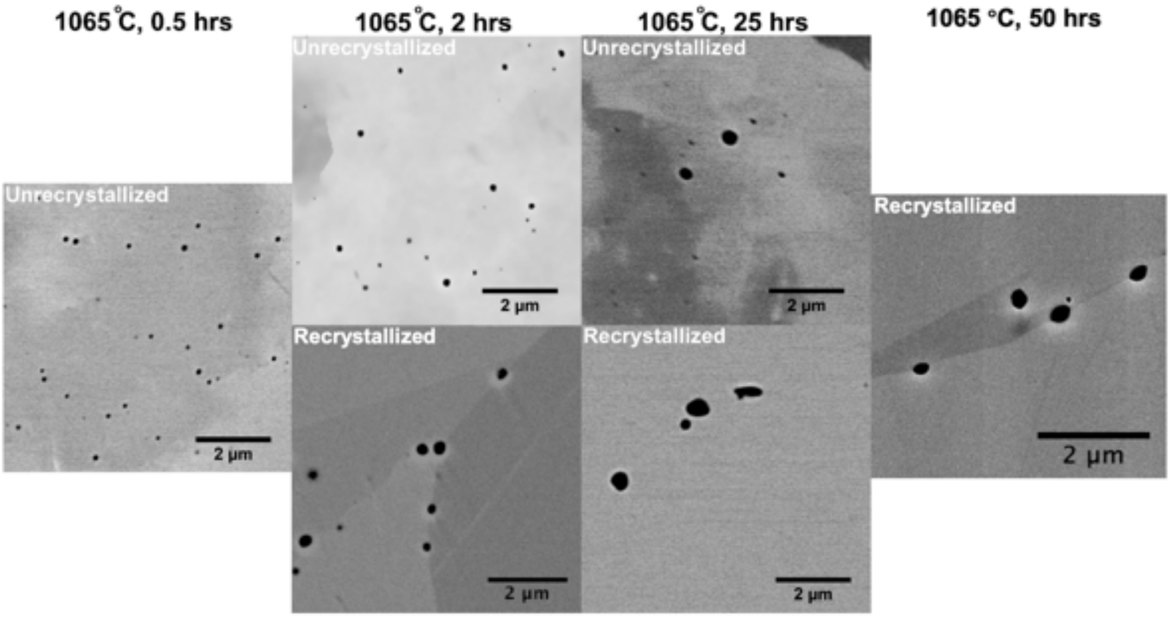

Fig 42 Effect of heat treatment time on oxide inclusion coarsening at 1065 °C: a comparison between un-recrystallized grain and recrystallized grain

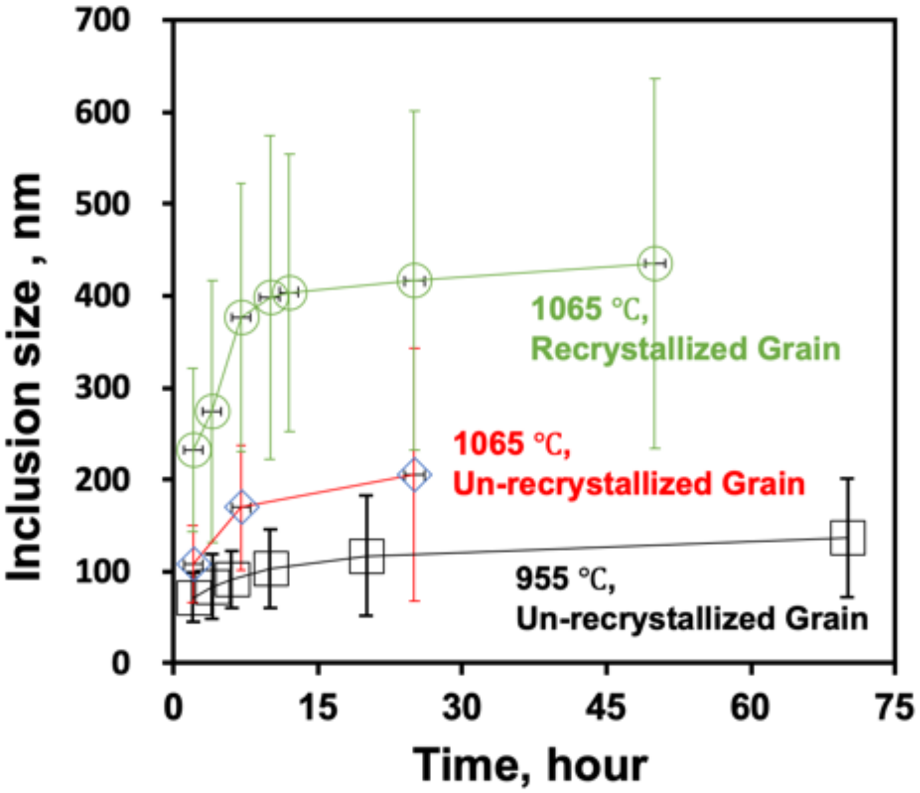

Fig 43 Evolution of inclusion size in AM part over the time: a comparison between un-recrystallized grain and recrystallized grain

4.3.5 The evolution of chemistry and morphology after heat treatment

The chemistry of oxide inclusion in AM part produced by the EOS L-PBF system has been revealed in Fig. 2 and Fig. 4, Si and Mn rich oxides ($MnSiO_3$) were determined. The chemistry and morphology of oxide inclusion in AM 316L SS heat-treated at 1065 ℃ for 0.5 hour were given in Fig. 44. EDX line scan was performed on oxide in recrystallized grain, as shown in Fig. 44(a), same $MnSiO_3$ oxide was determined according to the line profile. Nevertheless, sulfide, more likely MnS due to its lowest Gibbs free energy of formation among sulfide based on Ellingham diagram, was found to precipitate adjacent to $MnSiO_3$. This has been widely studied for cast 316L SS [52] and has been discussed in Chapter 2, section 2.3.2. The formation of sulfide indicated that AM 316L SS might lose its superior corrosion resistance after heat treatment at temperature > 1000 ℃ [55, 56]. The formation of sulfide was also confirmed by the bump of sulfur signal in the line profile. Interestingly, a series of oxides near a grain boundary was discovered to have core/shell structure, which Mn enriches at the shell and Si concentrates at the core, as shown in Fig. 44(b), sulfide was also detected adjacent to the oxides. While in the unrecrystallized grain, as displayed in Fig. 45, Cr and Mn rich oxides were observed. Moreover, with the ultra- high resolution of the TEM/EDX analysis, Al signals were detected in almost all oxides since Al has the an even higher oxygen reactivity than Si and Mn in 316L SS. Although Al is not the regular alloying elements for 316L SS, Al contamination has been widely reported for steel manufacturing [22, 43].

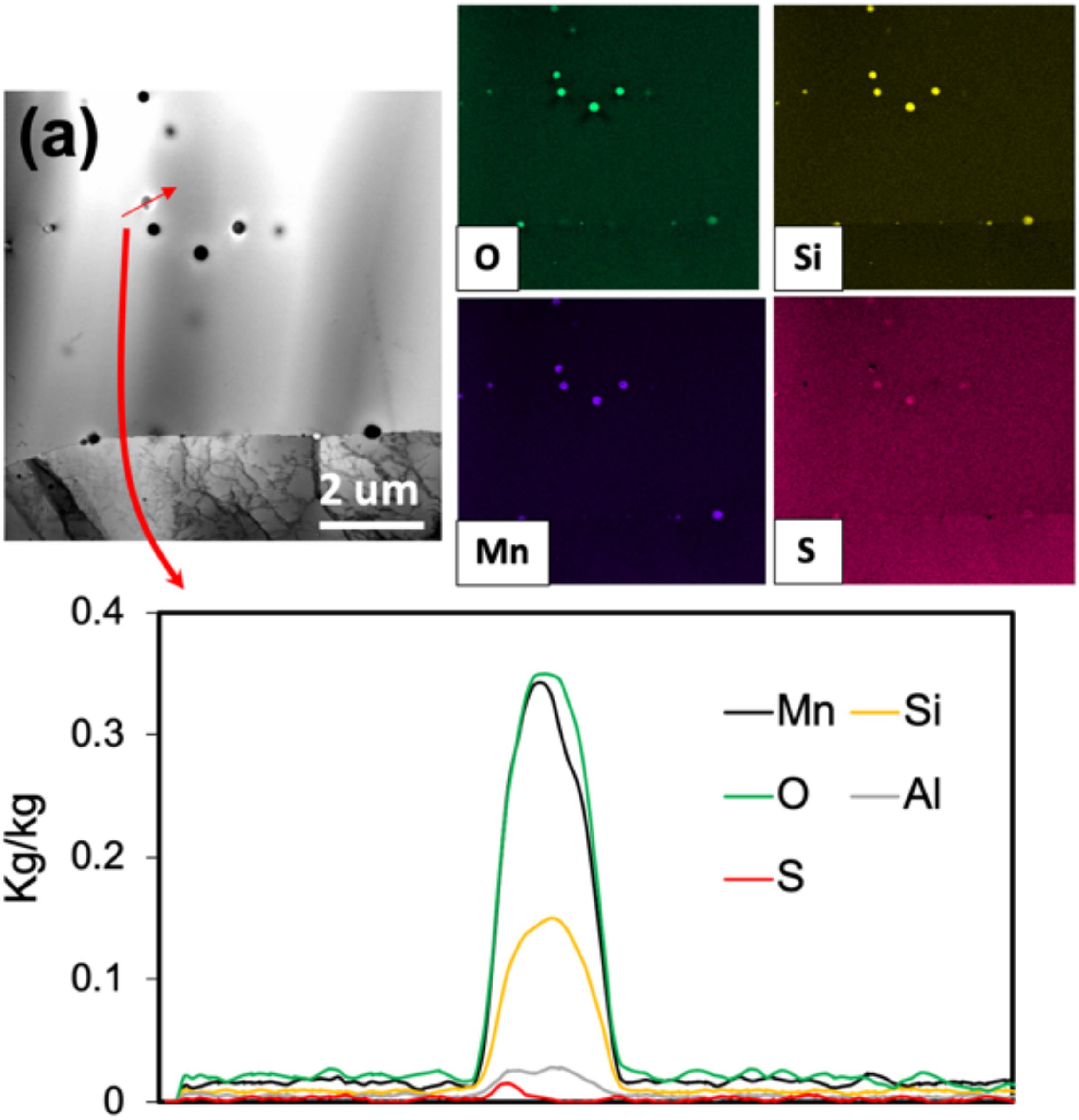
(a)
2 um
O
Si
Mn
S
Kg/kg
0.4
0.3
0.2
0.1
0
Mn
Si
O
Al
S

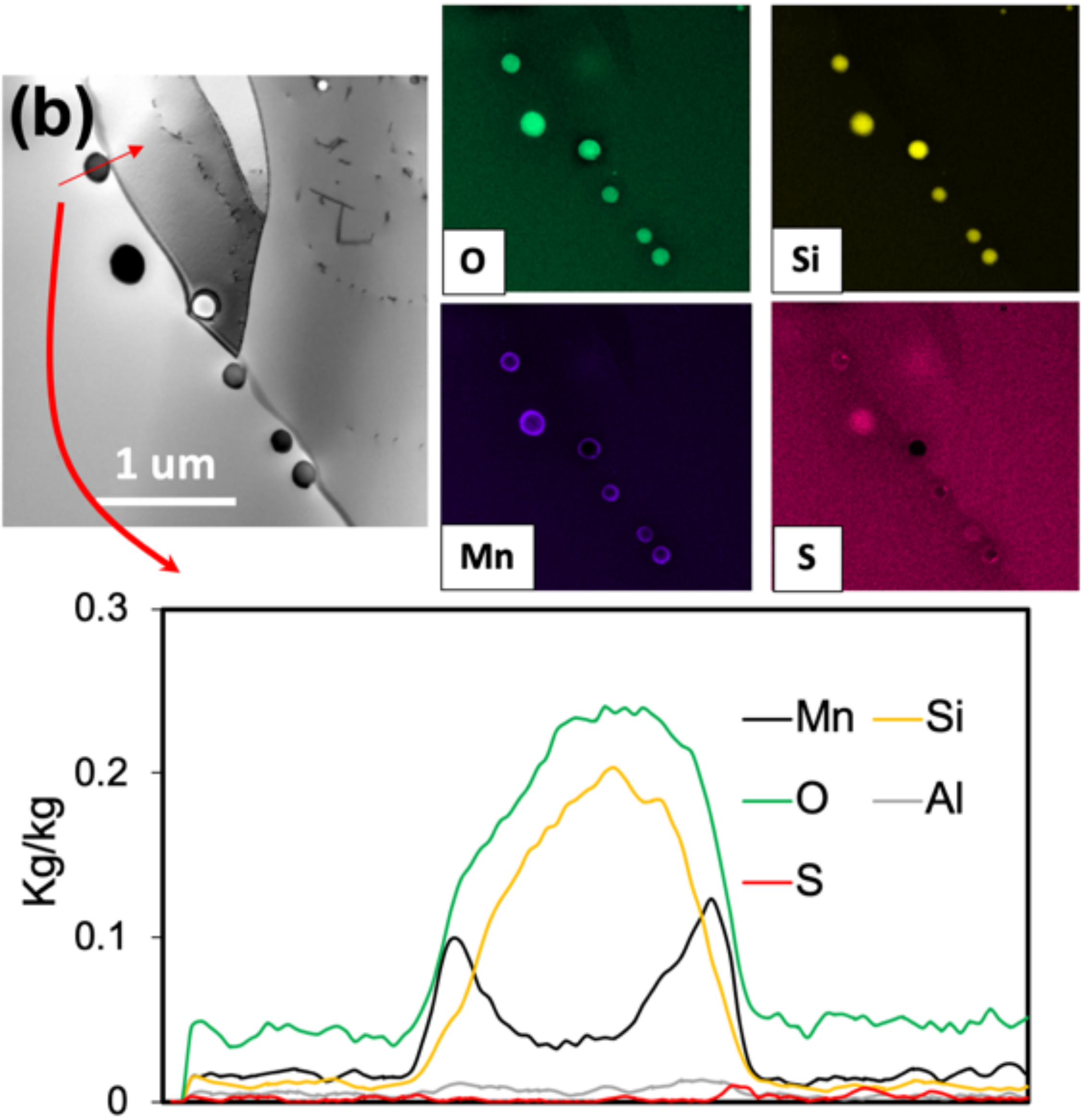

Fig 44 EDX elemental mapping and line profile of $MnSiO_3$ oxide inclusion in recrystallized grain of AM 316L SS after heat-treated at 1065 ℃ for 0.5 hour.

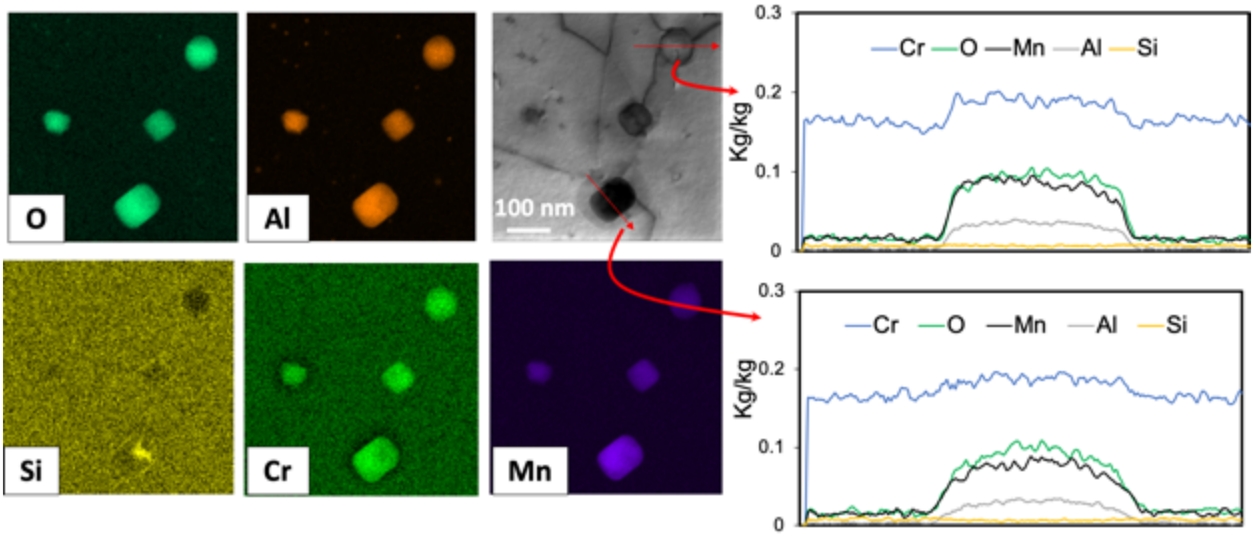

Fig 45 EDX elemental mapping and line profile of $CrMn_2O_4$ oxide inclusion in unrecrystallized grain of AM 316L SS after heat-treated at 1065 ℃ for 0.5 hour.

4.3.6 The distribution of oxides after recrystallization

The distribution of oxides was investigated after heat treatment, it was also discovered to be affected by grain boundary migration. Fig. 46 gave the number percent and volume fraction percent of intergranular and intragranular oxide inclusions at recrystallized grains for AM 316L SS. The analysis method and definition of number percent and volume fraction percent of intergranular and intragranular oxide were given in section 4.2.4. For three heat treatment conditions (1065 ℃ for 2, 12, and 50 hours), fifteen BSE images contain a complete grain were processed by ImageJ. Initially, a high number percent (65%) and volume fraction percent (70%) of oxide inclusions were found to locate at grain boundaries, these numbers dropped to 48% and 57%, respectively, after 50 hours of heat treatment. Considering the effect volume of grain boundaries as compared to grain interiors, the number of 48 % number percent of oxide inclusions and 57 % volume fraction percent of oxide inclusions situated at grain boundaries was significant. The fact that a high fraction of oxides accumulates on grain boundaries indicates that small oxides were dragged by grain boundaries instead of dissolved by grain boundaries in AM 316L SS. Moreover, oxides at grain boundaries were larger than those inside the grain, and this difference increased with holding time. Oxides diffuse through grain boundary seemed to be underlying reason for the rapid coarsening of oxides in recrystallized grain.

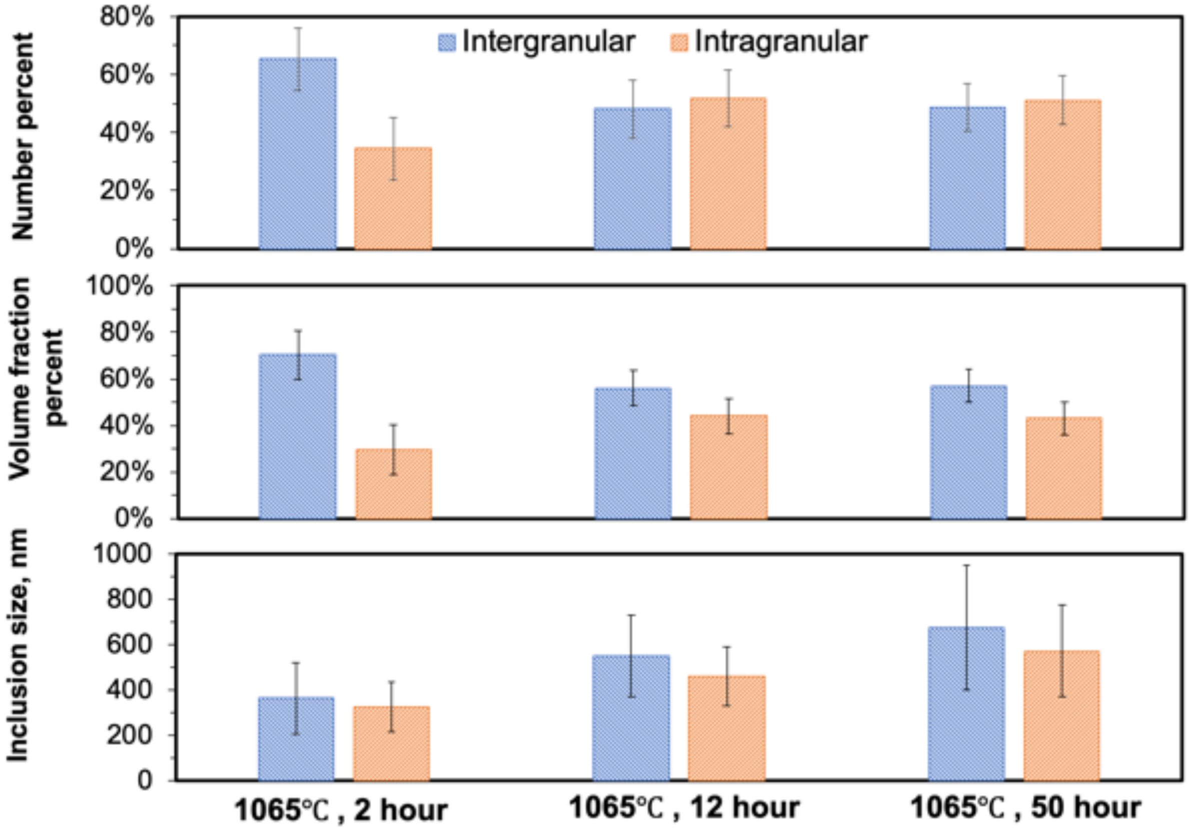

Fig 46 The number percent (a), volume fraction percent (b), and average size of intergranular and intragranular oxides at recrystallized grains for AM 316L SS heat-treated at 1065 ℃ for 2 hours, 12 hours, and 50 hours.

4.4 Discussion

4.4.1 The size evolution of nanoscale oxide in AM 316L SS after heat treatment

According to Fig. 38 and Fig. 39, the nanoscale oxide inclusions coarsened from 50 nm to 392 nm with increasing temperatures of 2 hours' isothermal heat treatment. The volume fraction of inclusion was found to keep constant after heat treatment from 650 ℃ to 1150 ℃, which indicates that the coarsening of oxides in AM 316L SS followed the Ostwald ripening process. The oxides grew slowly at low temperatures (< 950 ℃), while the coarsening rate of oxides at a higher temperature (> 955 ℃) is rather significant. The AM 316L SS remained unrecrystallized at temperature < 955 ℃, and begun to recrystallize since 1065 ℃ where the average oxide size jumped by more than 100 %. Hence, the remarkable coarsening rate of oxide inclusion at high temperature could be related to the recrystallization process.

The microstructure of AM 316L SS heat-treated at 1065 ℃ was further examined by TEM and SEM, as shown in Fig. 40. The TEM image (Fig. 39(b)) exhibited dislocation free recrystallized grain, besides, dislocations were observed in the unrecrystallized grains indicating the ongoing recovery process. Both images revealed that oxide inclusions in the recrystallized region were considerably greater than those in the unrecrystallized region. This was confirmed by the statistical analysis of oxides in different regions displayed in Fig. 41. It indicated that grain boundary migration initiated by recrystallization significantly facilitates oxide coarsening. Due to the partially recrystallized microstructure of AM 316L SS heat-treated at 1065 ℃, longer heat treatment up to 50 hours was conducted to explore the role of grain boundary migration on oxide coarsening. Additionally, the comparison of oxides coarsened in the recrystallized grain and unrecrystallized grain was made, as shown in Fig. 42 and Fig. 43. The AM 316L SS heat-treated at 955 ℃ with the time up to 70 hours was included. It is worth to mention that AM 316L SS remained unrecrystallized at 955 ℃. Fig. 43 suggested that oxide size increased rapidly at the early stage of heat treatment, while the oxides in the recrystallized grain, as denoted by the green line, coarsened with a higher rate than those in the unrecrystallized grain. Due to the fact that a significant amount of oxides with greater size were found to situated at grain boundary of fully recrystallized grain, as shown in Fig. 46, the growth of recrystallized grain, which is equivalent to the migration of grain boundary, appeared to interact with oxides and affect the coarsening of oxides. Therefore, it is reasonable to infer that the rapid coarsening of oxide inclusion was via grain boundary diffusion, which is the fastest diffusion route for polycrystalline material.

After approximately 10 hours of heat treatment at 1065 ℃, the oxide coarsening rate leveled off for both temperatures. The Gibbs-Thomson relation, as shown in equation (2), indicated that the solute concentration at smaller size particle surface is higher than the matrix while larger particle surface has lower solute concentration, which induces a net diffusion flux from small particles to the matrix and transfers to large particles [94]. At the initial stage of heat treatment, the AM 316L SS contained a high number of nanoscale oxide inclusions (< 50 nm), which gives rise to high concentration gradient at these smaller particles surface and eventually high coarsening rate. With the consumption of smaller particles, the average size of inclusions increased with time which alleviates the coarsening rate.

4.4.2 The chemistry evolution of nanoscale oxide in AM 316L SS after heat treatment

As shown in Fig. 45, $MnSiO_3$ oxides in as-built AM 316L SS converted to Cr and Mn rich oxides. This transformation was found for oxides in the unrecrystallized grain. Yan et al. characterized the oxides in AM 316L SS heat-treated at 1200 ℃ for 1 hour with partially recrystallized microstructure [5]. They reported the formation of prismatic shape Cr and Mn rich oxides, which was identified as $CrMn_2O_4$ by diffraction pattern, in the unrecrystallized grain according to the attached TEM image. Thermodynamic calculations were performed, and their results indicated that spinel $CrMn_2O_4$ and MnS are stable phases at temperatures between 1000 ℃ to 1200 ℃. Therefore, the transformation from $MnSiO_3$ to $CrMn_2O_4$ was a thermodynamically favorable process.

Fig. 44(b) revealed that a line of $MnSiO_3$ oxides near/at the grain boundary have a core-shell structure with Si-rich cores and Mn-enriched shells, as compared to normal coarsened $MnSiO_3$ oxides, as shown in Fig. 44(b). The formation of large oxides was through the diffusion of solute from the matrix to the surface of larger particles. For $MnSiO_3$ oxide inclusion, the activation of Si diffusion in gamma iron is approximately 25 kJ/mol, and Mn diffusion in iron has the similar activation energy as Fe diffusion in iron (the activation energy of Fe grain boundary diffusion and lattice diffusion are approximately 140 kJ/mol and 280 kJ/mol, respectively.) [112, 113]. The activation of O diffusion is 96 kJ/mol [114]. As mentioned earlier, grain boundary diffusion was considered as the diffusion route for oxides in and near recrystallized grain. Therefore, faster diffusion velocity of Si and O through rapid diffusion path could be the underlying formation mechanism of the core-shell structure. The core-shell structure of oxides in oxide-dispersion strengthened Fe-Cr alloy has been reported [115]. The Y-rich core and solute rich shell was observed, and it was suggested that the formation of this structure could be govern by interfacial energy between oxides and matrix. The Y_2O_3 with the lowest Gibbs free energy of formation among all solutes in their alloys may have a high nucleation barrier, and the formation of a shell could decrease its interfacial energy. More investigation is needed to elucidate the cause of the core-shell structure. Moreover, the high thermal stability of Cr rich oxides could be another reason of the lower coarsening rate of oxides in the unrecrystallized grain. The chemistry investigation of oxides done by TEM so far implies that the transformation from $MnSiO_3$ to $CrMn_2O_4$ occurs in unrecrystallized grain, although this requires more quantitative analysis to confirm, it was inferred that the slow diffusion rate in unrecrystallized grain could be the underlying cause. The slow diffusion makes the nucleation of $CrMn_2O_4$ oxides a more effective way to reduce the total energy of the system.

4.4.3 The distribution of oxides after recrystallization

In the Introduction part, section 4.1, the debate of how the grain boundary migration facilitated the coarsening of particles has been introduced. In the present work, a high fraction of oxides accumulated on grain boundaries indicated that small oxides were dragged by grain boundary instead of dissolved by migrating grain boundaries and reprecipitate out. The forward force from grain boundary migration exerts on second phase particles has been calculated, which was several orders of magnitude higher than the gravity of inclusions and thus enables the dragging of particles by grain boundaries [104]. Moreover, the inclusions in solids are not immobile, and the particle mobility drastically increases with decreasing particle radius, hence, the nanoscale oxide inclusions in AM 316L SS have fairly high mobility. These small oxides can be directly dragged through volume diffusion of matrix atom (Fe in this case) or interfacial diffusion (as the matrix atom move and the vacancy behind was occupied by oxides molecule, hence the oxides move with grain boundary molecule by molecule or atom by atom) [98, 104, 105].

The increasing heat treatment time at 1065 ℃ is accompanied by the continuing recrystallization process, and this led to the decrease of number percent and volume fraction percent of intergranular oxides, as shown in Fig. 46. It implied that as the growth of oxides, some of them were detached from migrating grain boundaries. The growth of grain decreased the driving force of grain boundary migration, and the large oxides can no longer be dragged, this is evidenced by Fig. 47. At the initial stage of heat treatment, although the small size oxides exert a higher pinning force on grain boundary, the newly nucleated grain boundary with a high driving force dragged a significant number of oxides.

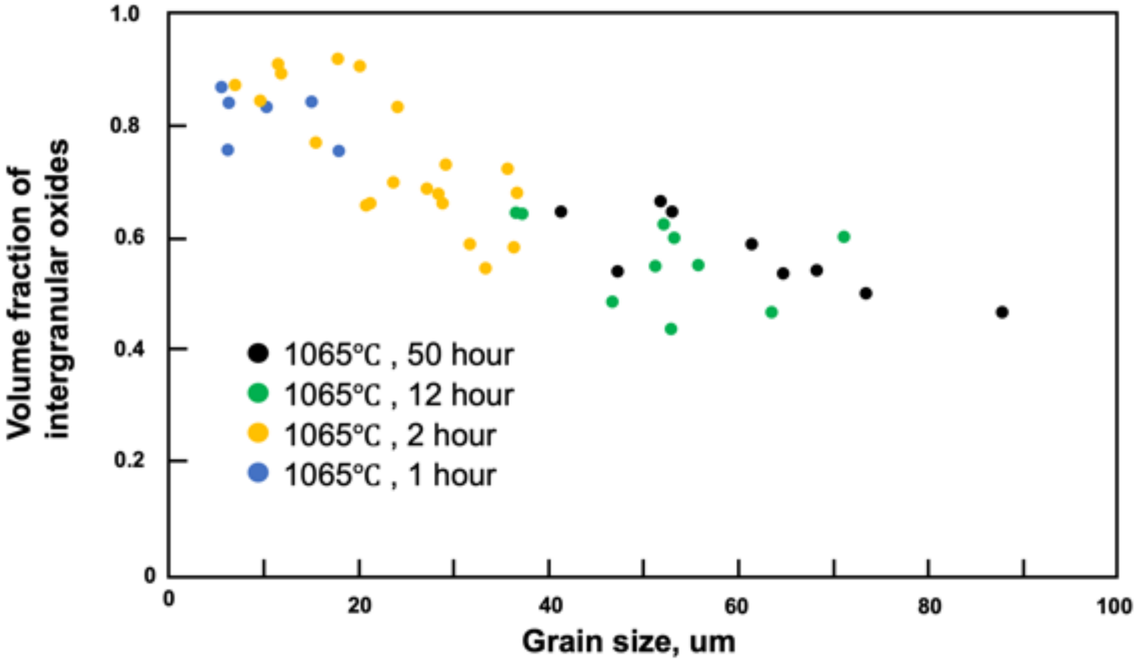

Fig 47 The plot of grain size versus volume fraction of intergranular oxides of AM 316L SS heat-treated at 1065 ℃ for 1 hour, 2 hours, 12 hours, and 50 hours.

As the oxides and grain boundary moving jointly, oxide inclusions accumulate at grain boundaries coarsening more rapidly than intragranular oxides owing to the much shorter diffusion path and faster diffusion route. With the migration of grain boundaries, the driving force decreases with increasing grain size, meanwhile, the inclusions also coarsening which leads to lower pinning force on grain boundaries. At a certain point, large oxides detached from moving grain boundary and left behind. As the grain boundary continuously migrated, it may again drag small oxides and move along with them. The average size of oxides at grain boundaries was always found to be larger than the intragranular oxides since (1) a portion of oxides were never dragged by grain boundaries and coarsened through lattice diffusion and (2) the coarsening through grain boundary was rapid enough. Oxide coarsening with grain growth was shown in Fig. 48. Both the size of intragranular oxides and intergranular oxides increased significantly at early stage of annealing, which implies that the drag and then detachment of oxides with grain boundary was a dynamic process during the heat treatment. There was an only minor increase of grain size from 12 hours to 50 hours, as indicated by the green and black symbols in the Fig. 48. As a result, the coarsening rate of both oxides leveled off with further heat treatment.

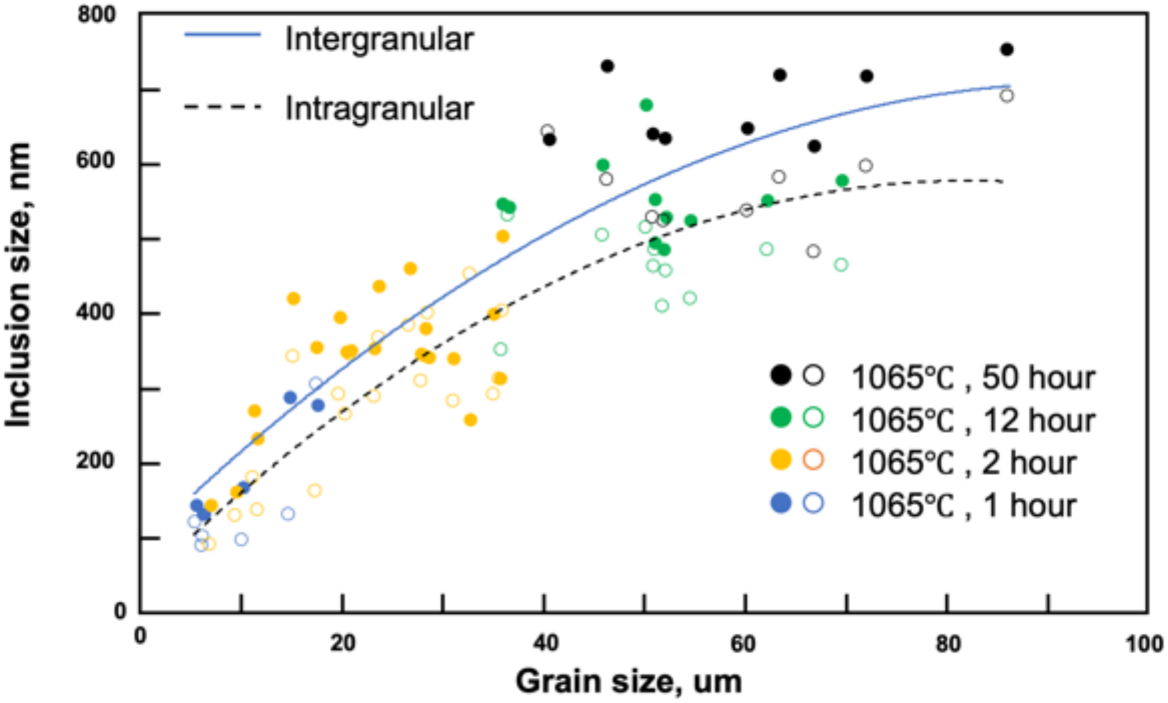

Fig 48 The plot of grain size versus average size of intergranular and intragranular oxides of AM 316L SS heat-treated at 1065 ℃ for 1 hour, 2 hours, 12 hours, and 50 hours.

4.4.4 The kinetic study of oxide coarsening

According to the kinetic relationship for particle coarsening through Ostwald ripening process [116]:

$$d^3 - d_0^3 = k \cdot t \qquad (5)$$

where d and d_0 is the particle radius after and before heat treatment, respectively, t is the heat treatment time, k is the rate constant for coarsening and can be express as $k = k_0 \exp(-Q/RT)$, where k_0 (preexponent) and Q (activation energy) are approximately independent of T (temperature).

Taking logarithm for eq. (5), it gives:

$$\ln(d^3 - d_0^3) = \ln k + \ln t \tag{6}$$

Substituting $k = k_0 \exp(-Q/RT)$ in eq. (6):

$$\ln(d^3 - d_0^3) = -\frac{Q}{R}\left(\frac{1}{T}\right) + \ln k_0 + \ln t \tag{7}$$

$\ln(d^3 - d_0^3)$ was plotted versus $1/T$ using the adopted exponent value for the same heat treatment time (2 hours), the activation energy (Q_a) can be obtained from the slope, the plots and corresponding Q_a were given in Fig. 49.

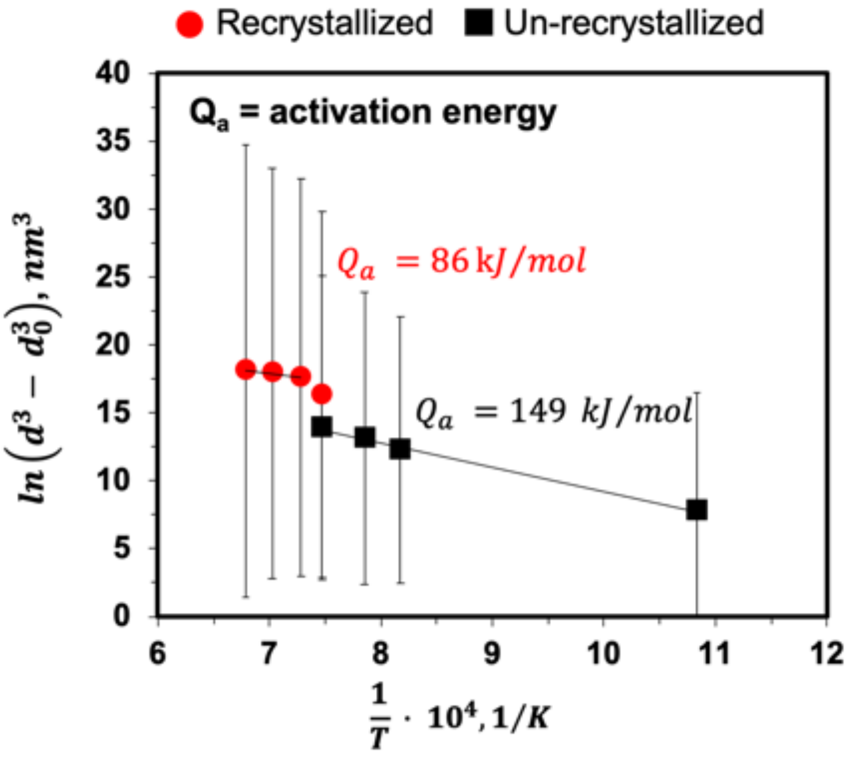

Fig 49 The plot of $\ln(d^3 - d_0^3)$ versus $1/T$ for unrecrystallized grain (T = 650 ℃, 955 ℃, 1000 ℃, and 1065 ℃) and recrystallized grain (T = 1065 ℃, 1100 ℃, 1150 ℃, and 1200 ℃), and activation energies (Q_a) measured from the slope. The annealing time for all temperatures was kept for 2 hours.

At low temperature (< 0.75 - 0.8 T_m), the diffusion kinetics in polycrystalline metal is usually dominated by a faster diffusion route, such as grain boundary diffusion or dislocation pipe diffusion [117]. Fig. 2 and Fig. 35 illustrated that oxide inclusion in as-built AM 316L SS decorated along the cellular walls and situated at grain boundaries. The cellular walls have been demonstrated to be composed of tangled dislocations, as shown in Fig. 50 (a). Moreover, since dislocation cellular structure was observed in almost all grains, all dislocations were considered to originate from the cellular structure. Hence, other than grain boundary diffusion, dislocation pipe diffusion could be involved in oxide coarsening. However, the dislocation cellular structure disappeared at 955 ℃ after only half-hour heat treatment indicating the annihilation of dislocations during the recovery process, as evidenced by Fig. 50 (b) and (c). The dislocation cellular structure can be revealed by etching using mixed acids (HCl: HNO_3: H_2O = 4:1:3) via immersion for 75 s. This indicated that dislocation density reduced quickly at 955 ℃, the coarsening of oxides at low temperature was govern by grain boundary diffusion. It is worth noting that as-built AM 316L SS contains a significant fraction of high angle grain boundaries (59 %) [12].

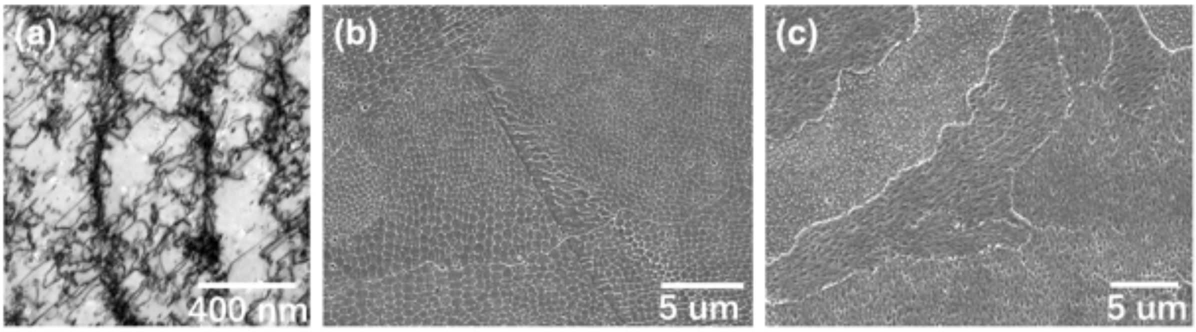

Fig 50 (a) TEM image showing the dislocation cellular structure of as-built AM 316L SS; (b) cellular structure of as-built AM 316L SS revealed by etching; (c) the disappearance of cellular structure of AM 316L SS after heat-treated at 955 °C for 0.5 hour.

At higher temperatures, due to the low effective thickness of grain boundary comparing to grain, the diffusion is usually dominated by lattice diffusion. Hence, higher activation energy was obtained, as shown in Fig. 51. In general, the activation energy of lattice diffusion is around two times of activation energy of grain boundary diffusion. However, according to Fig. 49, the activation energy of oxide coarsening at high temperature (> 0.76 T_m) is lower than that of activation energy of oxide coarsening at low temperature (< 0.76 T_m). The melting point of 316L SS is approximately 1400 °C, 0.76 is obtained by 1065 °C divided by 1400 °C. The AM 316L SS heat-treated at 1065 °C for 2 hours exhibited partially (50%) recrystallized microstructure structure, thus 1065 °C is a transition temperature for oxide coarsening. At 1100 °C, AM 316L SS became almost recrystallized. Thus, the 1065 °C was not adopted for calculating the activation energy. This discontinuity could be attributed to the different properties of grain boundaries. At the early stage of recrystallization, the newly nucleated grain grew by consuming the stored energy in the deformed grain. While in the recrystallized grain, the migration of grain boundary is driven by the reduction of grain boundary energy. Grain boundaries in recrystallized grain may have a higher misorientation angle. The low activation energy of oxide coarsening at high temperature implies the significant involvement of grain boundary diffusion due to the dragging effect.

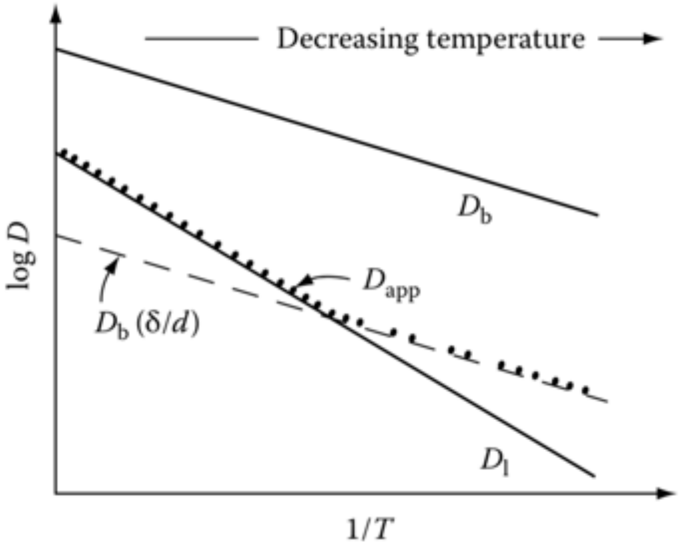

Fig 51 Diffusion in a polycrystalline metal. D_b is grain boundary diffusion diffusivity, D_l is lattice diffusion diffusivity, $D_{app} = D_l + D_b\delta/d$, where δ and d is effective thickness of grain boundary and grain size [117].

4.4.5 The interaction between oxides and grain boundary migration

Schematic shown in Fig. 50 illustrates the interactions between migrating grain boundary and oxides in AM 316L SS. Grain boundary migration initiated by the nucleation of new grains, driven by the reduction of stored energy or the reduction of grain boundary energy afterward, could drag a high number of oxides and move jointly. As oxides accumulated at grain boundaries, small oxides dissolved, and atoms diffused to large oxides with shorter diffusion path. The grain boundary provided a diffusion highway for atoms. As a result, oxides situated at grain boundary coarsened rapidly during the joint movement. When the oxides become large, and at the same time, the increasing grain size led to a lower driving force for grain boundary migration, large oxides detached from grain boundary. Grain boundaries with enough driving force would move continuously towards deformed grain or smaller grain, and small oxides could still be dragged. Eventually, the driving force decreased to a value that grain boundaries stopped migration, and some oxides stayed at grain boundaries. This process caused a high fraction of oxides gathered at grain boundaries at the early stage of recrystallization and when the grains were small, and this fraction decreases with grain size. Due to the rapid diffusion at grain boundaries, the average size of oxides at grain boundaries was always higher than those inside the grain.

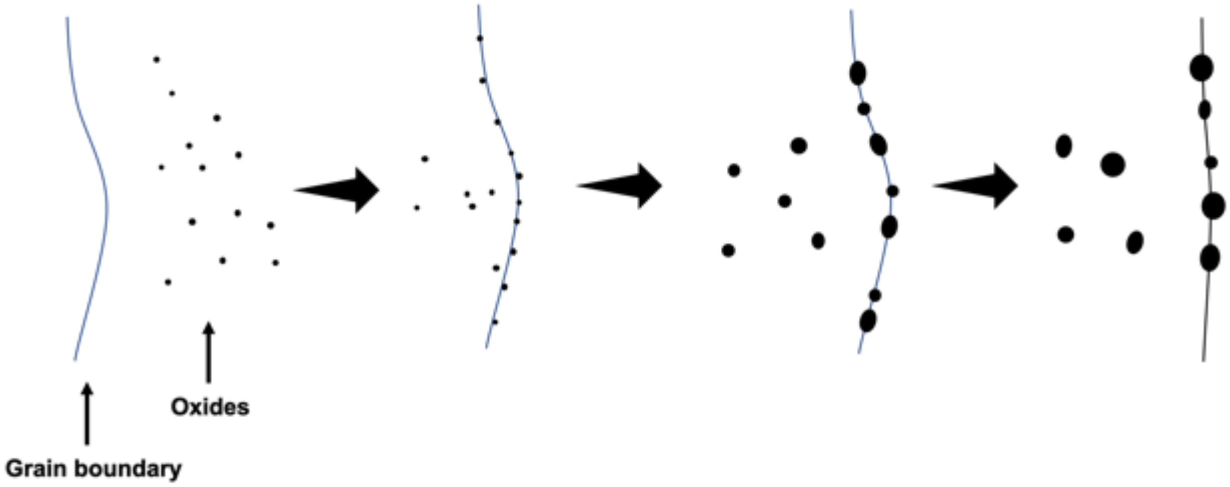

Fig 52 Schematic depicting interaction between oxides and migrating grain boundary.

4.5 Conclusion in this chapter

The evolution of nanoscale oxide inclusions in AM 316L SS was investigated as a function of temperature and heat treatment time. Three aspects of evolution were explored, size, chemistry and morphology, and distribution. Experiments, along with statistical analysis, indicated that grain boundary migration during the recrystallization process played a critical role in the evolution of nanoscale oxides. The summary of findings is listed as follows:

- The coarsening of nanoscale oxides obeys Ostwald ripening theory, it represents that smaller oxides shrink while larger oxides grow.
- The increasing average size of oxides lowered the solute concentration in the matrix, as a result, the coarsening rate decreased due to the reduction of the concentration gradient at the larger particle surface.

- Some $MnSiO_3$ oxides in the recrystallized grain have core-shell with Si-rich cores and Mn-enriched shells, this could be attributed to the faster diffusivity of Si and O atoms or the reduced interfacial energy by Mn-rich shell.
- Some $MnSiO_3$ oxides in the unrecrystallized grain converted $CrMn_2O_4$ since it is the stable phase between 1000 ℃ to 1200 ℃.
- Grain boundary dragging led to a high fraction of oxides accumulated at the grain boundary, and this fraction decreases with grain size.
- The joint movement of grain boundary and oxides resulted in significant coarsening of oxides due to the shorter diffusion path and faster diffusion route along the grain boundary.

Conclusion

Owing to the high concentration of oxygen exists in AM 316L SS comparing to its conventional made counterparts, and the critical role of oxides on mechanical properties, the origin and formation of oxide inclusions were investigated. The primary contributor to oxygen in AM parts without environmental oxygen contamination was found to be the precursor powder, more specifically, oxide inclusions in precursor powder. Increasing the oxygen content in the process chamber and the contamination from moisture both could lead to a higher volume fraction of oxides. However, the strengthening effect from the extra uniformly dispersed nanoscale oxides was not observed. The increase of the volume fraction of oxide inclusion has a minor effect on yield strength, ductility, hardness, and Charpy impact toughness. Worse than this, moisture has shown to reduce the hardness. The surface oxidation of spatter particles that deposit back into the melt pool has been identified as the dominant path for oxygen from L-PBF process environment to the final AM part. Moreover, removing traditional oxygen getters, Si and Mn, does not mitigate the oxygen contamination, Cr rich oxides can form instead. The spattering behavior was further studied, and it was found that the incorporation of spatter particles on as-printing AM parts can be significantly affected by the laser scan strategy. Lase scans against the direction of gas flow can lead to a lower amount of spatter particle deposition on as-printing parts. However, the tensile properties were found to not affected by the spatter particles. The nanoscale oxides presented in AM 316L SS was discovered to evolve into different forms after heat treatment. The oxides coarsening obeys the Ostwald ripening process, and this process was significantly facilitated by recrystallization. $MnSiO_3$ oxides with core-shell structure, which contains Mn-rich shell and Si-rich core, were observed in recrystallized grain, and $CrMn_2O_4$ oxides were discovered in the unrecrystallized grain. Grain boundary dragging led to a high fraction of oxides accumulated at the grain boundary, and as a result, these oxides coarsened rapidly through grain boundary diffusion.

References

[1] T. DebRoy, H.L. Wei, J.S. Zuback, T. Mukherjee, J.W. Elmer, J.O. Milewski, A.M. Beese, A. Wilson-Heid, A. De, W. Zhang, Additive manufacturing of metallic components – Process, structure and properties, Progress in Materials Science 92 (2018) 112-224.
[2] S. Irukuvarghula, H. Hassanin, C. Cayron, M. Aristizabal, M.M. Attallah, M. Preuss, Effect of powder characteristics and oxygen content on modifications to the microstructural topology during hot isostatic pressing of an austenitic steel, Acta Materialia 172 (2019) 6-17.
[3] J.O.M.B. J. A. Kitchenr., Molly Gleiser and J.W. Evans, Note on the solubility of oxygen in gamma iron, Transactions of the Faraday Society 48 (1952) 995-997.
[4] J.L. Meijering, On the diffusion of oxygen through solid iron, ACTA METALLURGICA 3 (1955) 157-162.
[5] F. Yan, W. Xiong, E. Faierson, G.B. Olson, Characterization of nano-scale oxides in austenitic stainless steel processed by powder bed fusion, Scripta Materialia 155 (2018) 104-108.
[6] A.E. Wilson-Heid, T.C. Novak, A.M. Beese, Characterization of the Effects of Internal Pores on Tensile Properties of Additively Manufactured Austenitic Stainless Steel 316L, Experimental Mechanics (2018).
[7] C. Qiu, M.A. Kindi, A.S. Aladawi, I.A. Hatmi, A comprehensive study on microstructure and tensile behaviour of a selectively laser melted stainless steel, Sci Rep 8(1) (2018) 7785.
[8] N. Chen, G. Ma, W. Zhu, A. Godfrey, Z. Shen, G. Wu, X. Huang, Enhancement of an additive-manufactured austenitic stainless steel by post-manufacture heat-treatment, Materials Science and Engineering: A 759 (2019) 65-69.
[9] K. Saeidi, L. Kvetková, F. Lofaj, Z. Shen, Austenitic stainless steel strengthened by the in situ formation of oxide nanoinclusions, RSC Advances 5(27) (2015) 20747-20750.
[10] Y. Zhong, L. Liu, S. Wikman, D. Cui, Z. Shen, Intragranular cellular segregation network structure strengthening 316L stainless steel prepared by selective laser melting, Journal of Nuclear Materials 470 (2016) 170-178.
[11] W.M. Tucho, V.H. Lysne, H. Austbø, A. Sjolyst-Kverneland, V. Hansen, Investigation of effects of process parameters on microstructure and hardness of SLM manufactured SS316L, Journal of Alloys and Compounds 740 (2018) 910-925.
[12] Y.M. Wang, T. Voisin, J.T. McKeown, J. Ye, N.P. Calta, Z. Li, Z. Zeng, Y. Zhang, W. Chen, T.T. Roehling, R.T. Ott, M.K. Santala, P.J. Depond, M.J. Matthews, A.V. Hamza, T. Zhu, Additively manufactured hierarchical stainless steels with high strength and ductility, Nat Mater 17(1) (2018) 63-71.
[13] Q. Chao, V. Cruz, S. Thomas, N. Birbilis, P. Collins, A. Taylor, P.D. Hodgson, D. Fabijanic, On the enhanced corrosion resistance of a selective laser melted austenitic stainless steel, Scripta Materialia 141 (2017) 94-98.

[14] X. Lou, P.L. Andresen, R.B. Rebak, Oxide inclusions in laser additive manufactured stainless steel and their effects on impact toughness and stress corrosion cracking behavior, Journal of Nuclear Materials 499 (2018) 182-190.

[15] J.H. Park, Y. Kang, Inclusions in Stainless Steels − A Review, steel research international 88(12) (2017).

[16] M.G.H.a.J.J. Moore, Influence of inclusions and heat treated microstructure on hydrogen assisted fracture properties of AISI 316 stainless steel, Engineering Fracture Mechanics 22 (1985) 93-100.

[17] J. Chao, C. Capdevila, Anisotropy in Mechanical Properties and Fracture Behavior of an Oxide Dispersion Fe20Cr5Al Alloy, Metallurgical and Materials Transactions A 45(9) (2014) 3767-3780.

[18] V.I.S. V.V. Sagaradze, V.L. Arbuzov, B.N. Goshchitskii, Yun Tian, Wan Qun, Sun Jiguang Radiation resistance and thermal creep of ODS ferritic steels, Journal of Nuclear Materials 295 (2001) 265-272.

[19] P.J.M. R.L. Klueh, I.S. Kim b, L. Heatherly, D.T. Hoelzer, N. Hashimoto, E.A. Kenik, K. Miyahara, Tensile and creep properties of an oxide dispersion-strengthened ferritic steel, Journal of Nuclear Materials 307 (2002).

[20] S. Ukai, T. Okuda, M. Fujiwara, T. Kobayashi, S. Mizuta, H. Nakashima, Characterization of High Temperature Creep Properties in Recrystallized 12Cr-ODS Ferritic Steel Claddings, Journal of Nuclear Science and Technology 39(8) (2002) 872-879.

[21] A.M. R. Lindau, M. Schirra, P. Schlossmacher, M. Klimenkov, Mechanical and microstructural properties of a hipped RAFM ODS-steel, Journal of Nuclear Materials 307 (2002).

[22] Z. Oksiuta, P. Olier, Y. de Carlan, N. Baluc, Development and characterisation of a new ODS ferritic steel for fusion reactor application, Journal of Nuclear Materials 393(1) (2009) 114-119.

[23] L.L. Hsiung, M.J. Fluss, S.J. Tumey, B.W. Choi, Y. Serruys, F. Willaime, A. Kimura, Formation mechanism and the role of nanoparticles in Fe-Cr ODS steels developed for radiation tolerance, Physical Review B 82(18) (2010).

[24] S.-K. Rittinghaus, M.B. Wilms, Oxide dispersion strengthening of γ-TiAl by laser additive manufacturing, Journal of Alloys and Compounds 804 (2019) 457-460.

[25] H. Springer, C. Baron, A. Szczepaniak, E.A. Jägle, M.B. Wilms, A. Weisheit, D. Raabe, Efficient additive manufacturing production of oxide- and nitride-dispersion-strengthened materials through atmospheric reactions in liquid metal deposition, Materials & Design 111 (2016) 60-69.

[26] C. Kenel, K. Dawson, J. Barras, C. Hauser, G. Dasargyri, T. Bauer, A. Colella, A.B. Spierings, G.J. Tatlock, C. Leinenbach, K. Wegener, Microstructure and oxide particle stability in a novel ODS γ-TiAl alloy processed by spark plasma sintering and laser additive manufacturing, Intermetallics 90 (2017) 63-73.

[27] C. Kenel, G. Dasargyri, T. Bauer, A. Colella, A.B. Spierings, C. Leinenbach, K. Wegener, Selective laser melting of an oxide dispersion strengthened (ODS) γ-TiAl alloy towards production of complex structures, Materials & Design 134 (2017) 81-90.

[28] A.J. Cooper, N.I. Cooper, J. Dhers, A.H. Sherry, Effect of Oxygen Content Upon the Microstructural and Mechanical Properties of Type 316L Austenitic Stainless Steel Manufactured by Hot Isostatic Pressing, Metallurgical and Materials Transactions A 47(9) (2016) 4467-4475.

[29] A.J. Cooper, Mechanistic studies on type 300 stainless steels manufactured by hot isostatic pressing: the impact of Oxygen involvement on fracture behaviour, American Society of Mechanical Engineers (2016).

[30] M.J. Heiden, L.A. Deibler, J.M. Rodelas, J.R. Koepke, D.J. Tung, D.J. Saiz, B.H. Jared, Evolution of 316L stainless steel feedstock due to laser powder bed fusion process, Additive Manufacturing 25 (2019) 84-103.

[31] J.A. Slotwinski, E.J. Garboczi, P.E. Stutzman, C.F. Ferraris, S.S. Watson, M.A. Peltz, Characterization of Metal Powders Used for Additive Manufacturing, J Res Natl Inst Stand Technol 119 (2014) 460-93.

[32] J.H. Tan, W.L.E. Wong, K.W. Dalgarno, An overview of powder granulometry on feedstock and part performance in the selective laser melting process, Additive Manufacturing 18 (2017) 228-255.

[33] F. Radjai, A. Rescaglio, J. Schockmel, N. Vandewalle, G. Lumay, S. Nezamabadi, S. Luding, J.Y. Delenne, Combined effect of moisture and electrostatic charges on powder flow, EPJ Web of Conferences 140 (2017).

[34] E.O. Olakanmi, Effect of mixing time on the bed density, and microstructure of selective laser sintered (sls) aluminium powders, Materials Research 15(2) (2012) 167-176.

[35] D.-R. Eo, S.-H. Park, J.-W. Cho, Inclusion evolution in additive manufactured 316L stainless steel by laser metal deposition process, Materials & Design 155 (2018) 212-219.

[36] M. Song, X. Lin, F. Liu, H. Yang, W. Huang, Effect of environmental oxygen content on the oxide inclusion in laser solid formed AISI 420 stainless steel, Materials & Design 90 (2016) 459-467.

[37] A. E1245-03, Standard Practice for Determining the Inclusion or Second-phase Constituent Content of Metals by Automatic Image Analysis, ASTM International, 100 Barr Harbor Drive, West Conshohocken, PA 19428, USA (2003).

[38] A. E1019-18, Standard Test Methods for Determination of Carbon, Sulfur, Nitrogen, and Oxygen in Steel, Iron, Nickel, and Cobalt Alloys by Various Combustion and Fusion Techniques, ASTM International, West Conshohocken, PA (2018).

[39] A. E2109-01, Standard Test Methods for Determining Area Percentage Porosity in Thermal Sprayed Coatings, ASTM International, 100 Barr Harbor Drive, West Conshohocken, PA 19428, USA (2014).

[40] S. Sgobba, T. Daniellou, Effects of thermocapillary forces during welding of 316L-type wrought, cast and powder metallurgy austenitic stainless steels, Journal of Materials Processing Technology 143-144 (2003) 578-583.

[41] E. Ahmadi, A.R. Ebrahimi, Welding of 316L Austenitic Stainless Steel with Activated Tungsten Inert Gas Process, Journal of Materials Engineering and Performance 24(2) (2014) 1065-1071.

[42] R.Y. Mikio SUZUKI, Katsuhiko MURAKAMI and Masayuki NAKADA, Inclusion Particle Growth during Solidification of Stainless Steel, ISIJ International 41(3) (2001) 247-256.

[43] X. Yin, Y.H. Sun, Y.D. Yang, X.F. Bai, X.X. Deng, M. Barati, A. McLean, Inclusion evolution during refining and continuous casting of 316L stainless steel, Ironmaking & Steelmaking 43(7) (2016) 533-540.

[44] M. HOJO, Oxide Inclusion Control in Ladle and Tundish for Producing Clean Sta inless Steel, ISIJ International 36 (1996) S128-S131.

[45] K.-H. Tseng, P.-Y. Chen, Effect of TiO2Crystalline Phase on Performance of Flux Assisted GTA Welds, Materials and Manufacturing Processes 31(3) (2015) 359-365.

[46] R. Casati, J. Lemke, M. Vedani, Microstructure and Fracture Behavior of 316L Austenitic Stainless Steel Produced by Selective Laser Melting, Journal of Materials Science & Technology 32(8) (2016) 738-744.

[47] C.L.A. Leung, S. Marussi, M. Towrie, R.C. Atwood, P.J. Withers, P.D. Lee, The effect of powder oxidation on defect formation in laser additive manufacturing, Acta Materialia 166 (2019) 294-305.

[48] M.L. Montero-Sistiaga, M. Godino-Martinez, K. Boschmans, J.-P. Kruth, J. Van Humbeeck, K. Vanmeensel, Microstructure evolution of 316L produced by HP-SLM (high power selective laser melting), Additive Manufacturing 23 (2018) 402-410.

[49] U. Scipioni Bertoli, B.E. MacDonald, J.M. Schoenung, Stability of cellular microstructure in laser powder bed fusion of 316L stainless steel, Materials Science and Engineering: A 739 (2019) 109-117.

[50] T.S.a.S.M. Masamitsu WAKOH, Effect of S Content on the MnS Precipitation in Steel with Oxide
Nuclei, ISIJ International 36(8) (1996) 1014-1021.

[51] J.H. Shin, J.H. Park, Formation Mechanism of Oxide-Sulfide Complex Inclusions in High-Sulfur-Containing Steel Melts, Metallurgical and Materials Transactions B 49(1) (2017) 311-324.

[52] H.-G.L.a.K.-S.O. Ham S. Kim, Precipitation Behavior of MnS on Oxide Inclusions in Si/Mn Deoxidized Steel, Metals and Materials 6(4) (2000) 305-310.

[53] Y.X. Pengjun Fang, Xinggang Li, Ya Chen, Influence of Atomizing Gas and Cooling Rate on Solidification Characterization of Nickel-based Superalloy Powders, Rare Metal Materials and Engineering 47(2) (2018) 423-430.

[54] U. Scipioni Bertoli, G. Guss, S. Wu, M.J. Matthews, J.M. Schoenung, In-situ characterization of laser-powder interaction and cooling rates through high-speed imaging of powder bed fusion additive manufacturing, Materials & Design 135 (2017) 385-396.

[55] I. Muto, D. Ito, N. Hara, Microelectrochemical Investigation on Pit Initiation at Sulfide and Oxide Inclusions in Type 304 Stainless Steel, Journal of The Electrochemical Society 156(2) (2009).

[56] K.H. Jiheon Jun, G.S. Frankel, Pitting Corrosion of Very Clean Type 304 Stainless Steel, Corrosion 70(2) (2013) 146-155.

[57] F.P. Glasser, The system MnO-SiO2, American Jounral of Science 256 (1958) 398-412.

[58] R.P. Reed, Nitrogen in austenitic stainless steels, JOM 41(3) (1989) 16-21.

[59] R.J. Hebert, Viewpoint: metallurgical aspects of powder bed metal additive manufacturing, Journal of Materials Science 51(3) (2015) 1165-1175.

[60] A.N.D. Gasper, B. Szost, X. Wang, D. Johns, S. Sharma, A.T. Clare, I.A. Ashcroft, Spatter and oxide formation in laser powder bed fusion of Inconel 718, Additive Manufacturing 24 (2018) 446-456.

[61] Q. Guo, C. Zhao, L.I. Escano, Z. Young, L. Xiong, K. Fezzaa, W. Everhart, B. Brown, T. Sun, L. Chen, Transient dynamics of powder spattering in laser powder bed fusion additive manufacturing process revealed by in-situ high-speed high-energy x-ray imaging, Acta Materialia 151 (2018) 169-180.

[62] M. Taheri Andani, R. Dehghani, M.R. Karamooz-Ravari, R. Mirzaeifar, J. Ni, Spatter formation in selective laser melting process using multi-laser technology, Materials & Design 131 (2017) 460-469.

[63] S.A. Khairallah, A.T. Anderson, A. Rubenchik, W.E. King, Laser powder-bed fusion additive manufacturing: Physics of complex melt flow and formation mechanisms of pores, spatter, and denudation zones, Acta Materialia 108 (2016) 36-45.

[64] M. Simonelli, C. Tuck, N.T. Aboulkhair, I. Maskery, I. Ashcroft, R.D. Wildman, R. Hague, A Study on the Laser Spatter and the Oxidation Reactions During Selective Laser Melting of 316L Stainless Steel, Al-Si10-Mg, and Ti-6Al-4V, Metallurgical and Materials Transactions A 46(9) (2015) 3842-3851.

[65] M. Taheri Andani, R. Dehghani, M.R. Karamooz-Ravari, R. Mirzaeifar, J. Ni, A study on the effect of energy input on spatter particles creation during selective laser melting process, Additive Manufacturing 20 (2018) 33-43.

[66] Y. Liu, Y. Yang, S. Mai, D. Wang, C. Song, Investigation into spatter behavior during selective laser melting of AISI 316L stainless steel powder, Materials & Design 87 (2015) 797-806.

[67] D. Wang, S. Wu, F. Fu, S. Mai, Y. Yang, Y. Liu, C. Song, Mechanisms and characteristics of spatter generation in SLM processing and its effect on the properties, Materials & Design 117 (2017) 121-130.

[68] P. Bidare, I. Bitharas, R.M. Ward, M.M. Attallah, A.J. Moore, Fluid and particle dynamics in laser powder bed fusion, Acta Materialia 142 (2018) 107-120.

[69] C. Pauzon, E. Hryha, P. Forêt, L. Nyborg, Effect of argon and nitrogen atmospheres on the properties of stainless steel 316 L parts produced by laser-powder bed fusion, Materials & Design 179 (2019).

[70] E.K. Kenji Kako, Joji Ohta and Masami Mayuzumi, Effects of Various Alloying Elements on Tensile Properties of High-Purity Fe–18Cr–(14–16)Ni Alloys at Room Temperature, Materials Transactions 43 (2002) 155-162.

[71] D.-R. Eo, S.-H. Park, J.-W. Cho, Controlling inclusion evolution behavior by adjusting flow rate of shielding gas during direct energy deposition of AISI 316 L, Additive Manufacturing 33 (2020).

[72] K.B.J. Mills K C, Brooks R F, et al., Marangoni effects in welding, Philosophical Transactions of the Royal Society of London. Series A: Mathematical, Physical and Engineering Sciences 356(1739) (1998) 911-925.

[73] C. Li, Y. Shi, Y. Gu, F. Yang, Effect of oxide on surface tension of molten metal, RSC Advances 7(85) (2017) 53941-53950.

[74] S. Ly, A.M. Rubenchik, S.A. Khairallah, G. Guss, M.J. Matthews, Metal vapor micro-jet controls material redistribution in laser powder bed fusion additive manufacturing, Sci Rep 7(1) (2017) 4085.

[75] C. Qiu, C. Panwisawas, M. Ward, H.C. Basoalto, J.W. Brooks, M.M. Attallah, On the role of melt flow into the surface structure and porosity development during selective laser melting, Acta Materialia 96 (2015) 72-79.

[76] V. Gunenthiram, P. Peyre, M. Schneider, M. Dal, F. Coste, I. Koutiri, R. Fabbro, Experimental analysis of spatter generation and melt-pool behavior during the powder bed laser beam melting process, Journal of Materials Processing Technology 251 (2018) 376-386.

[77] A.R. Nassar, M.A. Gundermann, E.W. Reutzel, P. Guerrier, M.H. Krane, M.J. Weldon, Formation processes for large ejecta and interactions with melt pool formation in powder bed fusion additive manufacturing, Sci Rep 9(1) (2019) 5038.

[78] L.I. Escano, N.D. Parab, L. Xiong, Q. Guo, C. Zhao, K. Fezzaa, W. Everhart, T. Sun, L. Chen, Revealing particle-scale powder spreading dynamics in powder-bed-based additive manufacturing process by high-speed x-ray imaging, Sci Rep 8(1) (2018) 15079.

[79] C.L.A. Leung, S. Marussi, M. Towrie, J. del Val Garcia, R.C. Atwood, A.J. Bodey, J.R. Jones, P.J. Withers, P.D. Lee, Laser-matter interactions in additive manufacturing of stainless steel SS316L and 13-93 bioactive glass revealed by in situ X-ray imaging, Additive Manufacturing 24 (2018) 647-657.

[80] J. Yin, D. Wang, L. Yang, H. Wei, P. Dong, L. Ke, G. Wang, H. Zhu, X. Zeng, Correlation between forming quality and spatter dynamics in laser powder bed fusion, Additive Manufacturing 31 (2020).

[81] P. Deng, M. Karadge, R.B. Rebak, V.K. Gupta, B.C. Prorok, X. Lou, The origin and formation of oxygen inclusions in austenitic stainless steels manufactured by laser powder bed fusion, Additive Manufacturing 35 (2020).

[82] U. Ali, R. Esmaeilizadeh, F. Ahmed, D. Sarker, W. Muhammad, A. Keshavarzkermani, Y. Mahmoodkhani, E. Marzbanrad, E. Toyserkani, Identification and characterization of spatter particles and their effect on surface roughness, density and mechanical response of 17-4 PH stainless steel laser powder-bed fusion parts, Materials Science and Engineering: A 756 (2019) 98-107.

[83] M.A.A. Khairallah S A, Lee J R I, et al, Controlling interdependent meso-nanosecond dynamics and defect generation in metal 3D printing, Science 368(6491) (2020) 660-665.

[84] A.B. Anwar, Q.-C. Pham, Selective laser melting of AlSi10Mg: Effects of scan direction, part placement and inert gas flow velocity on tensile strength, Journal of Materials Processing Technology 240 (2017) 388-396.

[85] H. Zheng, H. Li, L. Lang, S. Gong, Y. Ge, Effects of scan speed on vapor plume behavior and spatter generation in laser powder bed fusion additive manufacturing, Journal of Manufacturing Processes 36 (2018) 60-67.

[86] M.C. Yinmin Wang, Fenghua Zhou, En Ma, High tensile ductility in a nanostructured metal, NATURE 419 (2002) 912-915.

[87] D.J.B. Hull Derek, Introduction to dislocations, Butterworth-Heinemann (2001).

[88] Y.S. Lei Lu, Xianhua Chen, Lihua Qian, K. Lu, Ultrahigh Strength and High Electrical Conductivity in Copper, SCIENCE 304 (2004) 422-426.

[89] S.H. Kim, H. Kim, N.J. Kim, Brittle intermetallic compound makes ultrastrong low-density steel with large ductility, Nature 518(7537) (2015) 77-9.

[90] X. Wu, M. Yang, F. Yuan, G. Wu, Y. Wei, X. Huang, Y. Zhu, Heterogeneous lamella structure unites ultrafine-grain strength with coarse-grain ductility, Proc Natl Acad Sci U S A 112(47) (2015) 14501-5.

[91] L. Liu, Q. Ding, Y. Zhong, J. Zou, J. Wu, Y.-L. Chiu, J. Li, Z. Zhang, Q. Yu, Z. Shen, Dislocation network in additive manufactured steel breaks strength–ductility trade-off, Materials Today 21(4) (2018) 354-361.

[92] N.S. Montero Sistiaga M, Hautfenne C, et al. , Effect of heat treatment of 316L stainless steel produced by selective laser melting (SLM), Proceedings of the 27th Annual International Solid Freeform Fabrication Symposium-An Additive Manufacturing Conference (2016) 558-565.

[93] B. A., Review Progress in Ostwald ripening theories and their applications to the γ′-precipitates in nickel-base superalloys Part II Nickel-base superalloys, Journal of Materials Science 37(12) (2002) 2379-2405.

[94] B. A., Review progress in Ostwald ripening theories and their applications to nickel-base superalloys Part I: Ostwald ripening theories, Journal of materials science 37(11) (2002) 2171-2202.

[95] V.Y. Novikov, Grain growth controlled by mobile particles on grain boundaries, Scripta Materialia 55(3) (2006) 243-246.

[96] R.B. Randle V, Interactions of grain boundaries with coherent precipitates during grain growth, Acta Metallurgica 34(5) (1986) 891-898.

[97] S. Vedantam, A. Mallick, Phase-field theory of grain growth in the presence of mobile second-phase particles, Acta Materialia 58(1) (2010) 272-281.

[98] I.O.a.K.I. Ryosuke Kainuma, Dragging of Liquid Bi Particles Induced by Grain Boundary Migration in Al–Bi Alloys, Materials Transactions 44(9) (2003) 1768-1773.

[99] Y.R.R. Antsiferov V N, Growth of dispersed oxide inclusions in 80% Ni-20% Cr alloys during annealing, Soviet Powder Metallurgy and Metal Ceramics 10(6) (1971) 482-484.

[100] O.H. Naka S, Bouchaud E, et al, Reprecipitation observed in Y2O3 dispersed titanium during heat treatment after cold rolling, Scripta metallurgica 23(4) (1989) 501-505.

[101] B.J.P. Bouchaud E, Naka S, et al, Dissolution of precipitates by migrating grain boundaries, Acta metallurgica et materialia 40(12) (1992) 3451-3458.

[102] N. Sallez, C. Hatzoglou, F. Delabrouille, D. Sornin, L. Chaffron, M. Blat-Yrieix, B. Radiguet, P. Pareige, P. Donnadieu, Y. Bréchet, Precipitates and boundaries interaction in ferritic ODS steels, Journal of Nuclear Materials 472 (2016) 118-126.

[103] C.S.A. Lofvander J P A, Kirchheim R, et al, Thermal stability of rare-earth oxides in Ti when annealed above the α/β transus, Scripta metallurgica 21(6) (1987) 859-861.

[104] G.R.M.A. Ashby M F, The dragging of small oxide particles by migrating grain boundaries in copper, Acta Metallurgica 16(9) (1968) 1081-1092.

[105] P.I.G. Ashby M F, The dragging of solid particles through metals by grain boundaries, Acta Metallurgica 15(2) (1967) 420-423.

[106] R.T.M. Serebryakov A V, Lobanov V I, On recrystallization of dispersion-hardened alloys, Physica status solidi (a) 14(1) (1972) 77-81.

[107] S.L.S. Gottstein G, Theory of grain boundary motion in the presence of mobile particles, Acta metallurgica et materialia 41(11) (1993) 3267-3275.

[108] D. Zhou, Z. Quadir, C. Kong, H. Pan, Z. Liu, G. Sha, P. Munroe, D. Zhang, Understanding structural evolution of nanostructured Cu-Al2O3 composite powders during thermomechanical processing, Materialia 4 (2018) 268-275.

[109] V.R. D, On the Ostwald ripening theory, Acta metallurgica 30(6) (1982) 1079-1086.

[110] P.W. Voorhees, The theory of Ostwald ripening, Journal of Statistical Physics 38(1-2) (1985) 231-252.

[111] J.A. Marqusee, J. Ross, Theory of Ostwald ripening: Competitive growth and its dependence on volume fraction, The Journal of Chemical Physics 80(1) (1984) 536-543.

[112] M.H.W. Batz W, Birchenall C E, Diffusion of silicon in iron, JOM 4(10) (1952) 1070-1070.

[113] P.M. H. V. M. MIRANI, Diffusion of Si in Fe-Si Containing 8 to 11 at% Si, Physica status solidi (a) 14(2) (1972) 521-525.

[114] S.L. Shang, H.Z. Fang, J. Wang, C.P. Guo, Y. Wang, P.D. Jablonski, Y. Du, Z.K. Liu, Vacancy mechanism of oxygen diffusivity in bcc Fe: A first-principles study, Corrosion Science 83 (2014) 94-102.

[115] E.A. Marquis, Core/shell structures of oxygen-rich nanofeatures in oxide-dispersion strengthened Fe–Cr alloys, Applied Physics Letters 93(18) (2008).

[116] M.J. Alinger, On the Formation and Stability of Nanometer Scale Precipitates in Ferritic Alloys during Processing and High Temperature Service, University of California, Santa Barbara (2004).

[117] D.A. Porter, Kenneth E. Easterling, and Mohamed Sherif, Phase Transformations in Metals and Alloys, CRC press (2009).

Appendix

Fig 53 Concept Laser Mlab cusing laser powder fusion system.

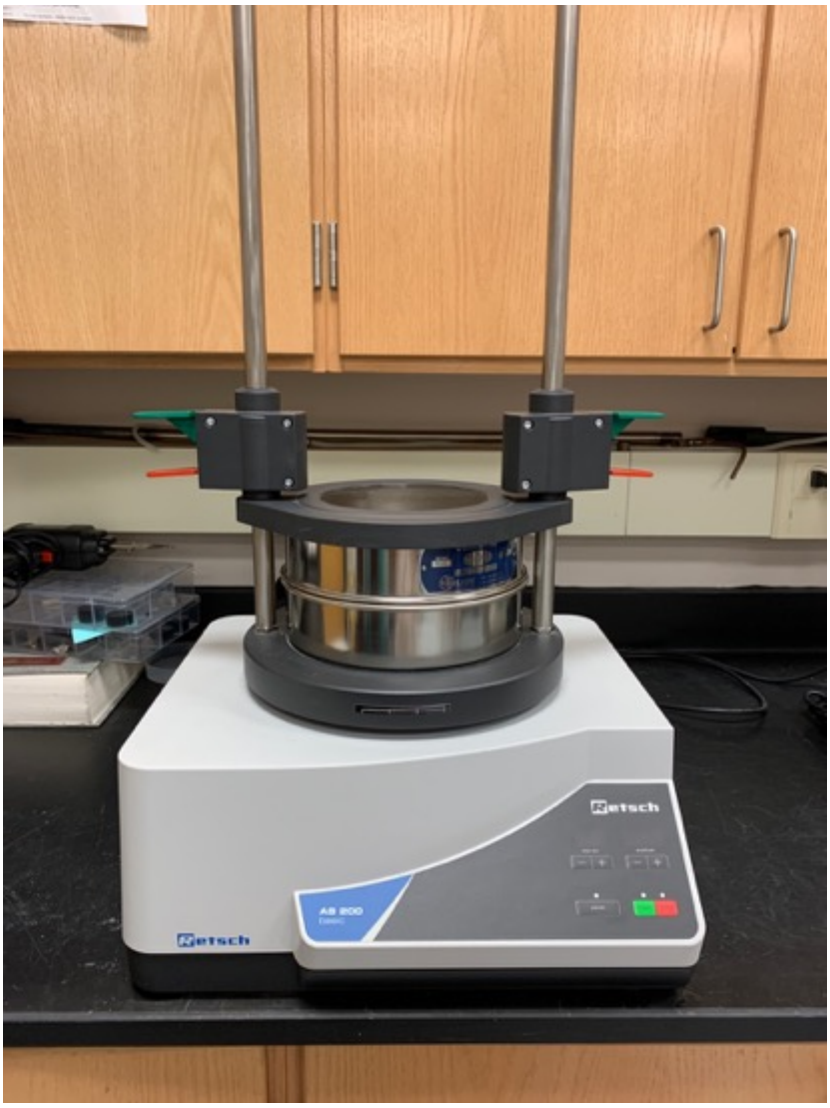

Fig 54 Retsch AS 200 sieve shakers.

Fig 55 Buehler IsoMet 2000 precision cutting machine.

Fig 56 Buehler VibroMet 2 vibratory polisher.

Fig 57 Struers TegraPol-15 Auto-polisher with Tegraforce-1.

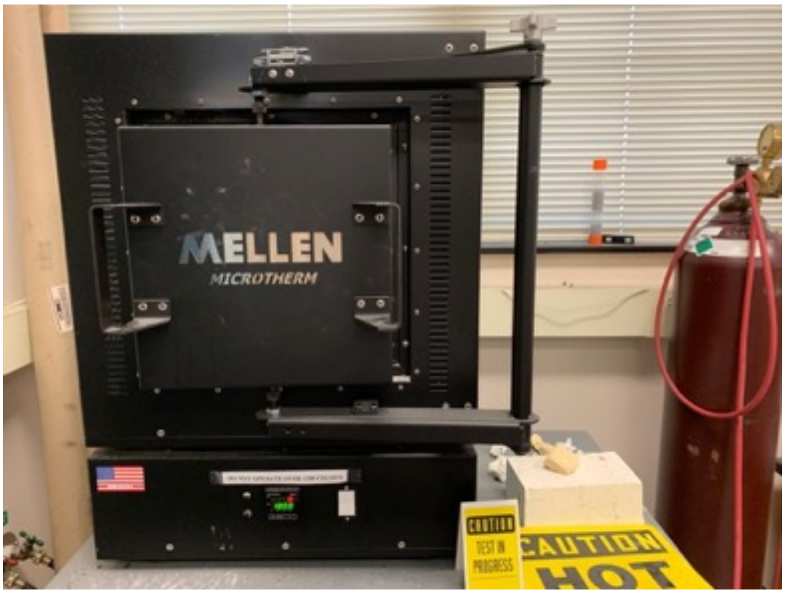

Fig 58 Mellen Microtherm box furnace.

Fig 59 DM-400 FT Microhardness tester (LECO Corporation)

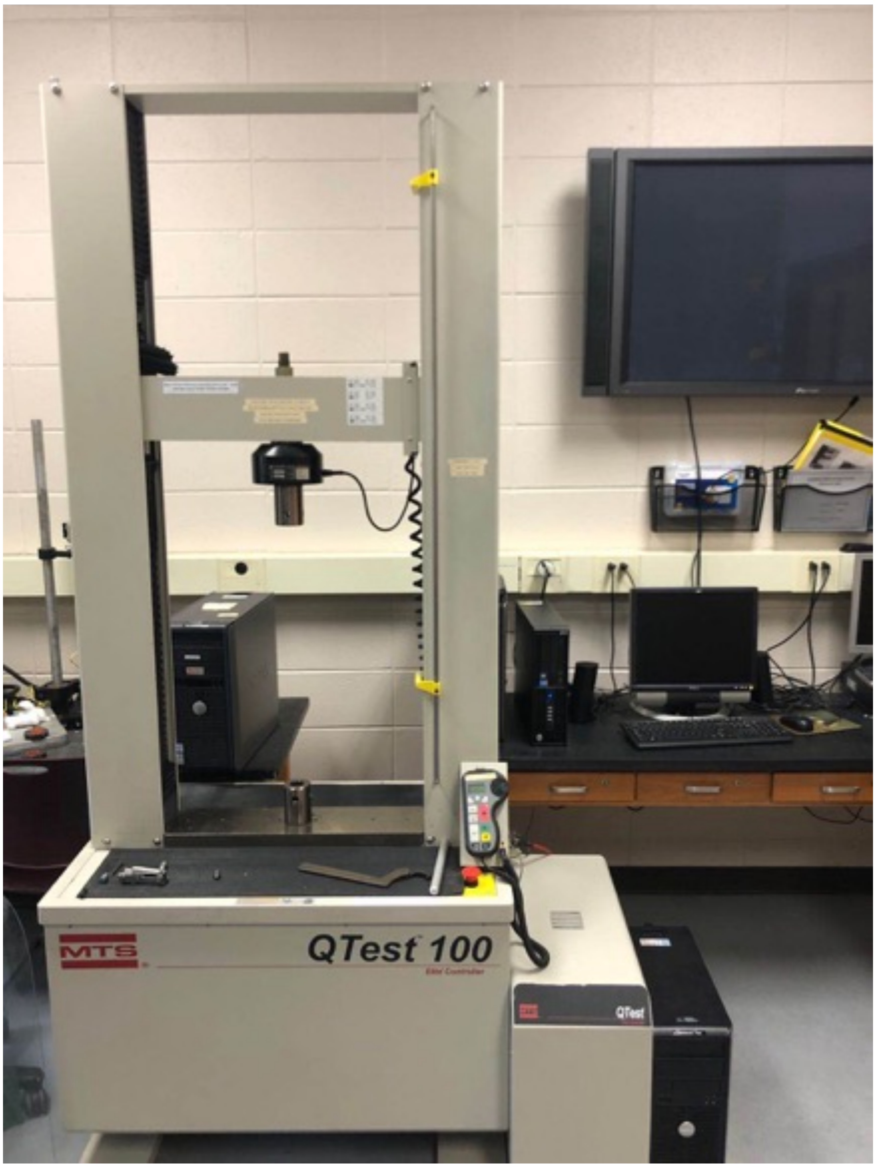

Fig 60 MTS Q-test 100 Elite Testing system

Fig 61 Tinius Olsen impact testing machine

Fig 62 JEOL JSM 7000F scanning electron microscope.

Fig 63 Olympus BX51 microscope

Fig 64 KEYENCE VHX-6000 series microscope